

Data-Driven based Fault Detection and Diagnosis for Vapor Compression Chillers

By SWARNALI MUKHOPADHYAY, M.Sc, B.E

A Thesis Submitted to the School of Graduate Studies in Partial Fulfilment of the Requirements for
the Degree of Doctor of Philosophy

McMaster University © Copyright by Swarnali Mukhopadhyay, October 2024

Data-Driven based Fault Detection and Diagnosis for Vapor Compression Chillers

DOCTOR OF PHILOSOPHY (2016), McMaster University, Hamilton, Ontario
(Mechanical Engineering)

TITLE: Data-Driven based Fault Detection and
Diagnosis for Vapor Compression Chillers

AUTHOR: Swarnali Mukhopadhyay
B.E. (University of Mumbai)
M.Sc. (University of New Haven)

SUPERVISOR: Dr. Saeid Habibi

NUMBER OF PAGES: xvi, 204

Abstract

Refrigeration is a fast-growing industry and has become an integral part of various industries such as food storage, pharmaceutical, residential, chemical, and data centers. Rising global temperatures have increased the need for more energy-efficient and environmentally conscious refrigeration systems. A consistent functioning refrigeration system requires good fault detection and diagnosis (FDD) system to detect faults before failures occur. A good FDD system can help reduce maintenance costs and increase energy savings. The refrigerant present in the chillers consists of greenhouse gases. Certain faults, such as refrigerant leakage, result in the release of refrigerant into the atmosphere, which has an environmental impact. Hence, an effective FDD system for chillers is important for accurately detecting and diagnosing faults. This thesis aims to build a data-driven FDD system for vapor-compression chillers. The purpose of this thesis is to address the variable operating conditions and fault conditions that occur during the operation of a chiller system. The operating conditions vary depending on the control logic, climate, and other factors that can occur in a system with multiple components. Faults can occur to varying degrees within a system. Early fault detection and diagnosis lead to prompt maintenance dispatching. It is imperative that an FDD system accommodates these conditions and accurately detect faults.

This thesis uses two types of data to build an FDD model. The experimental data provided by ASHRAE RP-1043, which contained both normal and fault conditions, were used. The ASHRAE dataset contains normal conditions and seven fault conditions at the four severity

levels. Other types of data used were simulated data generated using the ASHRAE RP-1043 model and a small chiller model developed by the author. Simulated data supplemented the experimental dataset with different normal operating conditions and fault severity levels. A hybrid architecture consisting of a dimensionality reduction method and classifier was proposed. This architecture facilitates the comparison of machine learning and deep learning techniques, and may be employed to develop a hybrid model that incorporates both approaches. Time series data was used to train and test this architecture. A deviation matrix method, which is a preprocessing method applied to the training and testing datasets, was proposed. This method was used with steady-state data to develop a 2D Convolutional Neural Network (CNN), Artificial Neural Network (ANN), and Support Vector Machine (SVM). The deviation matrix method proved effective for machine learning and deep learning models to detect and diagnose faults for different normal and fault severity levels.

A study using steady-state time-series data and complete test cycle data was conducted to build and test the hybrid architecture. It was concluded that using steady-state time-series data yielded a higher classification accuracy for faults. The deviation matrix method was applied to the simulation and experimental data, and 2D CNN, ANN, and SVM were used to study these datasets. It was concluded that some parts of the training data could be substituted with the simulation data to obtain acceptable classification accuracy. The 2D CNN, ANN, and SVM were able to diagnose faults in the test data containing different severity levels from the training set and small-chiller data. The SVM was also effective in detecting near-normal operations.

These findings imply that using steady-state filters can help increase the diagnostic accuracy of the FDD method. Creating databases of fault conditions is expensive and time consuming. Thus, supplementing the training dataset with simulated data can be beneficial for decreasing the effort required for database creation. The deviation matrix method has been shown to be helpful for data-driven methods in recognizing faults in varying operations, such as near-normal operations and different fault severity levels. These conditions are indicative of the real world and were not included in the training dataset. It was also shown that the FDD methods trained using the ASHRAE data were able to diagnose the two faults of the small chiller. This expands the possibility of generalization among the FDD methods. Data-driven methods can be very specific to the training dataset, but this study proves that the methods can recognize fault signatures irrespective of the system.

Acknowledgements

I express my deepest gratitude to my supervisor, Dr. Saeid Habibi, for his patience, generosity, and guidance through my Ph.D program. His unwavering support and mentorship helped me to reach the end of this journey. Furthermore, I would like to thank my supervisory committee, Dr. Marilyn Lightstone and Dr. Chan Ching, for their invaluable knowledge and feedback. This endeavor would not have started without Dr. Ishwar Puri and Dr. Souvik Pal, whom I would like to thank for giving me the opportunity to pursue my PhD.

I would also like to express my gratitude to my friends and colleagues at McMaster University, who helped me go through my PhD studies. I am also thankful to Dr. Elliot Huangfu, whom I enjoyed working with.

I would be remiss not to mention my parents, who have always supported me unwaveringly and encouraged me throughout my life. Their belief in me made me pursue goals that I thought I could not.

I thank Trevor my partner for always being there for me on my worst and best days. This would have been impossible without the help of you. Finally, I would like to acknowledge Luchi the cat's company through the long nights and very helpful inputs.

Contents

Abstract	ii
Acknowledgements	vii
Contents	viii
List of Figures	xii
List of Tables	xiv
Nomenclature	xv
1. Introduction	1
2. Literature Review	7
2.1 Fundamentals of Chiller Systems	8
2.2 Common Types of Faults in Chiller Systems	11
2.3 Traditional Fault Detection and Diagnosis Methods	13
2.4 Data-Driven Techniques for Fault Detection	16
2.4.1 Data preprocessing	17
2.4.2 Machine Learning for Fault Detection and Diagnosis	20
2.4.3 Deep Learning Techniques for Fault Detection and Diagnosis	28
2.5 Challenges in Data-Driven Techniques	33
2.6 Recent Advances and Future Trends	36
2.6.1 Overview of Recent Advancements	36
2.6.2 Predictions and Future Trends	37
2.7 Research Gaps and Conclusion	38
3. ASHRAE dataset	40
3.1 System description	41
3.2 ASHRAE RP-1043 data set	43
3.2.1 Experiment	43
3.2.2 ASHRAE chiller model	50
3.2.3 Simulation dataset	54
3.3 Summary	56
4. Establishment of FDD methods	57

4.1 Hybrid network	57
4.1.1 Dimensionality Reduction	58
4.1.2 Classifiers	66
4.2 CNN	76
4.2.1 CNN structure for dataset	79
4.2.2 2D input creation method	80
4.2.3 Challenges in image data set generation	89
4.2.4 Deviation Strategy	91
4.3 Pipeline	99
4.4 Summary	100
5. Small chiller model	102
5.1 Modular Cooling System Overview	104
5.1.1 Cooling System set-up	104
5.1.2 Modeling Approach	107
5.2. System Faults	109
5.3. Mathematical Modeling	109
5.3.1 IT Rack Cooling Unit	110
5.3.2 Compressor	111
5.3.3 Condenser	112
5.3.4 Expansion Valve	112
5.3.5 Evaporator	113
5.3.6 Overall Heat Transfer Coefficient	114
5.3.7 Wall-Heat Transfer Model	114
5.3.8 System Model	115
5.4. Fault Models	119
5.5. Analysis	121
5.5.1 Experimentation and model validation	121
5.5.2 Sensitivity Analysis	125
5.5.3 Fault Evaluation	125
5.6 Simulation for FDD model	129
5.7 Summary	132

6. Implementations and Results	134
6.1 Application of Hybrid network for FDD.....	134
6.1.1 Complete dataset.....	136
6.1.2 Steady state dataset	139
6.1.3 Missing severity levels.....	140
6.2 Application of 2D input method	141
6.2.1 Dataset with only ASHRAE simulation data	142
6.2.2 Dataset with combined simulation and experimental data.....	144
6.2.3 Training data as simulated and testing data as experimental	145
6.2.4 Influence of experimental data on testing.....	146
6.2.5 Influence of experimental data on training	147
6.2.6 Testing using missing severity level	148
6.2.7 Testing using near normal and other normal data	149
6.2.8 Testing using small chiller data.....	150
6.3 Summary	151
7. Discussion	153
7.1 Effect of Steady State Data	153
7.2 Simulation and Experimental data	156
7.3 Missing Severity Level Data.....	157
7.4 Testing New Data.....	158
7.5 Implications.....	160
7.6 Limitations	162
7.7 Summary	163
8. Conclusion	164
8.1 Concluding remarks	164
8.2 Recommendations for future work	166
Appendix - 1	168
A1. Pressure drop in refrigerant loop heat exchanger.....	168
Appendix - 2. Overall Heat Transfer Coefficient.....	171
A2.1 Evaporator	171
A2.2 Condenser.....	174

Appendix - 3 Model Sensitivity Analysis177

Bibliography180

List of Figures

1.1	States of fault detection and diagnosis	3
2.1	Vapor compression chiller system	10
2.2	Classification fault detection and diagnostic methods	14
2.3	Classification of HVAC FDD methods	17
	Schematic of Simplified Water Flow Diagram of Chiller Test	41
3.1	Stand	49
3.2	One Test cycle of ASHRAE experiment	52
3.3	Model description flow chart	57
4.1	Hybrid network architecture	62
4.2	Variance ratio of 65 features using PCA Variance ratio of 65 features using PCA	63
4.3 (a)	Data points before PCA	63
4.3 (b)	Data points after applying PCA	64
4.4	Autoencoder structure	65
4.5	LSTM AE architecture	68
4.6	SVM data plot	72
4.7	A single neuron architecture	75
4.8	ANN architecture	77
4.9	Convolutional Neural Network architecture	80
4.10	CNN architecture for fault classification	82
4.11	Sine wave with three quantile bins	83
4.12 (a)	MTF image	83
4.12 (b)	Aggregated MTF image	84
4.13	MTF of 4 features from normal operation	86
4.14	Polar coordinate graph for sine time series	87
4.15	GASF image for sine wave	88
4.16	Four features from ASHRAE dataset	88
4.17	GASF of 4 features from normal operation	90
4.18	Comparison of simulated and experimental images	93
4.19	RFE for RandomForestClassifier	94
4.2	Workflow for feature selection from the ASHRAE dataset	97
4.21	Features in deviation matrix	98
4.22	Images generated using deviation strategy for faults	99
4.23	Workflow to implement deviation matrix method	104
5.1	Schematic of experimental set-up	107
5.2	Schematic of the vapor compression chiller system	108
5.3	Pressure-Enthalpy diagram of refrigeration cycle	115
5.4	Thermal resistance network for tube with insulation	

5.5	Flowchart of chiller model	118
5.6	Temperature profile under 3kW loadings	122
5.7	Temperature profile under 2.3kW loadings	123
5.8	Fault simulation at varying fault levels	127
6.1	LSTM Architecture	135
6.2	Confusion matrix of test data of the complete dataset	137
6.3	Confusion matrix of test data of the steady state dataset	139
6.4	Confusion matrix for simulated dataset	143
6.5	Confusion matrix for combined simulated and experimental data	144
6.6	Confusion matrix for experimental data	145
6.7	Accuracy w.r.t varying experimental data in testing dataset	146
6.8	Accuracy w.r.t varying experimental data in training dataset	147
6.9	Confusion matrix for different severity level dataset	149
6.10	Confusion matrix of near normal test data	150
6.11	Confusion matrix of small chiller test data	151
7.1	Test accuracy for two datasets	154

List of Tables

3.1	List of features from experimental test runs	44
3.2	Steady- state conditions matrix	47
3.3	Types of faults tested for ASHRAE RP 1043	50
3.4	Operating conditions for simulated data	55
3.5	Faults simulated in chiller model	55
4.1	List of activation functions	73
4.2	Total number of samples available for data set	89
4.3	List of features obtained from feature selection method	94
5.1	Components of the experimental set-up	105
5.2	Instrumentation details	106
5.3	Model parameters	116
5.4	Constants of the chiller system	121
5.5	Simulated faults	126
5.6	Simulated operation conditions	130
5.7	Small chiller fault models	132
6.1	List of classes	136
6.2	Classification accuracy of all models for complete data	138
6.3	Classification accuracy of all models for steady state data	140
6.4	Classification accuracy of all models with missing severity level data	141
6.5	Faults simulated in chiller model	142

Nomenclature

A	Area (m^2)		
Bo	Boiling number		
C_p	Specific heat capacity ($\text{J kg}^{-1}\text{C}^{-1}$)		
d	Diameter (m)		
Fr	Froude number		
F	Friction factor		
G	Mass flux (m^3s^{-1})		
Gr	Grasshof number		
g	Mass flow rate (kg s^{-1})		
h	Enthalpy (J kg^{-1})		
K	Thermal conductivity ($\text{W m}^{-1}\text{K}^{-1}$)		
LMTD	Logarithmic mean temperature difference		
L	Length (m)		
M	Mass (kg)		
N	Compressor rotary speed (rpm)		
N	Polytrophic efficiency		
P	Pressure (Pa)		
Pr	Prandtl number		
pr	Critical pressure (Pa)		
Q	Heat transfer (W)		
Ra	Rayleigh number		
Re	Reynolds number		
S_f	Spacing between fins (m)		
T	Temperature ($^{\circ}\text{C}$)		
t	Time (sec)		
U	Overall heat transfer coefficient ($\text{W m}^{-2}\text{K}^{-1}$)		
W	Work (J kg^{-1})		
vol	Displacement volume in compressor		
x	Vapor quality		
A	Heat transfer coefficient ($\text{W m}^{-2}\text{K}^{-1}$)		
H	Volumetric efficiency		
P	Density (kg m^{-3})		
M	Viscosity (Pa s^{-1})		
		Subscripts	
		a	Air
		ao	Air out
		ai	Air in
		b	Base
		ca	Cold air
		cw	Cold water
		cu	Cooling unit
		cp	Compressor
		cn	Condenser
		cv	Control volume
		dis	Discharge
		e	Evaporator
		g	Gas phase
		i	Inner
		ins	Insulation
		l	Liquid phase
		lo	Liquid only
		nb	Nucleate boiling
		o	Outer
		r	Refrigerant
		suc	Suction
		tp	Two-phase
		v	Expansion valve
		w	Water

Declaration of Academic Achievement

This research presents analytical and computational work carried out solely by Swarnali Mukhopadhyay, herein referred to as “the author”, with advice and guidance provided by the academic supervisor Dr. Saied Habibi. Information that is presented from outside sources which has been used towards analysis or discussion, has been cited when appropriate, all other materials are the sole work of the author.

1. Introduction

Refrigeration has been playing an important role in mankind's life for the past 100 years. The need for climate-controlled environments has led to the evolution of refrigeration technology from rudimentary ice houses to more advanced forms of cooling using refrigeration cycles. Refrigeration systems have also been adapted for human comfort in the form of air-conditioning units, cooling, and heating for cars and buildings. Refrigeration technology has not only played a role in small-scale climate control but also in cold storage and other industrial applications. The massive capacity for cold storage has played a vital role in sustaining the food industry during the Green Revolution. Supermarkets have used refrigeration extensively to store and display food items for a long time. Industries, such as petrochemical plants, petroleum refineries, and the paper pulp industry, require large cooling capacities (Ireneo C. Plando, Jr., 2023). Some of the applications for the chemical and process industries are the separation of gases, condensation of gases, dehumidification of air, storage of liquid at low pressure, removal of heat of reaction, and cooling for preservation. The pharmaceutical industry uses filtered air conditioning systems to provide a sterile environment for manufacturing capsules. The production of blood plasma and antibiotics requires freeze-drying, which involves the sublimation of water at low pressure and temperature. Refrigerated centrifuges have also been used to manufacture various drugs. Another application with a growing demand for cooling systems is in data centers. The role of data centers in everyday life has steadily

increased. The increase in the demand for faster, better, and more efficient computing has resulted in higher energy density IT racks in data centers (Y. Zhang et al., 2022).

The energy consumption of the air conditioning and refrigeration sectors accounts for 17% of the global electricity consumption (Coulomb, 2015). There has been a noticeable increase in global usage of refrigeration systems. The frozen food industry is expected to reach \$ 294 billion by 2025. The Intergovernmental Panel on Climate Change (IPCC) estimated a 15-fold increase in the demand for energy for air conditioning between 2025 and 2050, and a 30-fold increase thereafter (Coulomb, 2015). Undetected refrigerant leakage has become a concern because of its contribution to ozone layer depletion and global warming. Such faults, which have not been detected in an increasing number of refrigeration systems, are a major concern.

Katipamula et al. (2005) estimated that improper maintenance of these systems causes a 15-30% loss of energy in building systems. Bruton et al. investigated air handler units (AHU) with different fault detection and diagnosis (FDD) systems and estimated that the FDD system's market achievable energy savings were 0.07-0.8 quads (1 quad=1.055*10¹²MJ) (2013). Li et al. (2007) studied 20 commercial buildings with rooftop units in California and estimated the energy savings based on a model to be USD 42/kW per year in service cost savings and USD 0.071/kWh in utility cost savings. A separate study carried out by Venkatasubramanian et al. (2003) indicated that the petrochemical industry estimated a 20-billion-dollar loss every year due to poor fault detection and diagnosis systems. Hence, it is important to consider abnormal event management (AEM).

Therefore, it is imperative to perform effective fault detection and diagnosis to reduce or eliminate unnecessary energy usage. A suitable FDD system should also continuously monitor the performance of the system, which would help in monitoring the timely maintenance of system components and saving tedious manual checks. Online fault detection and monitoring of the system will make the operation cost effective.

Fault detection and diagnosis are two components of the FDD method. Fault detection checks for the presence of faults in the system, whereas fault diagnosis identifies the fault type, probable reason for the fault, and its location. According to Chiang et al. (2001), process monitoring involves four distinct phases: fault detection, fault isolation, fault diagnosis, and fault recovery, as shown in Figure 1.1. Although these stages are presented sequentially, it is not always necessary to go through each stage. The transition between stages is often automated and seamless, with only essential information presented to the operator for appropriate action.

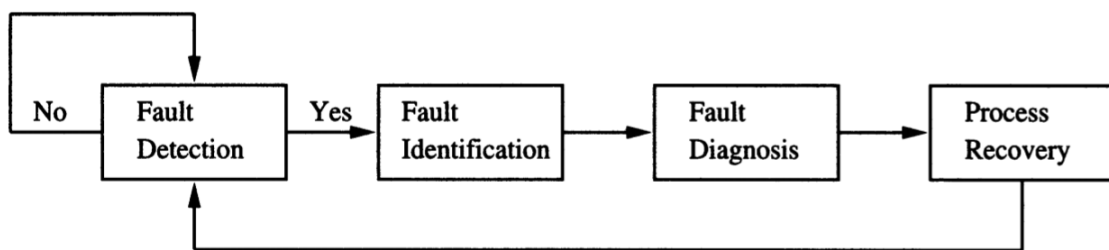


Figure 1.1: Stages of fault detection and diagnosis (L. H. Chiang, 2001)

Fault detection and diagnosis methods for chillers fall under a broad umbrella of heating ventilation and air-conditioning (HVAC) systems. This thesis concentrates on the FDD of the chillers. The FDD method can be categorized into three main approaches: quantitative

model-based, qualitative model-based, and process history-based techniques (Katipamula & Brambley, 2005).

Data-driven methods can be categorized into traditional machine and deep learning-based methods. Machine learning methods use statistical and mathematical techniques to learn patterns in systems using historical data. They can build models with less data, faster training speed, and good interpretability. However, they struggle to perform complex tasks when using high-dimensional data. Deep learning methods are complex neural networks. They require large amounts of data to build relationships in a neuron in order to perform a task. Deep learning methods can handle high-dimensional big data and complex tasks. They have proven to be powerful in time-series modeling, image processing, and knowledge transfer, which are effective strategies for FDD development.

Data-driven methods are data-hungry and require large amounts of data to develop FDD methods. The data quality is crucial for the development of an accurate FDD method. Generating these vast databases of normal and faulty conditions can be expensive and time-consuming. ASHRAE RP-1043 is the only publicly available dataset used by most researchers to develop the FDD methods. The dataset also has low variability in operating conditions and fault severity levels. Thus, the dataset does not completely represent the real-world operation of chillers. Data-driven methods should have access to versatile data consisting of various normal operations and faulty conditions across different types of chillers, so that a generalized FDD can be developed. A generalized FDD is important for detecting and diagnosing faults in a large variety of chillers, thereby saving money and energy through timely maintenance, and reducing consumer discomfort.

The research question that arises from this problem is how data-driven FDD models for chillers can adapt to variable operating conditions and fault severity levels. Which data-driven model is effective for adapting to variable operating conditions and fault severity levels?

Physics-based models of the two types of vapor compression chillers were used to generate various normal operating conditions and fault severity levels. These simulated data were used as a supplement to the experimental data to develop FDD models. This study provides insights into the extent to which simulated data can be used to develop data-driven models. A data preprocessing method using a deviation matrix was developed to generate fault patterns, which would aid the models in fault diagnosis. The deviation matrix method transforms the 1D sensor data into 2D data with prominent fault patterns. This method enables the implementation of 2D artificial intelligence (AI) models. The models were tested against new fault severity levels and near-normal operations to detect normal operations and diagnose faults, respectively. The ability of models to adapt to variations means that they can be tested in the real world. Hence, more studies should be conducted to explore the operational variations to create robust FDD systems. A pre-trained FDD with one type of chiller was used to classify the faults of the different types of chillers. This study assessed the ability of the proposed deviation matrix method and transfer learning technique to diagnose faults. This also contributes to the ability of the models to detect and diagnose faults across different types of chillers.

This thesis comprises eight chapters. This chapter is followed by a review of the relevant literature. The literature review includes a background on FDD and an overall review of

FDD methods used in chillers. Recent advances and future trends are discussed, identifying gaps in literature and the contributions of this study. The third chapter provides an overview of the ASHRAE RP-1043 project, including the experimental setup and database. It also details the simulation plans and simulated database creation. The fourth chapter presents the methodology section. It begins with the development of a hybrid network with feature selection and classifiers based on machine-learning and deep-learning-based methods. Further sections describe the Convolution Neural Network (CNN), investigate 2D input creation methods, and propose the deviation matrix method. Chapter 5 describes the development of the small chiller model and the data-generation exercise. Chapter 6 presents the results of the hybrid network and simulation data using deep learning models. Chapter 7 discusses the results of the previous section. Chapter 8 concludes the thesis, with recommendations for future research.

2. Literature Review

Chillers are a critical component of HVAC system, as they play a crucial role in maintaining optimal temperatures in spaces such as commercial buildings, industrial processes, and data centers. They function by circulating cold air throughout the building via ventilation systems. It is estimated that 15-30% of energy is wasted owing to system faults and improper controls (Katipamula & Brambley, 2005) . The early detection of such failures is essential to prevent service disruptions and minimize energy losses due to improper maintenance. Therefore, the development of fault detection, diagnosis, and prognosis methods is necessary to enable early identification of issues and reduce wear and tear on equipment, ultimately leading to more efficient energy use.

If not promptly addressed, faults may lead to failures that can result in downtime, which disrupts business operations and incurs financial losses. Regular maintenance and repair can minimize the downtime and costs. Malfunctions in the chiller components can result in decreased efficiency and increased operational costs. The early detection of faults can prevent permanent damage to the chiller and extend its lifespan. It would be beneficial to have the ability to assess the health of the chiller to schedule maintenance and reduce the need for premature replacement, thereby saving capital expenses. Chillers in commercial and residential buildings play crucial roles in providing comfortable indoor environments. If chillers operate incorrectly, they can lead to fluctuating temperatures, poor air quality, and other potential health hazards. Certain industries, such as food and data centers, must comply with regulations and standards regarding temperature maintenance, energy efficiency, and environmental impact. Failure to comply with these requirements can result

in spoilage of perishable goods, server failure in data centers, and potential fines, leading to financial and reputational damage. Therefore, fault detection in the chillers is a critical component of HVAC maintenance.

FDD for chillers can largely be divided into traditional and data-driven methods. Traditional methods require expert knowledge of the system and use the rules and alarms determined by an expert to detect faults. The increasing computing power and efficient neural network methods have led to the popularity of data-driven methods. Deep learning (DL) utilizes various levels and arrangements of information representation layers to achieve hierarchical data modeling and processing capabilities. This approach ultimately enhances the system's ability to classify and predict the outcomes.

The literature review details the various FDD methods developed for chillers. It begins with an explanation of the different types of chiller systems and their components. It further details the common types of faults that occur in chiller systems, and the traditional and data-driven methods used to diagnose these faults. The challenges of data-driven methods and future trends in fault diagnosis systems were discussed. This research gap was identified based on the literature review.

2.1 Fundamentals of Chiller Systems

Chiller systems are cooling devices that, along with HVAC systems, maintain the desired indoor environment. These systems have applications in various industries, such as the food industry, data centers, and commercial buildings. Chillers extract heat from a fluid, usually

a mixture of water and glycol or water, which lowers the temperature of water or air present in the desired space.

Various types of chillers are commonly used to provide cooling solutions in different industries. Each type of system has advantages and disadvantages that make it unique and best suited for specific industries.

1. Vapor Compression Chillers: They are a popular type of chiller; they use the compression and expansion of refrigerant gas to remove heat from the system. Vapor compression chillers are found in different configurations, such as air-cooled, water-cooled, seawater-cooled, and oil-free chillers.
2. Absorption Chillers: They use steam or hot water as heat energy to drive the cooling process. They are used where waste heat is available, owing to their energy efficiency.
3. Adsorption Chillers: They use adsorbent materials for heat removal from the system. They are used in scenarios where low-grade heat sources are available to produce chilled water and desalinated water (Szteklér et al., 2019).
4. Hybrid Chillers: These types of chillers combine different cooling systems, such as absorption and compression. These systems are flexible in adapting to varying conditions and provide better performance and energy efficiency.
5. Water-cooled chillers: Water-cooled chillers use cooling towers or water as a medium to remove heat from the refrigerant. They are used in the cooling of large spaces where a high cooling capacity is required.

6. Air-cooled Chillers: These chillers use air to dissipate heat from the refrigerant. These chillers are typically used in small-scale applications, and those for which water is limited.
7. Centrifugal Chillers: Centrifugal chillers use centrifugal force to compress the refrigerant. They have a high cooling capacity and good efficiency. These systems are typically installed in large buildings and in industrial applications.

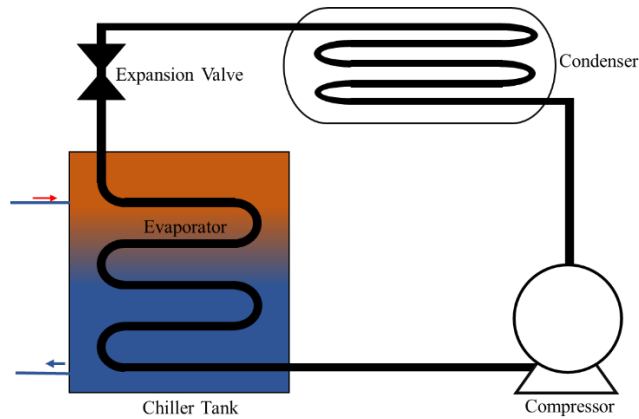


Figure 2.1: Vapor compression chiller system

Figure 2.1 shows the common configuration of a vapor compression chiller system as described above. A chiller system consists of four mechanical components: compressor, condenser, evaporator, and expansion valve. These systems are typically equipped with a control system.

- Compressor: The compressor is an important component of the chiller that circulates the refrigerant within the system. It compresses the refrigerant, thereby increasing its pressure and temperature.

- Condenser: This is a heat exchanger that helps dissipate heat from the refrigerant into the ambient air or water. The refrigerant exited the condenser in a liquid state.
- Expansion valve: The expansion valve is a mechanical valve that decreases the pressure of the refrigerant and regulates its flow at the entrance of the evaporator.
- Evaporator: This is a heat exchanger that absorbs heat from the water or air. This absorbed heat causes the refrigerant to evaporate.
- Control System: Control systems monitor and regulate parameters such as temperature, pressure, and flow rates. These controllers help the system to operate under varying conditions and allow the user to control the output parameters of the chiller.

2.2 Common Types of Faults in Chiller Systems

Faults can be categorized into two types: (a) hard failures that occur suddenly and result in complete shutdown or unsatisfactory comfort conditions and (b) soft faults that result in slow deterioration in performance without a breakdown of the system (Comstock et al., 2001). Hard failures can easily be detected using inexpensive methods. Soft faults, such as the loss of refrigerant or fouling in heat exchangers, present significant challenges in terms of detection and diagnosis.

The most comprehensive study of system failures was conducted by Stouppe for (1989) hermetic air conditioning equipment (1989). The study categorized 76% of the faults were

attributed to electrical components, 19% to mechanical components and 5% to refrigerant circuits.

A study conducted by Braun et al. analyzed a database for direct expansion rooftop air conditioning units (RTU) for common faults and their impact on the performance of the unit (Breuker & Braun, 1998). By examining the service records, they determined how often faults occurred, and calculated the estimated cost of servicing these issues. The most frequent faults were electrical and control-related, and the most expensive service cost was compressor failure. The faults occurring in the refrigeration cycle, such as refrigerant leakage and condenser fouling, are significant but lower than compressor failure. These refrigeration cycle faults lead to compressor failure and a gradual degradation in the efficiency of the RTUs.

Some of the chiller faults mentioned in the literature are as follows:

1. Component faults: Every component of the chiller system is susceptible to faults. Faults in components such as condensers, compressors, evaporators, and valves lead to a decrease in the efficiency and cooling capacity (Cui & Wang, 2005). Other component faults include compressor valve leakage, fan failures in the heat exchanger, frosting in the evaporator, and condenser fouling (Braun, 2003)
2. Sensor faults: These faults can occur owing to the malfunction of sensors, improper installation, and degradation of sensors due to natural wear and tear. This leads to inaccurate measurements that affect controller functions and inefficiency in the

system. Detecting and diagnosing sensor faults are vital for the successful operation of chillers.

3. Refrigerant faults: These types of faults include refrigerant flow, overcharging, leakage, excessive oil, and non-condensable in refrigerants that affect the chiller power consumption and system performance (Cheung & Braun, 2016).
4. Soft faults: Soft faults are slow-growing faults till a noticeable impact on performance occurs in the system. Faults such as sensor drift and fouling in heat exchangers can be classified as soft faults (Jin et al., 2019).

2.3 Traditional Fault Detection and Diagnosis Methods

There are various approaches to FDD of HVAC systems. The literature published over the past 20 years has provided several classifications of FDD methods. However, the classification system proposed by Katipamula and Brambley (2005), which categorizes FDD methods into two primary categories: model-based and process history-based methods, has gained widespread acceptance in many publications. This classification is illustrated in Figure 2.2.

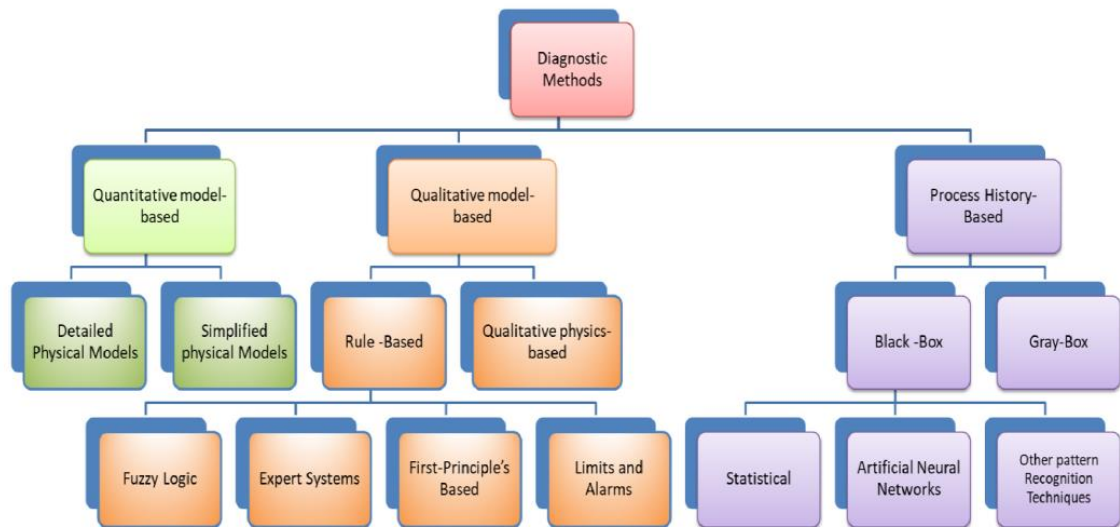


Figure 2.2: Classification fault detection and diagnostic methods (Katipamula & Brambley, 2005)

➤ Quantitative model- based

Model-based methods use a physics-based mathematical representation of a system to detect and diagnose faults. It compares sensor measurements to computed values to detect the occurrence of faults. The quantitative model-based approach is categorized into detailed and simplified models. Physical models were developed using the fundamental physical governing principles of the system. The FDD is developed using a system model that inputs measurements and model parameters, and the modeled output is compared with the measured output. Detailed physical models use complex mathematical equations to represent the interactions between various components in a system. Equations such as mass, momentum, energy

balances, and heat and mass transfer relations were applied and solved. These models can simulate transience as well as normal and fault conditions.

➤ Qualitative model- based

This type of FDD method is based on qualitative modeling techniques, which, unlike quantitative methods, use mathematical equations to represent the system. Qualitative methods use qualitative or knowledge-based relations to relate the state of a system to its components. Qualitative model-based methods can be categorized into rule-based and qualitative physics-based models. Rule-based systems use rules developed based on expert knowledge and first-principles. It is a form of if- then- statements gathered in an expert database by knowledge engineers. Systems with limited process knowledge can be represented using qualitative physics-based models that depict their state. Some of the parameters were fine-tuned to represent the system accurately. Therefore, knowledge of the system is required to develop these models.

An FDD for refrigerator faults was developed using dynamic non-linear state estimation techniques that generate residuals between the measured and estimated states to perform diagnostic classification (Wagner & Shoureshi, 1992). A steady-state model was used to develop an FDD for a packaged chiller that used nine temperatures and a humidity sensor to investigate five faults (Rossi & Braun, 1997). An FDD for large chillers was developed using five features to identify six faults (Reddy, 2007). A refrigerant leakage detection

method was developed for a vapor compression chiller using a qualitative model-based method that employs an adaptive model and dynamic thresholds (Navarro-Esbrí et al., 2006). A model-based FDD for a centrifugal chiller was developed using six physical performance indices that indicated the health of the system (Cui & Wang, 2005). Over time, qualitative models have advanced and started hybridizing with process history-based techniques to increase non-linearity in the model and take advantage of black-box models (A. Beghi et al., 2016; Bonvini et al., 2014; N. Tudoroiu et al., 2008; B. Sun et al., 2011; K. Yan et al., 2017). A significant amount of work has been conducted on model-based methods between 1980 and 2005 (Katipamula & Brambley, 2005). Process history-based methods started in 1990 and have become increasingly popular in the last decade (Yang Zhao et al., 2019).

2.4 Data-Driven Techniques for Fault Detection

In the past decade, there has been a notable increase in data-driven methods for FDD in HVAC systems. Bi et al. (2024) categorized HVAC FDD methods, as shown in Figure 2.3.

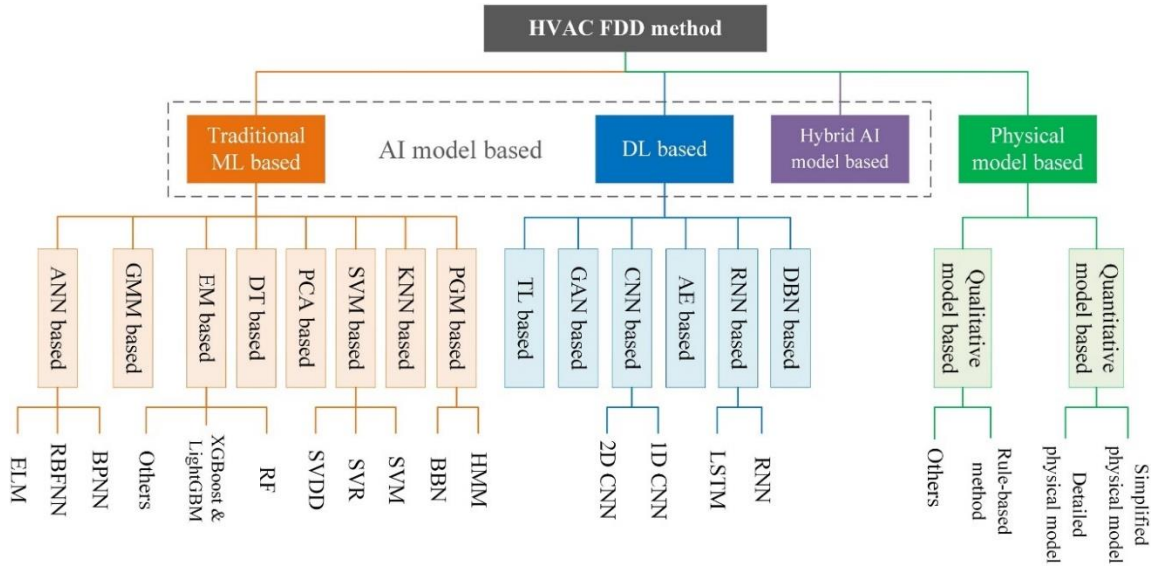


Figure 2.3: Classification of HVAC FDD methods (Bi et al., 2024)

Data-driven techniques can be categorized into machine- and deep learning-based methods. Statistical, linear algebra, optimization, and other mathematical techniques are employed by machine learning algorithms to create predictive models based on existing data. Deep learning methods are advanced and have adaptable network architectures. They are based on neural networks that are trained for fault-detection and diagnosis tasks. Researchers are increasingly adopting deep learning methods owing to rapid progress in AI research. The machine learning and deep learning methods are discussed in detail in the following sections.

2.4.1 Data preprocessing

Data preprocessing was conducted prior to the FDD. Preprocessing typically involves cleaning, transformation, integration, and data reduction. Data cleaning helps address missing values and noise from sensor data to reduce false alarms. Data transformation

involves normalizing, scaling, and weighting the variables to obtain more consolidated data. Data reduction was used to reduce the dimensionality of the data. Linear Discriminant Analysis (LDA) and Principal Component Analysis (PCA) are the most common dimensionality reduction methods (Soltani et al., 2022).

2.4.1.1 Feature Selection

Data-driven classification models depend on the quality of the training datasets. Therefore, the selection of relevant features and their correlations is important. An optimal subset of features increases fault identification and decreases model overfitting, false alarms, and complexity (K. Yan et al., 2018).

Chandrashekar et al. (2014) divided the feature selection method into three main groups: filter, wrapped and embedded methods. The filter method ranks features based on the confidence level of the training set. The wrapping method uses a feature selector wrapped in a classifier. This is dependent on the functionality of the classifier, which makes it more computationally expensive and unsuitable for large datasets. Feature selection is integrated into the training process in embedded methods, which results in faster performance compared to the wrapper method.

Some studies have conducted sensitivity analyses to select the relevant features (Mathew C. Comstock, 1999; Zhou et al., 2009). Yan et al. (2014) developed a filter-based method (Relieff) to select a subset of features for chiller FDD. A method combining filter-based and wrapper selection algorithms was applied to select features that achieved the highest classification accuracy (Hua Han et al., 2011; Mochammad et al., 2021). Tian et al. (2021)

improved the maximum relevance and minimum redundancy algorithms (K. Sun et al., 2016) which use feature relevance with the type fault. A CNN comprises feature extraction and classification layers. Various studies have developed methods for feature extraction and temporal CNN for the FDD of chillers. A sparsity regularization filter was used to reduce redundancy and improve fault diagnosis (H. Gao et al., 2022). ReliefF was used to screen features, Recursive Feature Elimination on Cross-Validation (RFECV) was used for optimal subset selection, and SVM was used for fault classification, achieving high accuracy and efficiency (Nie et al., 2023). Embedded methods such as feature-enhanced techniques and encoder-decoder networks for residual feature extraction were compared (B. Li et al., 2021) and Linear Support Vector Classification (LinearSVC)-based feature selection method was used followed by CNN (X. Sun et al., 2020). He et al. used a Sequential floating Forward Search (SFS) for the feature selection of sensor deviation data (Y. He et al., 2023). A cost-sensitive SFS was proposed to select the optimum number of features and required sensor placement (K. Yan et al., 2018). Some interpretable methods have been developed to facilitate the visualization of feature contributions in embedded feature extraction methods. Techniques such as Gradient-weighted Class Activation are used in CNN (G. Li et al., 2021) and the Shapley Additive explanation is used in autoencoder (Gupta et al., 2022) to interpret fault detection in deep learning methods. The loss of data that occurs due to feature extraction is desired to be understood from the earlier mentioned works.

2.4.2 Machine Learning for Fault Detection and Diagnosis

Machine-learning-based FDD methods can increase productivity and decrease the cost of the process in industry and academia (K. M. Lee et al., 2019). Machine learning methods can be used in chillers for early fault detection, efficiency optimization, and condition monitoring, which can help in optimizing the operating conditions of the chiller. The two methods into which the machine learning methods can be categorized into are supervised and unsupervised methods (Singh et al., 2022).

Supervised machine learning uses labeled data to train a model. Labeled data have the required faults to be classified as tagged with the associated parameters. Some supervised machine learning models include Bayesian probabilistic networks, support vector machines, and decision trees. Unsupervised machine learning uses unlabeled data for detection and diagnosis. As the data are unlabeled, they mainly rely on clustering methods to detect faults. Methods such as principal component analysis and k-means clustering are used for fault detection.

2.4.2.1 Review of Machine Learning Techniques

This section reviews the various methods developed by researchers using machine-learning-based techniques for the fault detection and diagnosis of chillers. The classification in Figure 2.3 was used as the framework to review the methods.

Methods based on probabilistic graphical models (PGMs) utilize visual representations and probability distributions to depict relationships between variables. The PGMs widely used in fault diagnosis are Hidden Markov Models (HMM) and Bayesian belief networks

(BBN). Yan et al. used Coupled Hidden Markov Models (CHMM) that combined HMM and Extended Kalman Filter (EKF) to enhance fault diagnosis, and the EKF was applied to estimate continuous fault severity in chillers and cooling towers (Y. Yan et al., 2015). Zhao et al. initially employed a BBN for the fault diagnosis of chiller units and devised a three-layer diagnostic Bayesian network (DiaBN) model. These methods have been experimentally proven successful in identifying faults with insufficient data (Zhao, Xiao, et al., 2013). To improve the fault detection and diagnosis (FDD) method for refrigeration systems, He et al. (2016) modified the Bayesian Network classifier (BNC) by implementing probability boundary constraints during normal operation, which reduced the false-alarm rate. Additionally, they addressed the problem of an increased missed detection rate (MDR) resulting from a lowered false alarm rate (FAR) by incorporating site-specific information into the BNC. Wang et al. (2017) conducted extensive research to improve the diagnostic capabilities of bayesian network (BN). They merged multi-source information and distance rejection to BN which enhanced FDD performance, and merged the BN with distance rejection, keeping the fault library updated and false alarm rate adjustable. The methodology was further applied to the field to evaluate supplemental and retained features (Z. Wang et al., 2018).

Methods based on Gaussian mixture models (GMMs) are probabilistic approaches that describe the probability distribution of a dataset as a combination of several Gaussian distributions. In the FDD context, GMMs can effectively identify unusually distributed samples by calculating the posterior probability of each data point across all Gaussian

distributions. The GMM was employed to identify the declines in the chiller energy efficiency. This demonstrates the precise identification of both severe faults and normal operations, although it occasionally misclassifies moderate faults as severe (Hu et al., 2016). An adaptive Gaussian mixture model (AGMM) was developed for FDD in nonlinear systems to detect and diagnose simultaneous faults in a water-cooled multichiller system (Karami & Wang, 2018). To create a dynamic probabilistic machine learning model for non-linear systems, they combined an AGMM with Unscented Kalman Filter (UKF) and GMM Regression. This integration results in a time-varying approach capable of handling complex non-linear data. A modified GMM was proposed, which is a supervised multi-class deep autoencoding GMM that identifies anomalies in labeled datasets for fault diagnosis in chiller systems. (Tra et al., 2022a).

K-nearest neighbor (KNN)-based methods select the k-nearest points closest to the sample. The sample was classified into classes with a maximum number of k points. KNN's accuracy of KNN is improved by applying an Extreme Learning Machine (ELM) for mapping features. A multi-label learning model was used to enhance the ELM-KNN and specific feature combinations for precise multiple fault diagnosis in chillers. The model achieves high accuracy, even with limited training data, by establishing individual fault models through multi-label learning and determining specific feature combinations for each fault.

Principal Component Analysis (PCA) is widely used as a dimensionality reduction method that uses unsupervised learning. PCA uses only the data distribution and interrelations between the features, excluding the class labels of the sample. A fault detection method for

chillers using Independent Component Analysis (ICA) to extract variable correlations and reduce data dimensionality shows better performance than PCA (P. Wang et al., 2015). The method involves preprocessing data by centering and whitening using PCA, filtering out non-steady state data, and detecting faults based on statistical thresholds. PCA identified anomalies, a reconstruction-based method isolated fault-related variables, and a decision table diagnosed faults in an experimental frictionless chiller system dataset (A. Beghi et al., 2016). Kernel Principal Component Analysis (KPCA) with genetic algorithm optimization for fault detection in complex systems, such as chillers, shows improved accuracy compared to PCA (N. Zhang et al., 2016). Refrigerant charge faults were detected using PCA, and Exponentially Weighted Moving Average (EWMA) control charts showed better efficiency than traditional methods at low fault severity levels (J. Liu et al., 2016). Fault detection methodology using local Principal Component Analysis without prior knowledge of abnormal phenomena. The performance of this approach was evaluated using a synthetic dataset under fault-free and faulty conditions (Simmini et al., 2018). An enhanced fault detection method that uses Kernel Entropy Component Analysis (KECA) for fault detection in centrifugal chillers showed better performance than traditional PCA, with fault detection ratios exceeding 55% even at low severity levels (Xia, Ding, Li, et al., 2021). Enhanced KECA and kernel density estimation were used to estimate the probability density function of the Cauchy-Schwarz divergence for fault monitoring (Xia, Ding, Jing, et al., 2021). This study investigates the creation of a self-tuning KPCA-based approach for fault detection in refrigeration systems, emphasizing the importance of steady-state functioning and the challenges of feature selection in fault-detection applications (Simmini

et al., 2022). Neural Network - Mixture Probabilistic PCA, an outlier detection method that uses a neural network-based mixture of probabilistic principal component analyzers, showed superior performance in chiller fault diagnosis (Tra et al., 2022b). A fault diagnosis method combining signal demodulation based on time-frequency analysis and Deep-PCA with a visual geometry group-PCA machine learning model was proposed for air-conditioning systems, which performed better than CNN (Song et al., 2023).

Support Vector Machine (SVM) is based on statistical learning theory. A conventional SVM was used for the binary classification tasks. However, it provides two strategies for multi-class classification: the one-against-all method and one-against-one approach. A hybrid method combining the ARX model with SVM for fault detection and diagnosis in chillers demonstrated higher accuracy and lower false alarm rates than traditional methods (K. Yan et al., 2014). An online detection method was developed that combines an Extended Kalman Filter (EKF) and a recursive one-class SVM without using faulty training data and has high accuracy rates (K. Yan et al., 2017). Bridging the divide between theoretical approaches and practical implementations, a cost-sensitive sequential feature selection algorithm was developed for chiller Fault Detection and Diagnosis (FDD) utilizing the ASHRAE dataset. Feature selection methods for chiller FDD include wrapper-based approaches, such as sequential forward feature selection (SFS) and SVM for classification (K. Yan et al., 2018). Fan et al. (2020) discussed the feasibility and enhancement of fault detection and diagnosis for chillers by using factory-installed sensors. This study explored the use of factory-installed sensors to diagnose chiller faults, highlighting the need for fault data samples and the potential for technical solutions to

increase the valid sample data. The least-squares SVM (LSSVM) optimizes fault diagnosis efficiency by creating an optimal hyperplane in a higher-dimensional space, thereby achieving high correct rates for various chiller faults (H. Han et al., 2019). The LSSVM was optimized using a gravitational search algorithm for incipient fault diagnosis in centrifugal chillers (Xia, Ding, & Jiang, 2021). A novel hybrid model using Particle Swarm Optimization-LSSVM for fault diagnosis in refrigeration systems, achieving a high diagnostic accuracy, was significantly improved from the traditional LSSVM (Ren et al., 2021). The model combines transfer component analysis (TCA) and a support vector machine with adapting decision boundaries (SVM-AD) to effectively diagnose faults in chillers, showing high accuracy in fault diagnosis when labeled target domain data are unavailable (van de Sand et al., 2021). A model with RFECV with SVM as classifier was developed for ASHRAE dataset and self-built air conditioner simulation dataset. It showed a significant reduction in diagnosis time and high overall accuracy (Nie et al., 2023).

Support Vector Regression (SVR) is a type of SVM used for regression problems. An FDD strategy for centrifugal chillers combines EWMA control charts and SVR to significantly improve FDD performance (Zhao, Wang, et al., 2013a). A chiller operation energy efficiency model using SVR optimized by the GA algorithm showed better prediction accuracy than the other models (J. Yan et al., 2014).

Support Vector Data Description (SVDD) is a type of SVM. This fault detection method uses SVDD for chiller fault detection, addressing non-Gaussian, non-linear, and wide-range process variables (Zhao, Wang, et al., 2013b). The PCA-R-SVDD algorithm offers an enhanced method for detecting early stage faults in centrifugal chillers, substantially

improving fault identification performance. This approach is effective in recognizing six common faults, detecting at least 50% of the fault data, successfully identifying a minimum of 50% of fault data, even when the fault severity is at its lowest level (G. Li et al., 2016). The Global Density-Weighted -SVDD method for chiller fault detection showed improved accuracy and reduced false alarm rates compared with conventional methods (K. Chen et al., 2021).

Artificial Neural Network (ANN) based methods are popular FDD methods. The diagnostic performance of probabilistic neural networks (PNN) and back-propagation networks (BPNN) for fault diagnosis in refrigeration systems shows that the probabilistic neural network outperformed the back-propagation network in terms of the overall diagnostic performance (Liang et al., 2018). A fault-diagnosing system for Ice-Storage Air-Conditioning Systems was proposed using an Enhanced Radial Basis Function Network combined with a Robust Quality Design to ensure normal performance and prevent equipment damage (Tien et al., 2022).

Extreme Learning Machine (ELM) provides an accelerated training strategy for neural networks. It is used in combination with big-data processing techniques to improve its effectiveness. A highly accurate fault detection technique for centrifugal chillers was developed by combining KECA with a voting-based extreme learning machine (VELM). This integrated approach demonstrated an average diagnostic precision exceeding 95%. The KECA-VELM classifier outperforms conventional methods such as BPNN, ELM, and VELM-based classifiers in identifying faults in chillers (Xia et al., 2022).

Li et al. (2023) proposed a hybrid model for diagnosing refrigerant undercharge faults in chillers using a DBN-enhanced ELM, achieving a high accuracy rate. The model combines deep learning and machine learning with parameters optimized by Particle Swarm Optimization, outperforming other models such as ELM, SVM, and KNN in terms of accuracy and robustness.

Random Forest (RF) is an ELM-based model. RF is often used in FDD for feature selection. A study utilized global sensitivity analysis employing an RF metamodel to determine the critical parameters for diagnosing chiller faults. They proposed a hybrid feature-screening strategy that significantly reduced the number of sensors while maintaining high diagnostic accuracy (Y. Gao et al., 2021). A feature importance ranking method based on random forest to enhance the fault detection and diagnosis performance of a chiller system was proposed for refrigerant faults in a variable-speed screw chiller (Lu et al., 2022). Random Forest and LightGBM were used with the Shapley Additive explanation method to uncover hidden knowledge in chiller faults, emphasizing the importance of specific features for fault detection (Y. Gao et al., 2022).

XGBoost and LightGBM are methods that are based on ensemble learning algorithms. A multi-region XGBoost model for fault detection and diagnosis in screw chillers achieves high fault detection and diagnostic accuracy (S. Zhang et al., 2021). Tree-based ensemble-learning methods and multivariate control charts have been used for fault detection and diagnosis in centrifugal chillers. The LightGBM-Multivariate Exponentially Weighted Moving Average was validated using experimental data (Yao et al., 2022).

2.4.3 Deep Learning Techniques for Fault Detection and Diagnosis

Deep learning models have complex and flexible network structures consisting of advanced feature extraction and fitting abilities. There has been an increase in deep-learning-based FDD methods in the past six years since 2018 (F. Zhang et al., 2023). Deep learning methods are reviewed based on Figure 2.3.

Deep Belief Network (DBN) consists of multiple Restricted Boltzmann machines (RBMs) stacked one upon the other. The multilayer structure acts as a feature-extraction layer that extracts high-level abstract features. A framework integrating density-based spatial clustering of applications with noise, a clustering method, and a DBN was proposed for the operational risk evaluation of screw chillers, showing superior performance compared to traditional models (X. Zhu et al., 2020). Knowledge-embedded deep belief network (DBN) method for diagnosing multiple faults in chillers. The method involves analyzing electronic-thermal and thermal faults, successfully decoupling sensor thermal faults, and integrating DBN, ELM, and KNN for diagnosis (Du, Chen, et al., 2023). A suggested technique employed a domain adaptation deep learning model, specifically DBN, to improve the generalization capabilities of ELM and KNN diagnostic models, along with Teacher-Student networks, for identifying faults in HVAC systems across various control modes and conditions (Du, Liang, et al., 2023).

A Recurrent Neural Network (RNN) was used to extract temporal information from the time-series data (Hüsken & Stagge, 2003). An RNN uses short-term memory to learn the temporal patterns in the data. Long Short Term Memory (LSTM) is an improvement on

RNN that struggles to retain long-term information owing to its susceptibility to vanishing and exploding gradients. A two-layer LSTM fault detection and diagnosis model was developed for various chiller faults, which exhibited superior performance over traditional RNN frameworks (K. Yan & Hua, 2019). An approach involving a two-stage method for condition monitoring of chillers and boilers: condition prediction and anomaly detection, with LSTM outperforming regression models such as LASSO, SVR, and MLP in predicting energy efficiency and detecting outliers or change points earlier (Y. Wang et al., 2019). A chiller fault diagnosis method uses automatic machine learning, extracts important features, and utilizes LSTM models to improve the performance (C. Tian et al., 2021).

Convolutional neural network (CNN)-based methods have gained popularity in the domain of FDD for HVAC systems. The convolution layers serve as feature extraction layers, and the fully connected layers are the diagnosis layers. CNN can be categorized into two types 1D CNN and 2D CNN based on the input data format. A fault diagnosis method for chillers was proposed using a very deep convolutional network (DCNN) with residual connections, achieving higher diagnostic accuracy compared to the traditional methods of SVDD or PCA (X. Liu et al., 2018). Miyata et al. (2020) proposed a methodology for generating a fault database through detailed simulation, training a CNN with the database, and successfully diagnosing real data with high accuracy, enabling the identification and approximate severity assessment of faults in HVAC systems. A novel fault diagnosis method was proposed for building chillers using data self-production and deep convolutional neural networks to achieve diagnostic accuracy. This method directly

transforms fault data into digitized images, avoids errors from multiple transformations, and outperforms other models in terms of diagnosis and individual fault accuracy (J. Gao et al., 2021). An explainable 1D CNN method for fault diagnosis in chillers was developed by visualizing the fault diagnosis criteria using Grad-Absolute-CAM (G. Li et al., 2021). Chiller fault detection and diagnosis using a 1D CNN-based approach has been proposed for chillers and shows improved accuracy compared to SVM, DT, and LightBGM (K. Yan & Zhou, 2022). This research introduces an enhanced Layer-wise Relevance Propagation technique to interpret CNN fault diagnosis models in chillers and identify the features that best contribute to the fault diagnosis of each fault (G. Li, Wang, et al., 2023). A method was proposed that uses interpretable mechanism mining by simulating fault experiments on different chillers, training a 1D-CNN for fault detection, using Score-CAM for interpretability, extracting key variables, and retraining the model for transfer applications (K. Chen et al., 2023).

An unsupervised deep learning technique known as an autoencoder (AE) is employed to extract complex features that encapsulate the essence of the input data representation. A Deep-AE model effectively detects and isolates faults in chiller systems by differentiating between small reconstruction errors for normal data and large errors for abnormal data (Cheng et al., 2021). Autoencoder-based fault detection and diagnosis methods were compared using residual matrix (REM) and latent space matrix (LSM), showing that LSM-based models outperform REM-based models (Choi & Yoon, 2021). A study focusing on the utilization of AE and interpretable AI, specifically SHAP, for fault detection and

diagnosis in industrial chillers showed reliable results and effective visualizations (Gupta et al., 2022).

A generative adversarial network (GAN) is a data generation model that addresses the issue of insufficient or unbalanced data. A study focusing on using a Generative Adversarial Network (GAN) to tackle the issue of class imbalance in fault detection and diagnosis of chillers in HVAC systems showed improved classification accuracy compared with traditional methods (K. Yan et al., 2020). A variational autoencoder-based conditional Wasserstein GAN with a gradient penalty (CWGAN-GP-VAE) was developed for chiller fault diagnosis to address the challenge of insufficient training data (K. Yan et al., 2022). A partially supervised, data-driven approach for detecting chiller malfunctions combines labeled and unlabeled information, substantially enhancing the precision of fault identification (B. Li et al., 2021). proposed a GAN-based chiller FDD framework with GANomaly, which achieved the highest accuracy in fault detection with a small amount of real fault data. Yan (2021) introduced a FDD framework for chillers utilizing a GAN-based approach with GANomaly. This method demonstrated high accuracy in identifying faults, while requiring only a limited amount of authentic fault data.

Transfer learning (TL)-based methods use existing knowledge obtained from trained models for one task and apply it to another task within the same domain. A methodology for transferring fault detection and diagnosis (FDD) knowledge from one chiller to another, thus improving energy efficiency, has been applied (X. Zhu et al., 2021). Liu et al. (2021) investigated various scenarios and training strategies using a transfer learning-based FDD method on an experimental dataset of two water-cooled chillers. This study explores how

energy conservation can be attained using AI to identify and diagnose faults within refrigeration systems. The method uses ASHRAE 1043 data to train and auto-scale TL to diagnose target chillers with varying cooling capacities (D. Lee et al., 2022). Deep-TL combines deep learning with transfer learning to address data distribution challenges in Building Energy Systems (BESs) and investigates three main strategies: network-based fine-tuning (FT), mapping-based domain-adaptive neural network (DaNN), and adversarial-based domain adversarial neural network (DANN) (G. Li, Chen, et al., 2023)

A hybrid AI model is a combination of multiple independent AI models. Hybrid models can utilize the abilities of more than one model, thereby creating a capable FDD. One such hybrid model, consisting of a 1D-CNN and GRU, displays superior performance in identifying minor faults compared to other algorithms (Z. Wang et al., 2020). This approach combines physics-based models with data-driven models of an air filter in an HVAC system to enhance system reliability, reduce life cycle costs, and improve sustainability by providing crucial information on system health status (Gálvez et al., 2021). The FDD method combines a HVAC system simulation model with LSTM-SVDD to address the delayed manifestation of faults and insufficient system-fault operational data. (H. Zhu et al., 2022). An approach for identifying multiple faults in chillers utilizing multi-label learning and a specialized feature combination-enhanced ELM-KNN model demonstrated high accuracy in detecting multiple faults, even with limited training datasets (P. Li et al., 2022). An end-to-end chiller FDD method combines a 1D-CNN and LSTM for feature extraction, incorporates a fused attention mechanism for feature refinement, and utilizes dynamic cross-entropy for real-time imbalance factor adjustment, resulting in enhanced

diagnostic performance (S. Han et al., 2022). A framework consisting of an autoencoder, classifier, and thresholder components with various deep and shallow model combinations had been tested for fault prediction efficacy (Zhanhong Jiang et al., 2023).

2.5 Challenges in Data-Driven Techniques

Challenges identified for data-driven methods are discussed below.

I. New/ Unknown faults

As expected, data-driven methods rely largely on the data used to build the models. The majority of studies use ASHRAEs experimental data, which includes seven types of faults and one simultaneous fault. Hence, models were developed and fine-tuned to detect and diagnose these types of singular fault.

II. Transient data

Most studies used steady-state data to develop FDD systems. Transient data are also a part of the operation of a chiller. Incorporating transient data in this study will provide more characteristics to FDD and make it more applicable to the real world.

III. Limited real-world data

Real-world complexities, such as multiple simultaneous faults or new, unknown faults, are not fully captured in laboratory or simulated data with existing datasets, such as those from ASHRAE, which lack these scenarios. It is difficult to obtain fault data from actual HVAC systems, leading to skewed datasets for normal operating data. A majority (63%) of the building managers surveyed found integrating automated fault detection and diagnostics (AFDD) tools into their

operations challenging, primarily because of the lack of standardized data access (Hacker et al.). Despite this, more than 90% recognized the potential of AFDD tools to reduce energy and operational costs. The main hurdle highlighted is the collection of accurate training data for developing these tools, which is an expensive and time-consuming process fraught with potential labeling errors. Gradual faults that reduce efficiency may not be immediately detectable, affecting operational quality, and possibly user comfort and energy efficiency. Recent efforts have been made to standardize data access, which could address some barriers to adoption.

IV. Limited data

Data-driven methods are data-hungry algorithms that require large amounts of variable data. As mentioned earlier, only a limited number of public datasets are available to researchers. The creation and planning of these datasets can be expensive and time consuming. Some sophisticated deep learning methods, such as GAN, have been proven to be effective in data mining but are computationally expensive.

There is a significant problem with the variable severity of the faults. Machine learning models trained on data from faults at one severity level struggle to identify the same fault when it is present at a different severity level, posing a challenge for reliable fault diagnosis across a spectrum of fault severities.

V. Reliability

The reliability of data-driven methods for building energy system fault detection and diagnostics (FDD) is questioned because of the tendency of models to be overfitted to training data, leading to false alarms during normal variations in performance, maintenance, and component replacements. Optimizing model parameters for specific datasets yields high performance on test and training data but raises doubts about the models' generalization capabilities in practical settings. Generalization in machine learning is a recognized problem, as noted in previous studies (D. Lee et al., 2021). While substantial research has focused on specific structures or predetermined datasets, there is a scarcity of studies examining models intended for broad application across diverse building layouts (Jin Wen & Shun Li, 2012). Moreover, models developed for a single dataset may exhibit high accuracy, which is not replicable for other datasets.

VI. Interpretability

The ease of understanding or interpretability is crucial for marketable fault detection and diagnostic (FDD) products. Decision makers prioritize the understanding of the specific features that influence the FDD model's performance and the underlying mechanism. This knowledge helps pinpoint the exact issue within the fault-diagnosis process, allowing for targeted problem-solving. Although conventional machine learning techniques, such as Bayesian Networks (BN) and Decision Trees (DT), offer some level of interpretability, they struggle to effectively manage intricate FDD tasks. Conversely, deep learning models excel in complex faults but lack interpretability owing to their layered structures. Efforts to enhance

deep learning interpretability are ongoing, with strategies divided into ante-hoc and post-hoc approaches, as documented in the literature (Bi et al., 2024).

2.6 Recent Advances and Future Trends

Advances in technology have enabled higher computational power and vast data storage solutions. These advances have led to the development of complex FDD methods.

Advancements and future trends in FDD for chillers are discussed below.

2.6.1 Overview of Recent Advancements

Data-driven methods for data generation, feature extraction, high-precision model training, and cross-system transfer performed well. Ongoing enhancement of deep-learning algorithms is necessary to create a robust online fault-monitoring system capable of adapting to dynamic systems. Wang et al. (2023) used an evolutionary learning-based FDD method for HVAC systems. This method is a continuous learning method that updates the changing performance of the system.

Such FDD systems require collection of large quantities of data over an extended period. The IoT ecosystem encompasses a vast network of interconnected devices numbering billions. IoT data can be managed, stored, and operated using cloud-computing services. Cloud computing operates over the Internet; hence, nothing is conducted on the local hard drive. Therefore, IoT and cloud computing work hand-in-hand and are the most useful when implemented together. FDD) of chillers can be enhanced through the implementation of cloud-based Internet of Things (IoT) technology. The IoT infrastructure enables the gathering of equipment data that can subsequently be stored and analyzed in cloud-based

systems. IoT devices at the edge detect faults, whereas cloud platforms handle data processing and analysis, reducing computational stress and network bandwidth consumption. Edge computing in IoT devices accelerates computational efficiency and reduces cloud server workloads, making fault diagnosis more efficient and real-time. A cloud-based IoT server is utilized in an automated lighting and ventilation system that incorporates numerous sensors and actuators. This embedded system, which employs the HTTP protocol, logs and updates sensor data through a cloud platform (Mahbub et al., 2020).

2.6.2 Predictions and Future Trends

A physical model based on the first-principles equation can be generalized (Shohet et al., 2020). The development of such models involves intricate mathematical processes and poses significant challenges. Implementing such models within a system requires specialized expertise. Hybrid models that combine the advantages of the generalizability of the physical model and ease of configuration of data-driven models should be explored further.

The integration of physical models with AI models has been proposed and is known as physical-informed neural network (PINN) and physical-informed machine learning (PIML). Physical knowledge is typically applied at a shallow level in feature engineering or data processing. PINN and PIML are applied at a deeper level, such as in artificial intelligence model design and training. Chen et al. and Wang et al. successfully implemented PINN in HVAC systems (2023; 2023).

Online FDD systems that actively learn from the system, such as variable normal operating conditions, and it is difficult to detect faults such as sensor drift, have the potential to better understand chiller behavior over extended time periods. The integration of technologies, such as IoT, cloud computing, and big data analytics, can be incorporated to collect data from more than one system and to learn, develop, and deploy FDD systems to collect chiller systems.

2.7 Research Gaps and Conclusion

Machine-learning models are interpretable, have fast training speeds, and require less data for training. These models struggle to handle large-scale high-dimensional data processing. Deep learning models can handle large-scale, high-dimensional, and non-linear data. Deep learning methods require a large number of samples to establish complex model relationships, which increases computing requirements. Deep learning methods can be used in time-series modeling, image processing, and knowledge transfer and have been shown to be beneficial for FDD applications.

Some research gaps that have been identified in the literature and the thesis aim to address are as follows.

- I. The majority of FDDs use steady-state filters for preprocessing. Hence, these models were trained using the steady-state data. There has been no investigation of the effects of training a model with steady state versus transient data. This study would help to understand if preprocessing with steady-state filters is worth the

computational cost, and if transient data help identify faults with low severity levels.

- II. The predominant approach for developing FDD systems for chillers involves utilizing the experimental data sourced from ASHRAE RP-1043. Notably, there is a lack of studies investigating the use of simulated data to augment the dataset's diversity.
- III. However, many studies have not tested these methods using unseen data. Unseen data, such as operating conditions, near-normal conditions, and data containing different fault severity levels than those of the FDD methods. These conditions reflect real-life scenarios, which should be studied for practical applications.

The data utilized for the development of data-driven FDD techniques is of crucial importance. The nature of the data used for FDD techniques determines the feasibility and practicality of using them in real-world applications. This thesis endeavors to address some of the variability issues present in the datasets commonly employed for FDD techniques. This thesis describes the use of steady-state and transient data in the development of FDD techniques. Furthermore, we discuss how simulation data can be utilized to supplement the experimental datasets. It is hoped that some of the insights from this thesis will assist future researchers in considering other scenarios in which a data-driven FDD system must be capable of accommodating real-world situations.

3. ASHRAE dataset

ASHRAE RP- 1043 project is a publicly accessible project developed by ASHRAE to study faults in a centrifugal vapor chiller and provides data to researchers to develop fault detection and diagnosis (FDD) methods. This project entailed the development and validation of a vapor-compression chiller model that could capture the transience of the system. The model can simulate the start-up and load change transients. The model can also replicate certain faults at various severity levels. A set of experiments was designed to study the normal operation under different operating conditions and induced faults at different severity levels.

This thesis utilizes ASHRAE RP- 1043 resources to develop and study FDD methods. This section provides a brief overview of the system and the experiments conducted on the chiller and the model developed for this chiller. A chiller model was used to simulate additional data to supplement the study in this thesis.

3.1 System description

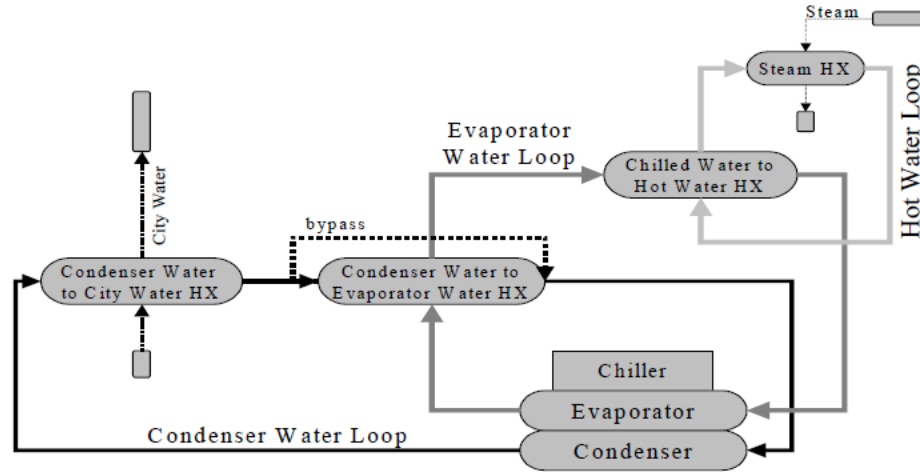


Figure 3.1: Schematic of Simplified Water Flow Diagram of Chiller Test Stand (Mathew C. Comstock, 1999)

The setup for the experiment was a McQuay PEH048J 90-ton chiller. The system consists of a centrifugal compressor, evaporator, condenser, and an expansion valve. The capacity of the chiller was controlled by changing the angle of the guide vane present at the inlet of the compressor. The refrigerant used in the chiller was R134a and the secondary fluid was water. Water-to-water and water-to-steam heat exchangers were arranged as substitutes for actual buildings and ambient loads.

The chiller test stand had three water loops: hot water, evaporator water, and condenser water. The hot water loop contained two heat exchangers: a steam heat exchanger that extracted heat from the steam and a chilled water heat exchanger. This heat exchanger extracts heat from the hot water loop into the chilled water coming from the evaporator.

The evaporator water loop consists of chilled water to a hot water heat exchanger, condenser water to evaporator water heat exchanger and evaporator. The evaporator lowered the inlet water temperature. The heat from the condenser is rejected into the chilled water at the condenser to the evaporator heat exchanger. This heated evaporator water extracts more heat from the hot-water loop in the chilled water to the hot-water heat exchanger. The water at the inlet of the evaporator was changed by operating valves in the steam circuit, hot water, and evaporator water loops.

The condenser water loop comprised condenser water to the city water heat exchanger, condenser water to the evaporator water heat exchanger and condenser. The heat dissipated by the evaporator is absorbed by the water in the condenser. Some of this heat is then rejected into the city water using the condenser water to city water heat exchanger. The warm condenser water goes through further cooling of the condenser water to the evaporator water heat exchangers. The valves present in the condenser water loop, city water, and bypass line of the shared heat exchanger were used to control the condenser inlet water temperature.

The condenser and evaporator used in the experiment were flood-type, 2 pass shell and tube-type heat exchangers. The tube contained the refrigerant, and the shell had water entering through the bottom and exiting from the top of the shell. A centrifugal-type compressor with a 4.8” impeller was used. The impeller ran at 32000 rpm and was driven by a constant-speed electric motor. The expansion valve is a system comprising a main valve, liquid line, and pilot valve. The thermostatic expansion valve contained R500 in the bulb, which controlled the opening and closing of the main valve.

3.2 ASHRAE RP-1043 data set

The following sections briefly explain the ASHRAE RP-1043 project, including the experiments conducted and model developed based on the experimental setup. These subsections are followed by the simulation data set generated using the model developed in the project.

3.2.1 Experiment

Experiments have been conducted to create a database for researchers to develop FDD methods or to verify their methods using a database (Satyam Bendapudi, 2002). The experimental work consisted of the following categories:

- Faults were instigated at four severity levels.
- The faults were conducted at different operating conditions
- 8 chiller faults were performed for each chiller loading
- Sensor data were gathered from the chiller at a sampling rate that ensured capture of the transience of the system.
- A typical building installation was replicated in the test unit.

The database consists of 66 features, some of which were measured or calculated using VisSim¹, as detailed in Table 3.1. The features observe various points of the chiller as well as the secondary loop, which substitutes for the building load variations. The temperature, pressure, flow rate, voltage, current, and valve positions were measured. The calculated

¹ VisSim is a visual block diagram program which is used for simulation of dynamical system and model based design of embedded system (*Visual Environment Software for Embedded Systems* | Altair Embed, n.d.). VisSim can be integrated in control system design and digital signal processing.

values include the heat rejection rate, energy balance of the heat exchangers, and approach temperatures. The test sequence consisted of 27 operating conditions running sequentially. The data were collected at 10 sec and 2 min intervals. A complete test run took 14 h with a start-up time and attained a steady state for each operating condition.

Table 3.1: List of features from experimental test runs (Comstock, Matthew C. & Braun, James E., 1999)

Designation	Source	Description	Units
Time (minutes)	VisSim	Real time counter	Seconds
TWE set	MicroTech	Chilled water setpoint—control variable	F
TEI	JCI AHU (RTD)	Temperature of Evaporator Water In	F
TWEI	MicroTech (Thermistor)	Temperature of Evaporator Water In	F
TEO	JCI AHU (RTD)	Temperature of Evaporator Water Out	F
TWEO	MicroTech (Thermistor)	Temperature of Evaporator Water Out	F
TCI	JCI AHU (RTD)	Temperature of Condenser Water In	F
TWCI	MicroTech (Thermistor)	Temperature of Condenser Water In	F
TCO	JCI AHU (RTD)	Temperature of Condenser Water Out	F
TWCO	MicroTech (Thermistor)	Temperature of Condenser Water Out	F
TSI	JCI AHU (RTD)	Temperature of Shared HX Water In (in Condenser Water Loop)	F
TSO	JCI AHU (RTD)	Temperature of Shared HX Water Out (in Condenser Water Loop)	F
TBI	JCI AHU (RTD)	Temperature of Building Water In (in Evaporator Water Loop)	F
TBO	JCI AHU (RTD)	Temperature of Building Water Out (in Evaporator Water Loop)	F
Cond Tons	VisSim	Calculated Condenser Heat Rejection Rate	Tons
Cooling Tons	VisSim	Calculated City Water Cooling Rate	Tons
Shared Cond Tons	VisSim	Calculated Shared HX Heat Transfer (only valid with no water bypass)	Tons

Cond Energy Balance	VisSim	Calculated 1st Law Energy Balance for Condenser Water Loop (only valid with no water bypass)	Tons
Evap Tons	VisSim	Calculated Evaporator Cooling Rate	Tons
Shared Evap Tons	VisSim	Calculated Shared HX Heat Transfer (should equal Shared Cond Tons with no water bypass)	Tons
Building Tons	VisSim	Calculated Steam Heating Load	Tons
Evap Energy Balance	VisSim	Calculated 1st Law Energy Balance for Evaporator Water Loop	Tons
kW	JCI AHU	Watt Transducer Measuring Instantaneous Compressor Power	kW
COP	VisSim	Calculated Coefficient of Performance	--
kW/Ton	VisSim	Calculated Compressor Efficiency	kW/ton
FWC	JCI AHU	Flow Rate of Condenser Water	GPM
FWE	JCI AHU	Flow Rate of Evaporator Water	GPM
TEA	MicroTech	Evaporator Approach Temperature	F
TCA	MicroTech	Condenser Approach Temperature	F
TRE	MicroTech	Saturated Refrigerant Temperature in Evaporator	F
PRE	MicroTech	Pressure of Refrigerant in Evaporator	PSIG
TRC	MicroTech	Saturated Refrigerant Temperature in Condenser	F
PRC	MicroTech	Pressure of Refrigerant in Condenser	PSIG
TRC_sub	MicroTech	Liquid-line Refrigerant Subcooling from Condenser	F
T_suc	MicroTech	Refrigerant Suction Temperature	F
Tsh_suc	MicroTech	Refrigerant Suction Superheat Temperature	F
TR_dis	MicroTech	Refrigerant Discharge Temperature	F
Tsh_dis	MicroTech	Refrigerant Discharge Superheat Temperature	F
P_lift	MicroTech	Pressure Lift Across Compressor	PSI
Amps	MicroTech	Current Draw Across One Leg of Motor Input	Amps
RLA%	MicroTech	Percent of Maximum Rated Load Amps	%
Heat Balance (kW)	VisSim	Calculated 1st Law Energy Balance for Chiller	kW
Heat Balance%	VisSim	Calculated 1st Law Energy Balance for Chiller	%
Tolerance%	VisSim	Calculated Heat Balance Tolerance According to ARI 550	%
Unit Status	MicroTech		0-27
Active Fault	MicroTech		0-44
TO_sump	MicroTech	Temperature of Oil in Sump	F
TO_feed	MicroTech	Temperature of Oil Feed	F
PO_feed	MicroTech	Pressure of Oil Feed	PSIG
PO_net	MicroTech	Oil Feed minus Oil Vent Pressure	PSI
TWCD	MicroTech	Condenser Water Temperature Delta	F
TWED	MicroTech	Evaporator Water Temperature Delta	F

VSS	JCI AHU	Small Steam Valve Position	%Open
VSL	JCI AHU	Large Steam Valve Position	%Open
VH	JCI AHU	Hot Water Valve Position	%Open
VM	JCI AHU	3-way Mixing Valve Position	%Mix
VC	JCI AHU	Condenser Valve Position	%Open
VE	JCI AHU	Evaporator Valve Position	%Open
VW	JCI AHU	City Water Valve Position	%Open
TWI	JCI AHU (RTD)	Temperature of City Water In	F
TWO	JCI AHU (RTD)	Temperature of City Water Out	F
THI	JCI AHU (RTD)	Temperature of Hot Water In	GPM
THO	JCI AHU (RTD)	Temperature of Hot Water Out	F
FWW	VisSim	Calculated City Water Flow Rate	GPM
FWH	VisSim	Calculated Hot Water Flow Rate	GPM
FWB	VisSim	Calculated Condenser Water Bypass Flow Rate	GPM

There were 48 sensors placed in the chiller and water loops. The refrigerant loop has pressure sensors that measure the high and low pressures on the condenser and evaporator sides. The refrigerant temperatures were measured using a MicroTech instrument (*Controls, Settings, And Functions; 200 Series Microtech Control Panel - McQuay PFS 155C Operation And Maintenance Manual [Page 15], n.d.*) in Fahrenheit. The saturated temperatures of the refrigerants in the condenser and evaporator were measured, along with the subcooled and superheated temperatures. The temperatures at the discharge and suction points of the compressor are measured. There are sensors present in the water loop that measure the temperatures across the condenser and evaporator, as well as the shared heat exchangers present in other water loops. Water flow rates are measured in condenser, evaporator as well as from the supply of the city water.

Prior to testing, all sensors on the test stand underwent calibration. In contrast, calibration was only possible for the pressure transducers located on the chiller. The ASHRAE RP-1043 reported uncertainties in the measured and calculated variables. The measurements with the most significant uncertainties were evaporator approach temperature at 4-10%, kW/ton at 4-5%, liquid subcooling at 5-15%, suction superheat at 5-25% and condenser approach temperature 8-25%. Variations in uncertainties occur owing to substantial changes in measurements across different operating conditions.

Table 3.2: Steady- state conditions matrix (Mathew C. Comstock, 1999)

Test	TWE_set	TCI	TEI
1	50	85.46	60.44
2	50	85.19	56.96
3	50	85.16	53.76
4	49	75.54	61.07
5	50	75.31	56.42
6	50	75.15	53.05
7	49	70.57	59.14
8	50	65.29	55.99
9	50	62.39	53.63
10	44	85.00	55.08
11	45	85.40	51.94
12	45	85.19	48.82
13	44	75.20	56.19
14	44	74.97	50.69
15	45	74.90	48.10
16	44	70.04	55.63
17	44	64.47	51.00
18	45	64.68	48.13
19	39	79.94	50.01
20	40	80.13	46.71
21	40	80.10	43.89
22	39	69.71	51.41
23	39	69.32	45.72

24	40	69.26	43.21
25	39	66.01	50.08
26	40	65.03	47.20
27	40	65.04	43.65

Different operating conditions can be achieved in the chiller by controlling three input temperatures of the chiller: the set-point temperature (TWE_set), condenser water inlet temperature (TWCI, TCI), and evaporator water inlet temperature (TEI, TWEI). TWE_set changed the least number of times. While TWE_set and TCI are kept constant, the system achieves a steady-state for every change in the TEI, as shown in Table 3.2. This strategy was repeated three times to change the TCI. This resulted in a test sequence for a fixed TWE_set, with nine test runs. This format was used twice more at two different TWE_set values, resulting in 27 operating conditions.

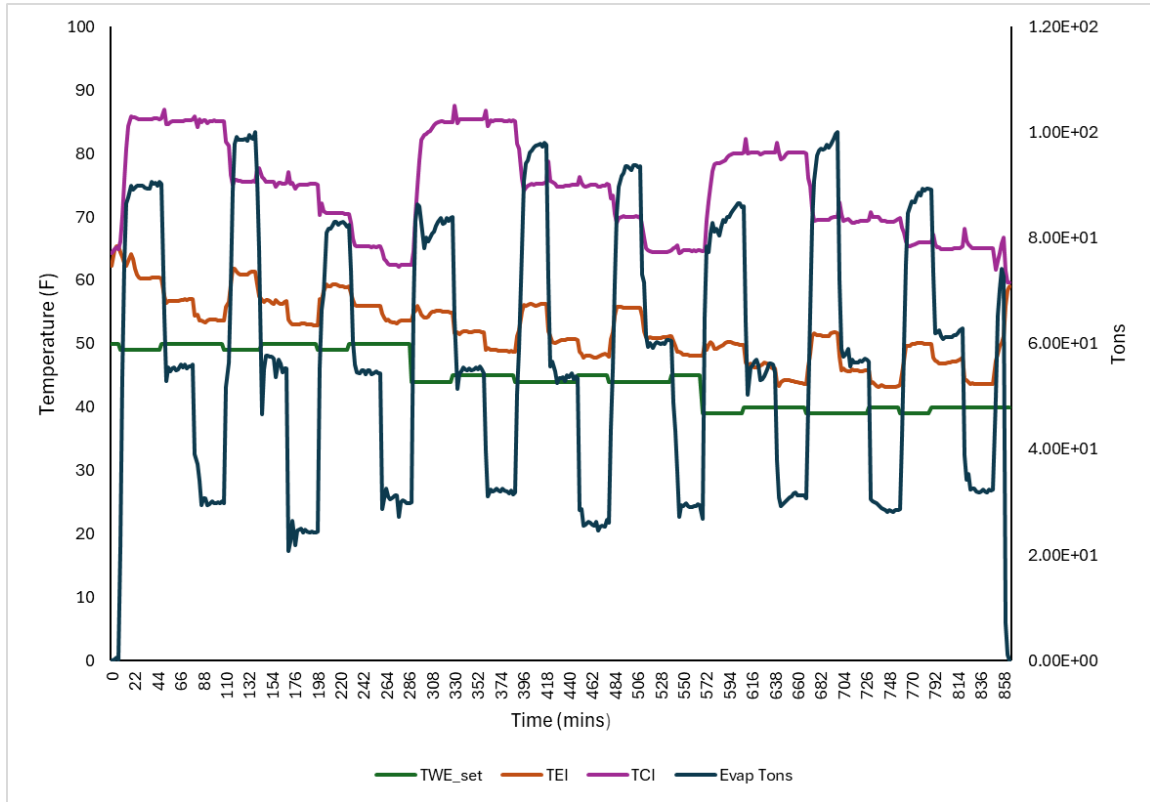


Figure 3.2: One Test cycle of ASHRAE experiment

Figure 3.2 represents one full test cycle. The test cycle required 14 h to complete. The load on the chiller was changed after a steady-state was achieved for the operating conditions. This load change is reflected in the EvapTons parameter shown in Figure 3.2. TEI is changed most often, as illustrated in Figure 3.2, and Table 3.2. Each test was run for 30 min in both transient and steady-state conditions. These 27 operating conditions were applied consecutively.

Table 3.3: Types of faults tested for ASHRAE RP 1043 (Mathew C. Comstock, 1999)

Sr. No.	Fault	Severity Levels
1	Reduced Condenser Water Flow	10% , 20%, 30%, 40%
2	Reduced Evaporator Water Flow	10% , 20%, 30%, 40%
3	Refrigerant Leak	10% , 20%, 30%, 40%
4	Refrigerant Overcharge	10% , 20%, 30%, 40%
5	Excess Oil	14%, 32%, 50%, 68%
6	Condenser Fouling	12%, 20%, 30%, 45%
7	Non-Condensables in Refrigerant	1%, 2%, 3%, 5%

The most frequently occurring faults were observed in chillers. Each fault was replicated in the system at four severity levels as listed in Table 3.3. The reduced condenser and evaporator water flow-rate faults were reproduced by controlling the valves present in the water loops. The condenser was fouled by blocking the tubes in the shell-tube heat exchangers, thereby reducing the overall heat transfer area. Refrigerant leakage and overcharging were performed by extracting and adding more refrigerant to the chiller.

3.2.2 ASHRAE chiller model

A vapor-compression centrifugal liquid chiller system was modelled to study the performance of the system under different conditions. The model considers various components of the system, including the evaporator, condenser, compressor, and expansion

valve. It uses inputs such as evaporator pressure, inlet enthalpy, condenser pressure, and chilled water temperature to calculate outputs such as refrigerant enthalpy at compressor discharge, refrigerant flow rate, motor power, and electromechanical losses. The model incorporates both quasi-steady-state and two-dimensional solutions to represent the behavior of the system accurately. The model also includes a simplified model of the expansion valve that uses a lumped-capacitance element to represent the bulb. Overall, the model provides a comprehensive understanding of the dynamic performance of the system and can be used to study trends and predict response times and steady-state values.

The model was implemented using the C++ programming language and executed in MATLAB. It is designed to be modular in component models, allowing easy integration and analysis. The model considered various dynamics, such as the refrigerant redistribution between heat exchangers and the thermal capacitance of the tube material.

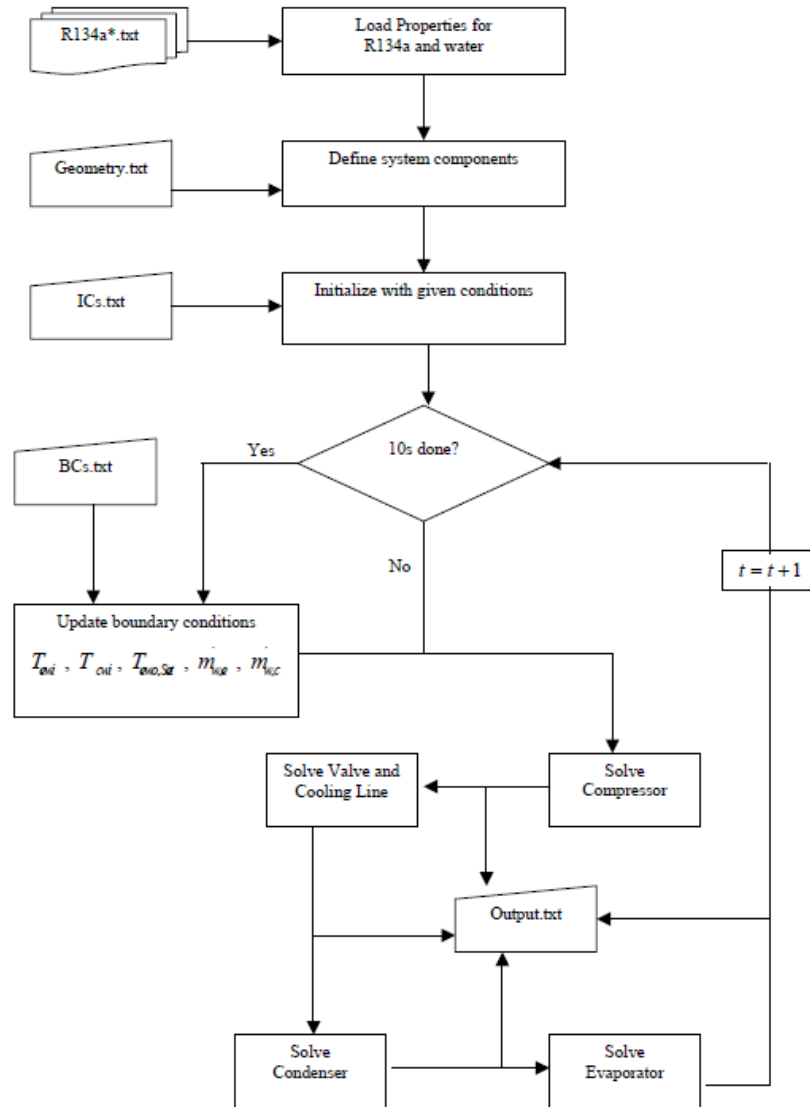


Figure 3.3: Model description flow chart (Satyam Bendapudi, 2002)

Figure 3.3 illustrates the model flow chart and flow of information across each module.

Compressor Model: The compressor model takes inputs such as evaporator pressure, inlet enthalpy, condenser pressure, and chilled water temperature error. The system generates data on the compressor discharge refrigerant enthalpy, rate of refrigerant flow, power consumption of the motor, and losses related to the electromechanical processes. The model

uses a quasi-steady-state approach when the current drawn by the motor is below the limit, and a two-dimensional solution when the limit is reached.

Expansion Valve Model: A simplified standard thermostatic expansion valve is used in the system model. The bulb of the expansion valve was modelled as a lumped-capacitance element. The bulb contained R500. The superheat pressure balances the evaporator pressure of R500 to control the valve opening. The model includes the refrigerant mass in the bulb, thermal mass of the bulb body, and heat transfer resistance on either side of the bulb body.

Cooling Line Model: The cooling line model represents a small bypass line that carries the liquid refrigerant to the motor and transmission housing. This model calculates the enthalpy at the evaporator inlet using the electromechanical losses derived from the compressor model.

Condenser Model: Utilizing the revised compressor and valve flow rates, along with the compressor exit enthalpy, the condenser model calculated solutions for the equations. the condenser pressure and enthalpy distribution were determined at the end of 1sec using an explicit Euler one-step correction method.

Evaporator Model: The evaporator model is similar to the condenser model and solves the equations using the updated evaporator pressure and enthalpy distribution. Using the same explicit Euler one-step correction technique, the evaporator pressure and enthalpy distributions were calculated after 1 second.

These models, along with the valve and cooling line models, were employed forward in time, using an explicit algorithm within a nested solution loop. The loop updated the boundary conditions and solved the equations for each component at 1second intervals.

The model was validated using data from a 90-ton McQuay chiller under various conditions including fault-free operation, reduced flow rates, refrigerant charge, and fouling in the condenser. This method can be employed to analyze the patterns in the operating parameters of systems and predict the response times and steady-state values. However, there are some areas for improvement, such as incorporating a more accurate expansion valve model and refining the correlations used to estimate the condenser heat transfer coefficient.

3.2.3 Simulation dataset

CNN requires a large number of samples. A diverse dataset containing various scenarios and variations in the input data is often beneficial for training a robust model. Although the experiments involved a series of transients followed by steady states, the steady-state data were insufficient for use as input for the CNN. To address this deficiency, the use of simulated data generated using the ASHRAE chiller model is proposed.

The ASHRAE model includes three inputs that can be used to set the different operating conditions for the chiller. The inputs were the temperature of the evaporator inlet (TEI), temperature of the condenser inlet (TCI), and set-point temperature of the chiller (Tset). The 27 operating conditions of the ASHRAE experiment were taken as reference

temperatures (RT), and variations in this temperature were used to create new operating conditions for the simulation dataset, as shown in Table 3.4.

Table 3.4: Operating conditions for simulated data

Sr. no.	Tset (°C)	TEI(°C)	TCI(°C)
1	RT+1	RT+1	RT+1
2	RT+1	RT+0	RT+0
3	RT+0	RT+1	RT+0
4	RT+0	RT+0	RT+1
5	RT-1	RT-1	RT-1
6	RT-1	RT-0	RT-0
7	RT-0	RT-1	RT-0
8	RT-0	RT-0	RT-1
9	RT+2	RT+2	RT+2
10	RT+2	RT+0	RT+0
11	RT+0	RT+2	RT+0
12	RT+0	RT+0	RT+2
13	RT-2	RT-2	RT-2
14	RT-2	RT-0	RT-0
15	RT-0	RT-2	RT-0
16	RT-0	RT-0	RT-2

Table 3.4 lists the 16 operating conditions based on the 27 experimental cooperating conditions. Hence each class contains 432 operating conditions, that is, Normal, reduced condenser water, reduced evaporator water, refrigerant overcharge, refrigerant leakage, condenser fouling. The reference temperature (RT) corresponded to the same parameters used in the experiments as listed in Table 3.2.

Table 3.5: Faults simulated in chiller model

Class name	Fault
0	Normal
1	Reduced Condenser Water flow rate

2	Reduced Evaporator Water flow rate
3	Refrigerant Overcharge
4	Refrigerant Leakage
5	Condenser Fouling

Five faults were selected from the seven faults used in the experiments, as listed in Table 3.5. These faults can be simulated using the ASHRAE model by manipulating various inputs. Reduced condenser and evaporator water faults were produced by altering the water flow rate parameter, which was used as the input to the model. Refrigerant leakage and overcharge were simulated by changing the amount of refrigerant present in the chiller. Condenser fouling was captured by inputting a fouling factor as one of the coefficients used to calculate the heat-transfer coefficients for the condenser. Each fault was simulated at three severity levels: 10, 20, and 30%. Faults of 5%, 15%, and 25% were also simulated for operating conditions 1-4.

3.3 Summary

This chapter describes the ASHRAE RP-1043 project and briefly outlines the experimental setup, test cycles, faulty experiments, and ASHRAE model. Experimental data are used to study the AI methods for FDD, which are explored in Chapter 4. The simulated data generated using the ASHRAE model were used to enrich the dataset and study the impact of the simulated and experimental data on the FDD methods.

4. Establishment of FDD methods

This section discusses various machine learning and deep learning methods for dimensionality reduction and classification. A hybrid model was proposed to study the performance of different methods for diagnosing chiller faults using time-series data from ASHRAE RP-1043. Methods for converting 1D time-series data into 2D images have been explored. A deviation strategy that can capture fault patterns is proposed.

4.1 Hybrid network

A hybrid network architecture was proposed, comprising a feature generation section and classification section. It can incorporate various dimension reduction methods and classifiers. Feature generation was performed via dimensionality reduction. A method based on machine learning and deep learning was chosen, and similarly for the classifiers. Hybrid networks provide the flexibility to combine different methods and study the best combination of methods for a task.

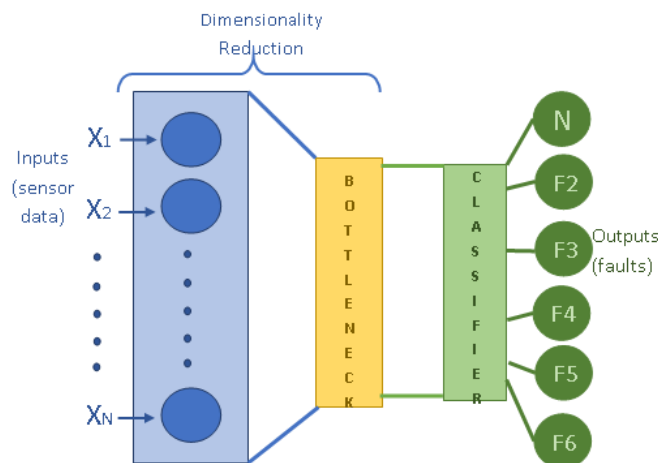


Figure 4.1: Hybrid network architecture

Figure 4.1 illustrates the architecture of a hybrid network. The input layer receives sensor data which is compressed using dimensionality reduction methods. The bottleneck layer represents the compressed data which would then be inputted into the classifier. The classification algorithm will then detect and diagnose the faults.

The network was implemented in the Google Colab environment using Python 3.10. Deep-learning methods use the Keras package to build the model.

4.1.1 Dimensionality Reduction

Dimensionality reduction techniques are commonly used in machine learning and data analysis to decrease the number of features or variables in a dataset, while preserving the most significant information. These methods are particularly advantageous for addressing problems, such as improving computational efficiency and increasing interpretability. The following is a concise overview of some frequently used dimensionality reduction approaches.

1. **Principal Component Analysis (PCA):** Principal Component Analysis (PCA) is a commonly employed linear method that transforms features into a set of orthogonal variables known as principal components. These components can be used as dimensionality reduction methods, as they can capture the maximum variance in the data, thus preserving most of its information. (Jolliffe, 1986).
2. **t-Distributed Stochastic Neighbor Embedding (t-SNE):** t-SNE is an efficient non-linear dimensionality reduction technique that effectively visualizes high-dimensional data in a lower-dimensional space while maintaining local

relationships among data points. This makes it suitable for identifying clusters and patterns in data (Maaten & Hinton, 2008).

3. **Uniform Manifold Approximation and Projection (UMAP):** UMAP is a non-linear dimensionality reduction algorithm that is well-known for its capacity to capture intricate patterns in high-dimensional data. This algorithm is particularly beneficial for visualizing and clustering data points in a lower-dimensional space, as demonstrated by McInnes et al. (2018).
4. **Autoencoders:** Autoencoders are a specific type of neural network designed to facilitate unsupervised learning of efficient data representations. The encoder component of the autoencoder is responsible for compressing the input data into a lower-dimensional representation, whereas the decoder component reconstructs the original data. Autoencoders are particularly effective in learning non-linear and hierarchical feature representations (Hinton & Salakhutdinov, 2006).
5. **Factor Analysis:** Factor analysis is a statistical technique that uses linear combinations of unobserved latent variables to explain the observed variables. The goal was to identify the common variance among the observed variables and reduce the dimensionality of the data by representing it in terms of fewer factors (Bartholomew et al., 2011).

Various techniques for reducing dimensionality provide different strategies for managing data with many dimensions. The selection of the most appropriate method depends on the specific features of the dataset and the intended outcomes of the analysis.

PCA and Autoencoder were chosen for dimensionality reduction on the experimental dataset of ASHRAE RP- 1043. PCA was chosen as the machine learning algorithm because it is a commonly used dimensionality reduction method. This helps to study the variance among the datasets and identify important features in the experimental dataset. Long Short Term Memory Autoencoder (LSTM-AE) was chosen as the deep-learning counterpart for dimensionality reduction. LSTM- AE is a type of autoencoder that utilizes the temporal dependencies of the experimental dataset for effective dimensional reduction.

4.1.1.1 PCA

PCA was used for exploratory data analysis and predictive models. This method is frequently employed to reduce dimensionality by mapping data points onto a limited number of principal components. This process creates lower-dimensional data while maximizing the preservation of data variability. Smaller datasets are easier to explore, visualize, and analyze data much easier and faster for machine learning algorithms without extraneous variables to process.

The following steps explain the basic implementation of the PCA.

1. Standardize the Data:

The data were standardized with a mean of 0 and a standard deviation of 1. This ensured that all the features contributed equally to the analysis.

$$X_{standardized} = \frac{X - \mu}{\sigma} \quad 4.1$$

where μ is the mean and σ is the standard deviation.

2. Compute Covariance Matrix

The PCA computes the covariance matrix of the standardized data. The relationships among the various features within the dataset were captured using the covariance matrix.

$$\text{Covariance matrix } \Sigma = \frac{1}{n} X_{standardised}^T X_{standardised} \quad 4.2$$

where, n is the number of samples.

3. Eigenvalue Decomposition

The next step involves performing eigenvalue decomposition on the covariance matrix.

This results in eigenvalues λ and the corresponding eigenvectors v

$$\Sigma v = \lambda v \quad 4.3$$

4. Select Principal Components:

The principal components are formed by selecting the top-k eigenvectors corresponding to the largest eigenvalues, which are listed in the decreasing order. These principal components represent the directions of the maximum variance in the data.

5. Transform the Data:

The original standardized data were multiplied by the selected principal components to obtain a lower-dimensional representation of the data.

$$X_{transformed} = X_{standardised} \cdot v_k \quad 4.4$$

where, v_k is the matrix of the top k eigenvectors.

PCA applied on ASHRAE 1043 experimental data set

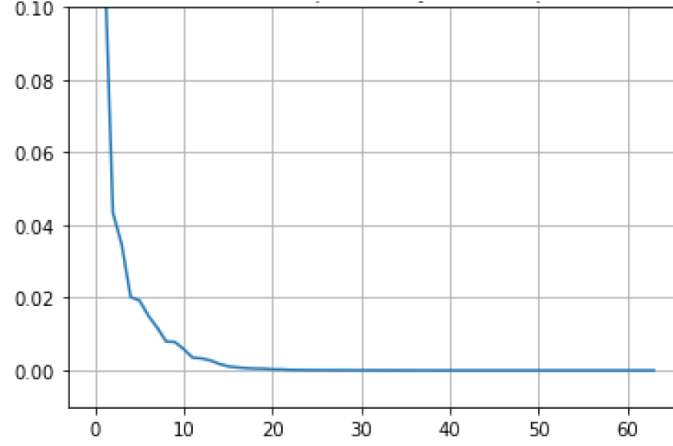


Figure 4.2: Variance ratio of 65 features using PCA

PCA was applied to the ASHRAE experimental dataset consisting of 65 features. Figure 4.2 illustrates the variance ratios of the 66 components. The variance ratio is the ratio of the eigenvalue of the principal component to the sum of the eigenvalues of all the principal components, as represented in Eqn 4.5. 15 components captured the maximum variance of the dataset at 0.995.

$$Variance\ ratio_i = \frac{\lambda_i}{\lambda_1 + \lambda_2 + \lambda_3 + \dots \lambda_n} \quad 4.5$$

Where, λ_i is the eigenvalue of related principal component

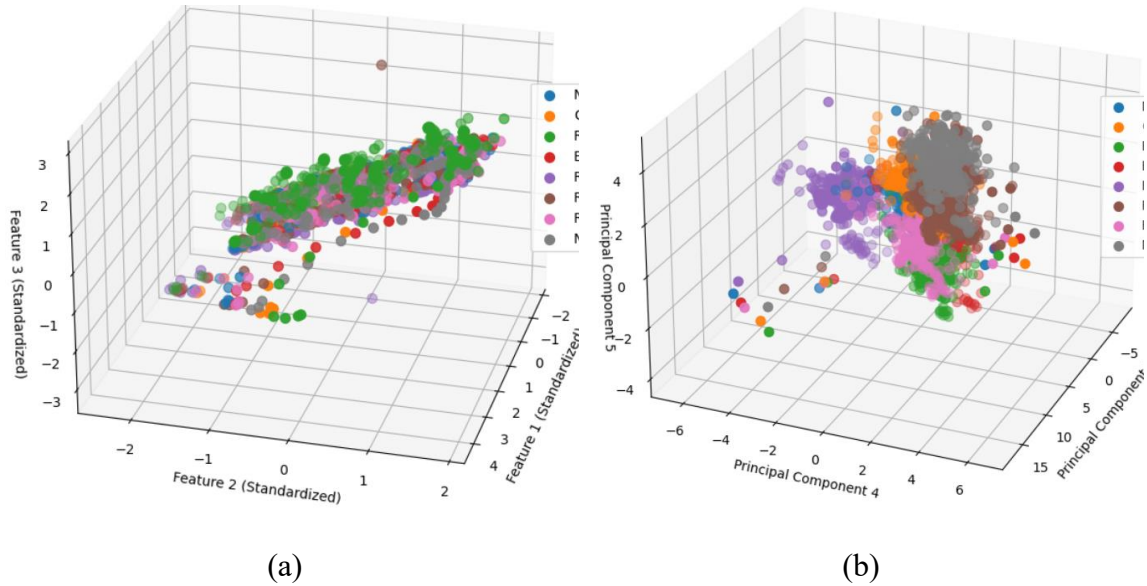


Figure 4.3 (a): Data points before PCA (b) Data points after applying PCA
The legend shows eight classes N-Normal, CF-Condenser Fouling, RCW-Reduced Condenser Water Flow, EO-Excess Oil, REW-Reduced Water Flow, RO-Refrigerant Overcharge, RL-Refrigerant Leakage, NC- Non-Condensable

Figure 4.3 (a) shows a 3D plot of the three features, TEI, TEO, and TCO (see Table 3.1), which represent the temperature of water at different locations in the evaporator and condenser. Figure 4.3 (b) shows 3D plots of PC 3, 4, and 5. These PCs were chosen for the purpose of illustration as the class clusters were best visible for them. The plot shows clusters for all classes, thus helping build effective classifiers.

4.1.1.2 LSTM-AE

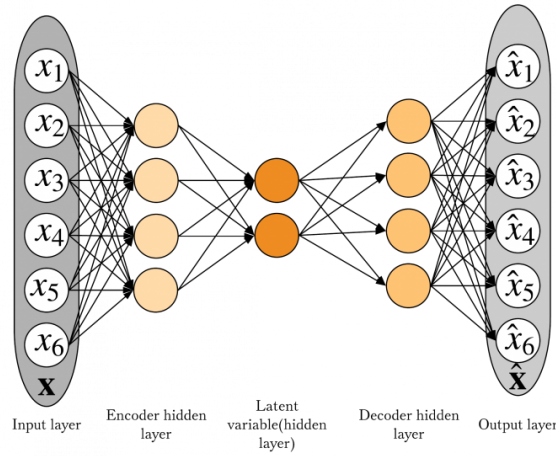


Figure 4.4: Autoencoder structure

An autoencoder (AE) is an ANN consisting of two parts: an encoder and decoder. The encoder consisted of an input layer and more than one hidden layer. The encoder functions as a latent variable or bottleneck, with a decreasing number of neurons, as shown in Figure 4.3. The encoder layer compresses the data by reducing dimensionality and removing redundancies. The decoder then attempts to reconstruct the data from the bottleneck. The reconstructed data had the same dimensionality as that of the input data. The autoencoder uses unsupervised training data, which are unlabeled data, to train the network. Once the autoencoder is trained, it can be separated and used only for data compression.

A LSTM-AE is a type of autoencoder that consists of an LSTM-type neural network in the autoencoder architecture. It is used for sequence modeling and feature extraction, particularly in the domain of sequential data such as time series or natural language processing. This approach merges the capabilities of LSTM networks, which are capable of recognizing long-term patterns in sequential information (H. Zhu et al., 2022), with the

principles of autoencoders, which are neural networks engineered to extract meaningful representations from input data (C. Tian et al., 2021). LSTM-AEs have been successfully applied in various domains such as natural language processing, time-series analysis, and speech recognition. Their ability to capture long-term patterns and develop multilevel representations makes them well-suited for tasks involving sequential data.

LSTM AE applied on data set

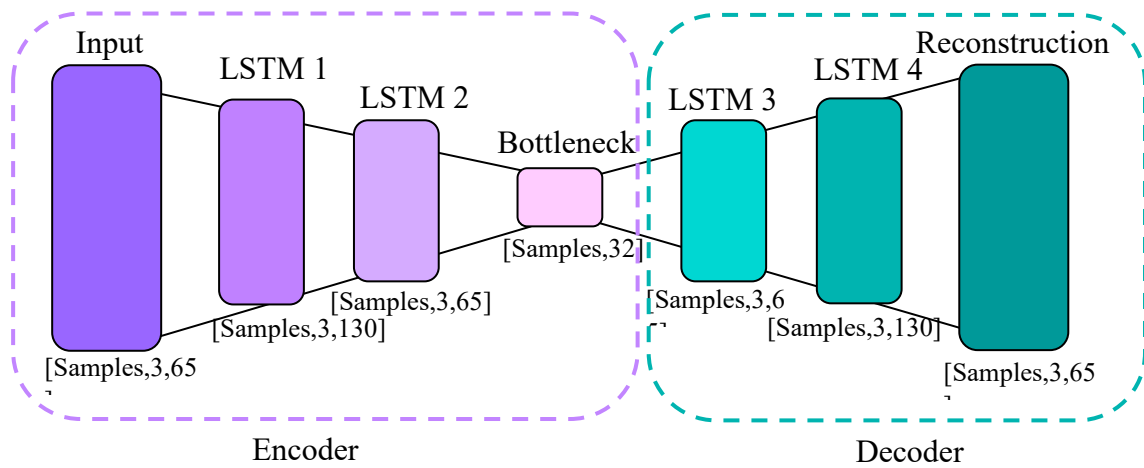


Figure 4.5: LSTM AE architecture

The LSTM-AE was configured with an input layer with the same number of units as the dimension of the input variable, which was 65 in this case. This autoencoder comprises five hidden layers with dimensions of 130, 65, 32, 65, and 130 and an output layer with 66 variables. The error of the autoencoder was calculated using Eqn 4.6, which calculates the mean absolute error (MAE) of the reconstruction.

$$MAE = \frac{1}{n} \sum_{i=1}^n |y_i - \hat{y}_i| \quad 4.6$$

Where,

n is number of samples

y_i is true value

\hat{y}_i is predicted value (reconstructed value)

The autoencoder's minimum MAE for the reconstruction was found to be 32 variables at the bottleneck. Each layer was followed by a dropout layer at 0.2 to prevent overfitting the model.

The network used an unsupervised training method. The layers are activated using ‘reLu’ and the model is optimized using ‘adam’ and training loss is calculated using ‘mse.’

4.1.2 Classifiers

Classifiers are machine learning and statistical algorithms that categorize data into labeled classes based on the features and attributes of the dataset. These algorithms learn the patterns and relationships between the features of the dataset. Once trained, they can predict the class of unseen data. Classifiers can be trained on either labeled or unlabeled datasets, and their effectiveness depends on the quality and quantity of training data used.

Classifiers can be broadly categorized into two types: supervised and unsupervised.

- Supervised classification

The supervised classification approach requires a labeled dataset that incorporates the features or attributes of the instances in tandem with their respective classes. The algorithm learns to associate the features with their corresponding classes. After the classifier has been adequately trained, it can accurately forecast the class labels of unseen instances. Common examples of supervised classifiers include decision trees, support vector machines (SVM), naive Bayes, logistic regression, random forests, and neural networks.

- Unsupervised classification

Unsupervised classification algorithms utilize unlabeled datasets by grouping data points to form clusters based on their inherent structures. These algorithms identify patterns or similarities between instances. Common examples include k-means clustering, hierarchical clustering, and Gaussian mixture models.

The classifiers were chosen based on the nature, size, computational resources, and specific requirements of the task. The Support Vector Machine (SVM) and Artificial Neural Network (ANN) were the two classifiers chosen for our study. SVM was chosen as the machine learning algorithm, and ANN was chosen as the DL algorithm for comparison.

4.1.2.1 SVM

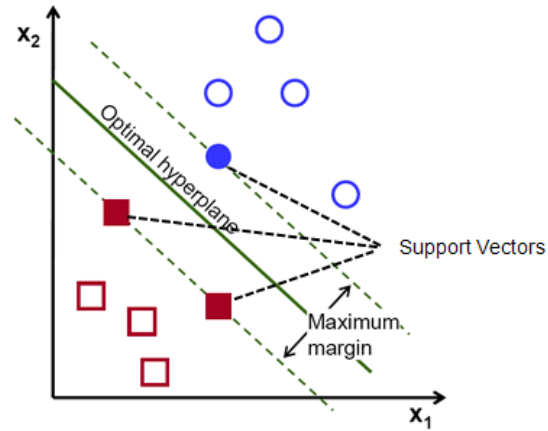


Figure 4.6: SVM data plot

Support Vector Machine (SVM) is a supervised machine learning method that employs specific algorithms to examine data for classification and regression purposes. This method uses a model trained on labeled data to perform analysis tasks. The SVM algorithm constructs a hyperplane in high-dimensional space. The plane was constructed to have the maximum distance between the data points, as shown in Figure 4.6. The data points closest to the hyperplane are known as support vectors. These support vectors influence the position and orientation of the hyperplane and help maximize the margin of the classifier. These points helped to build the SVM.

Vapnik et al. (1995) developed statistical learning theory. SVM methodology provides a simplified understanding of this theory. The following presentation of the methodology was adapted from Guo et al. (2005).

Consider a vector $x \in R^n$ that represents a pattern to be classified. Vector x_i is labeled with either class $y_i \in \{\pm 1\}$. Let there be l training examples $\{(x_i, y_i), i = 1, 2, \dots, l\}$. The SVM maps x to a higher dimensional space \mathcal{H} using a non-linear operator $\Phi(\cdot): R^n \rightarrow \mathcal{H}$. The non-linear SVM classifier is defined as follows.

$$f(x) = w^T \Phi(x) + b, w \in \mathcal{H}, b \in R \quad 4.7$$

The transformed data $\Phi(x)$ exhibited linearity, whereas the original data $x \in R^n$ exhibited non-linearity. The SVM classifier utilizes a hyperplane that optimizes the separation margin between the two classes, as illustrated in Figure 4.6. When the training set cannot be fully separated in \mathcal{H} owing to a partial class overlap, a slack variable ξ_i is introduced to generalize the analysis. The SVM algorithm aims to minimize $\|w\|$ while categorizing data with the least number of possible errors.

Mathematically, minimize

$$J(w, \xi) = \frac{1}{2} \|w\|^2 + C \sum_{i=1}^l \xi_i \quad 4.8$$

With $\xi_i \geq 0$ satisfying the constraint:

$$y_i(w^T \Phi(x_i) + b) \geq 1 - \xi_i, i = 1, 2, \dots, l \quad 4.9$$

The regularization parameter C balances the trade-off between the model complexity and training error, ensuring optimal generalization performance.

Using the method of Lagrange multipliers, minimizing $J(w, \xi)$

Minimizing $J(w, \xi)$ using a Lagrange multiplier gives a vector w that forms a linear combination of mapped vectors $\Phi(x_i)$.

$$w = \sum_{i=1}^l \alpha_i y_i \Phi(x_i) \quad 4.10$$

where $\alpha_i \geq 0$ and $i = 1, 2, \dots, l$ are the Lagrange multipliers linked to the constraints in Eqn. 4.9. The Lagrange multipliers $\alpha_i \geq 0, i = 1, 2, \dots, l$ are solved using the dual form of Eqn. 4.11, which is

$$\max W(\alpha_1, \alpha_2, \dots, \alpha_l) = \sum_{i=1}^l \alpha - \frac{1}{2} \sum_{i=1}^l \sum_{j=1}^l \alpha_i \alpha_j y_i y_j K(x_i, x_j) \quad 4.11$$

Subject to

$$0 \leq \alpha_i \leq C, i = 1, 2, \dots, l$$

$$\sum_{i=1}^l \alpha_i y_i = 0 \quad 4.12$$

To transform the input vector into a high-dimensional feature space, a kernel function was employed. Some common types of kernel functions include the Gaussian Radial Basis Function (RBF), Polynomial, Sigmoidal, and Inverse multi quadratic. Polynomial and radial basis functions were selected for this study. These are defined as follows:

$$\text{Polynomial kernel: } K(x, y) = ((x \cdot y) + 1)^p \quad 4.13$$

$$\text{Gaussian RBF kernel: } K(x, y) = \exp\left(\frac{-||x-y||^2}{\sigma}\right) \quad 4.14$$

where $\sigma \in R$, the width of the RBF function, $p \in N$, degree of the polynomial function.

SVM applied on datasets

The SVM, used as a multi-class classifier, was trained on the ASHRAE experimental dataset. SVM parameters were obtained by conducting a grid search². The parameters that were searched were C for 0.1, 1, 10, 100, and 1000; gamma for 1, 0.1, 0.01, 0.001, and 0.0001; and kernel for RBF and polynomial. Gamma values are used to determine the extent to which the training samples affect the model. The model used five folds for each of the 25 candidates for a total of 125 fits. The best parameters obtained after the grid search were $C = 1000$, $\gamma = 0.001$, and kernel = RBF.

4.1.2.2 ANN

The design of Artificial Neural Networks (ANNs) is based on the organization and operations of biological neural networks. ANNs are composed of interconnected nodes or artificial neurons arranged in multiple layers, mirroring the structure of the neurons in the human brain. Artificial neurons are the fundamental building blocks of ANNs. These neurons process inputs from multiple neurons by applying weights, summing the results,

² Grid search refers to the method where in all the values in hyper parameter of a method are arranged in a grid form. The method is tested against all possible combinations of values in hyper-parameters. The combination of values achieving the best performance of the method by assessing the maximum training accuracy is then recommended for further application.

and transmitting the outcome to one or more additional neurons. In certain cases, artificial neurons employ an activation function to modify the output before relaying it to the next variable.

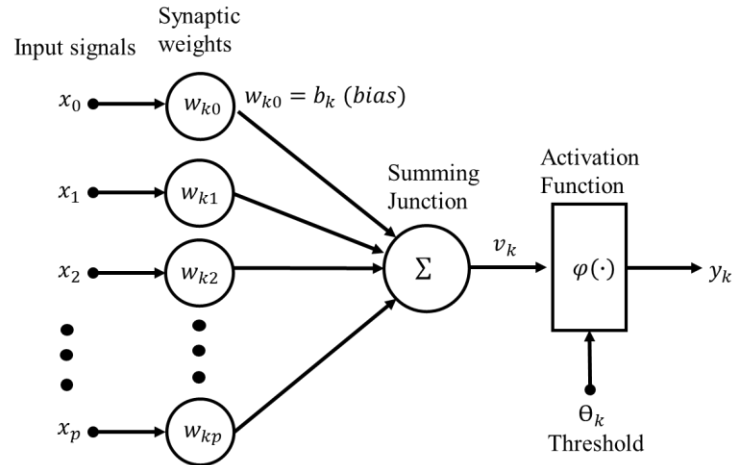


Figure 4.7: A single neuron architecture

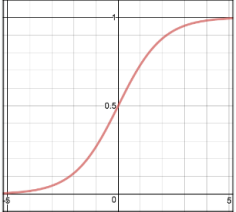
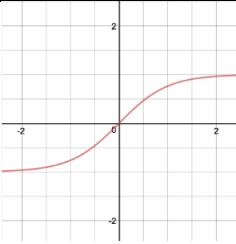
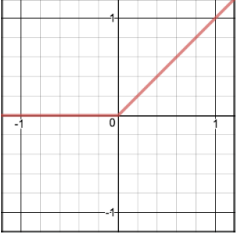
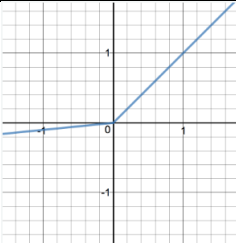
The components of the neurons illustrated in Figure 4.7 represent biological neurons. Artificial neuron k has $p+1$ inputs with signals $x_0, x_1, x_2, \dots, x_p$ and weights $w_{k0}, w_{k1}, w_{k2}, \dots, w_{kp}$. Usually, the x_0 input is assigned the value $+1$, thus making it a bias input. Hence, p actual inputs are available to the neuron.

The output of the summation junction in neuron is:

$$v_k = \varphi\left(\sum_{j=0}^p w_{kj}x_j\right) \quad 4.15$$

Nonlinearity is introduced into the neuron by the activation function, which helps to model complex input-output relationships. Table 4.1 presents several widely used activation functions, including the sigmoid function, hyperbolic tangent (tanh) function, rectified linear unit (ReLU), leaky ReLU, and softmax functions.

Table 4.1 : List of activation functions

Activation function	Plot	Equation
Sigmoid		$\varphi(v) = \frac{1}{1 + e^{-v}}$
Tanh		$\tanh(v) = \frac{e^v - e^{-v}}{e^v + e^{-v}}$
ReLU		$f(v) = \max(0, v)$
Leaky ReLU		$f(v) = \begin{cases} v & \text{if } v > 0 \\ \alpha v & \text{if } v \leq 0 \end{cases}$

Softmax		$\varphi(v_i) = \frac{e^{v_j}}{\sum_{k=1}^N e^{v_k}}$
---------	--	---

The activation function was chosen based on the type and range of the dataset, as each function has its own advantages and disadvantages. The function should satisfy the requirements of the task and the network architecture.

A neural network consists of three interconnected layers of neurons: input, hidden, and output layers. The movement of data from the input layer to the output layer and back helps the network learn more about the data and provides the desired output.

The forward propagation network computes information from the input layer to the output layer via the hidden layers in one direction. The output is calculated using the weights and biases applied to the input along with the activation function.

Back-propagation neural networks are popular algorithms that use training algorithms. After the initial forward run, a loss function, which is the error between the predicted and true outputs, is calculated. The gradient is a measure of the change in the loss function, which is calculated for every forward run. The weights of the neural network are adjusted based on gradient descent, which is an algorithm that minimizes the loss function. The weights were iteratively adjusted by following the negative gradient of the loss function until minimum loss was attained. Thus, a highly optimized neural network with a feedback loop was achieved.

ANN applied on ASHRAE dataset

The neural network used as the classifier had an input layer with 32 variables and two hidden layers with 50 and 40 nodes, respectively, as illustrated in Figure 4.8. The ANN

architecture is achieved by starting with one hidden layer. The hidden layers were added individually until a significant increase in the test accuracy was noted. A dropout layer with 0.2 rate was used after the first hidden layer to prevent overfitting. Each hidden layer used a reLU as the activation function. The output layer has eight variables, and the network classifies the eight classes. The model was compiled using the loss function of sparse categorical cross-entropy (Z. Wang et al., 2020), and the loss optimizer used was stochastic gradient descent (SGD) (Léo Bottou, 1998). The model was fitted for 200 epochs with a batch size of 32. The training and validation losses were monitored and both learning curves converged steadily in four separate model runs. This suggests that the model had a good fit.

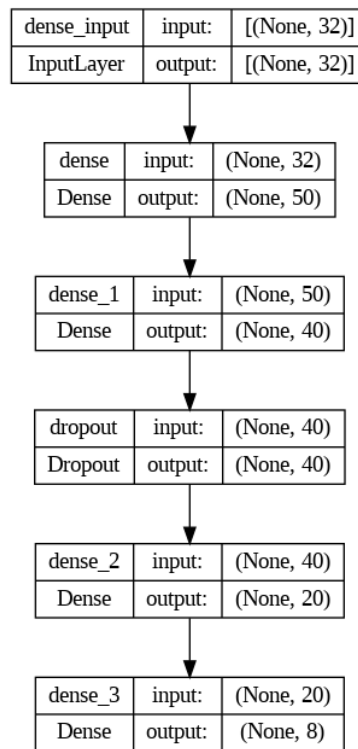


Figure 4.8: ANN architecture

4.2 CNN

A CNN is a deep learning algorithm that uses repeated application of filters on the input to generate a feature map. This feature map was used as an input to a fully connected neural network to classify the images. As illustrated in Figure 4.9, the CNN architecture comprises an input layer, output layer, and several hidden layers. These hidden layers contain multiple convolutional, pooling, and fully connected layers. The convolution layers consist of a kernel that scans a multi-dimensional array from left to right. This feature extraction method is commonly used for image preprocessing. It calculates the dot product between the numerical values of the input array and kernel. The dot product is fed into the output array. A pooling layer was used to reduce the spatial size of the feature maps. This reduces the dimensionality, thus lowering the computational requirements. Additionally, it helps in extracting key features that remain consistent regardless of the rotation or position, thereby enhancing the model's training effectiveness. A fully connected layer is a fully connected neural network that receives input from the flattened layer and learns the possible non-linear functions in that space. The neural network is a feed-forward network with backpropagation applied in every training iteration. Using softmax classification, the model can differentiate between dominant and low-level features in the images. There are various CNN architectures such as LeNet, AlexNet, VGGNet, GogLeNet, ResNet, and ZFNet.

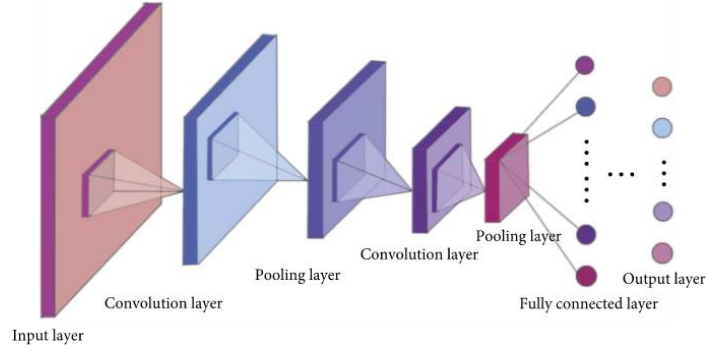


Figure 4.9: Convolutional Neural Network architecture(K. Chen et al., 2019)

There are two types of CNN-based FDD methods: 1D and 2D CNN. The 1D CNN has fewer complex models, thereby decreasing the computation and fewer training parameters. 2D requires more data-processing steps for conversion. The 2D structure can capture spatial information, which helps extract a pattern that explains the relations between the cells of the matrix. Therefore, a 2D CNN was selected to implement the FDD system.

- Convolution Layer

The convolution operation is expressed by Eqn. 4.15. Consider I as the input image, and filter (kernel) K with dimensions $k_1 \times k_2$. The convolution operation is represented (Goodfellow et al., 2016)

$$(I * K)_{ij} = \sum_{m=0}^{k_1-1} \sum_{n=0}^{k_2-1} I(i+m, j+n)K(m, n) \quad 4.15$$

Consider a CNN with input map I , filters K , and bias b . Let in the input image have height H , width W , and channels $C=3$ such that $I \in \mathbb{R}^{H \times W \times C}$. The output of this convolution operation is

$$(I * K)_{ij} = \sum_{m=0}^{k_1-1} \sum_{n=0}^{k_2-1} \sum_{c=1}^C K_{m,n,c} \cdot I_{i+m,j+n,c} + b \quad 4.16$$

Considering that the image is grayscale, $C=1$ eqn.4.13 modifies

$$(I * K)_{ij} = \sum_{m=0}^{k_1-1} \sum_{n=0}^{k_2-1} K_{m,n} \cdot I_{i+m,j+n} + b \quad 4.17$$

Eqn 4.14 can be rewritten for multiple convolutional layers as follows:

$$x_{i,j}^l = \sum_m \sum_n w_{m,n}^l o_{i+m,j+n}^{l-1} + b^l \quad 4.18$$

Where:

l is the current convolution layer

x is input of dimension $H \times W$, i and j as iterators

$w_{m,n}^l$ is the weight matrix of dimension $k_1 \times k_2$ has m and n are iterators connecting neurons between layers l and $l-1$.

b^l is bias at layer l

$$o_{i,j}^l = f(x_{i,j}^l) \quad 4.19$$

Where,

$o_{i,j}^l$ is the output layer at layer l

$f()$ is activation function

- Pooling layer

Pooling layers were implemented in the CNN to reduce data dimensionality. It can be applied as a local or global pooling layer after a convolutional layer. Local pooling was applied to the clusters. Global pooling was applied to all neurons. Max pooling and average pooling are the two most commonly used pooling methods. In max pooling, the highest value within each cluster is selected, whereas average pooling computes the mean value for each cluster.

- Fully connected layers

The fully connected layers constitute the final stage of the CNN. After the feature extraction step, the feature maps were flattened to 1 D vector to be input into the fully connected layer. This layer connects every neuron in one layer to every neuron in another layer. The output of this layer was the identification of classes.

4.2.1 CNN structure for dataset

The CNN model built for the FDD is illustrated in Figure 4.10. A CNN consists of two convolutional layers and a global max-pooling layer. The input layer had dimensions of (5,4,1). Convolutional layers 1 and 2 have eight filters of sizes 3 and 4, respectively. The

convolutional layer was activated using the tanh function. The convolutional layer is followed by a global max-pooling layer. Two fully connected dense layers were used after the pooling layer to flatten and classify the feature maps. The last dense layer uses softmax activation for classification. The model was compiled using the Adam optimizer and sparse categorical cross-entropy was used as the loss function.

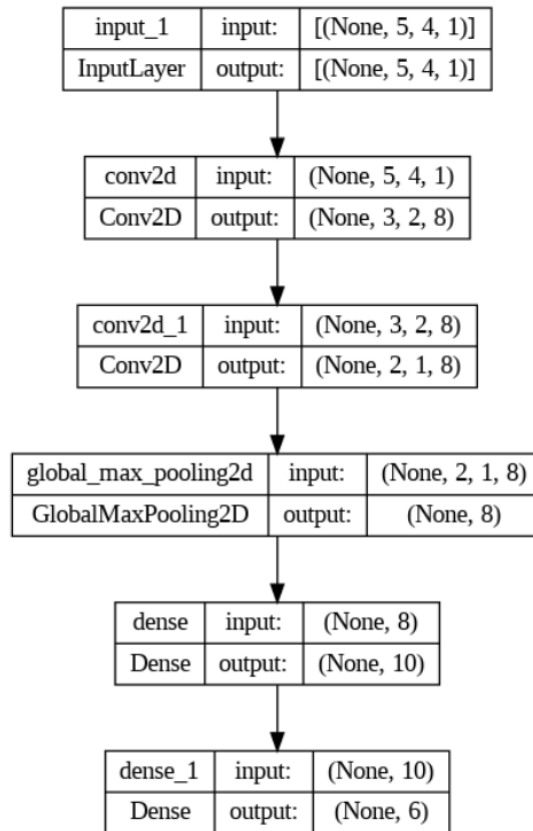


Figure 4.10: CNN architecture for fault classification

4.2.2 2D input creation method

A time-series is a set of sequential data points listed at specific time intervals. The dataset used in these studies had multiple features recorded at each time interval, which is known

as a multivariate time series. Time series data are usually in 1D form, because each row is a time stamp with multiple columns as different features. The case study used a 2D CNN for feature extraction, thus requiring the conversion of a 1D time-series to 2D matrices or images.

Markov Transient Field (MTF) and Gramian Angular Summation Field (GASF) are two methods investigated for 1D to 2D conversion. The methods were applied to ASHRAE RP-1043 (Chapter 3.2.1), and the challenges of the application were explained. A deviation strategy was proposed to address the shortcomings of the procedure.

4.2.2.1 Markov Transition Field

The Markov Transition Field (MTF) is based on a Markov Matrix, and a square matrix describes the transitions of the Markov chain (Z. Wang & Oates, 2014). This matrix describes the probability of moving from one state to another in a dynamic system. Given a time series X , the values were discretized into Q bins.

Each x_i is assigned to the corresponding bins q_i ($j \in [1, Q]$). A weighted adjacency matrix W of $Q \times Q$ dimension is created. This matrix is formed by tallying the transitions between quantile bins, following the principles of a first-order Markov chain for each time step.

Example: A sine wave is considered a time-series example. 200 time points i.e. x_i is used to construct the time series. It is discretized into three bins as illustrated in Figure 4.11.

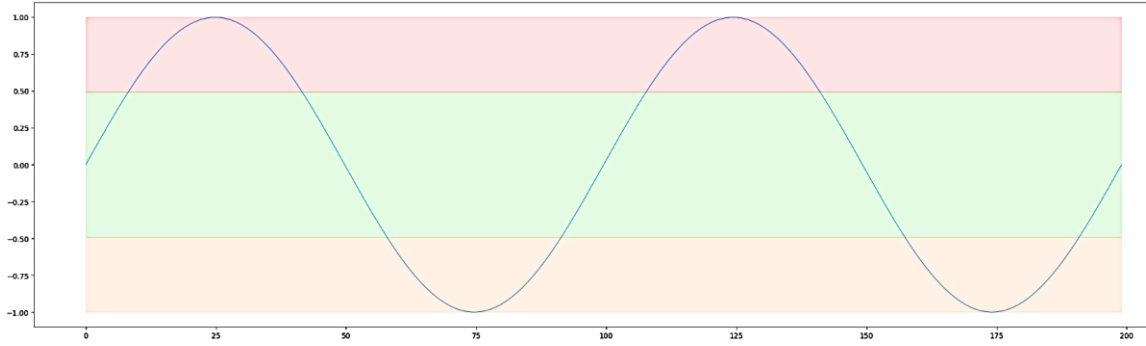


Figure 4.11: Sine wave with three quantile bins

In Matrix W , the element w_{ij} represents the occurrence rate at which a data point in quantile q_j is succeeded by a data point in quantile q_i .

$$W = \begin{bmatrix} w_{11|P(x_t \in q_1 | x_{t-1} \in q_1)} & \cdots & w_{1Q|P(x_t \in q_1 | x_{t-1} \in q_Q)} \\ \vdots & \ddots & \vdots \\ w_{Q1|P(x_t \in q_Q | x_{t-1} \in q_1)} & \cdots & w_{QQ|P(x_t \in q_Q | x_{t-1} \in q_Q)} \end{bmatrix} \quad 4.20$$

Example: Implementing eqn 6.20 to the example time series

$$W = \begin{bmatrix} 65 & 2 & 0 \\ 2 & 61 & 2 \\ 0 & 2 & 65 \end{bmatrix}$$

The distribution of the time series and temporal dependencies on the time step do not affect the Markov Transition Matrix. Therefore, the information is lost in the matrix W . MTF overcomes this limitation by allocating probability from each quantile at time step i to the quantile at time step j for every element M_{ij} of the MTF.

In the Markov Transition Field (MTF), M_{ij} signifies the probability of transitioning from q_i to q_j . MTF M captures the multi-span transition probabilities of the time series by allocating the probability from the quantile at time step i to the quantile at time step j for each pixel M_{ij} . The transition probability between points separated by time interval k is denoted as $M_{i,j||i-j|=k}$. The principal diagonal, M_{ii} , represents a special case where $k = 0$, and

measures the probability of a quantile transitioning to itself (self-transition probability) at time step i .

$$M = \begin{bmatrix} w_{ij|x_1 \in q_1, x_1 \in q_j} & \cdots & w_{ij|x_1 \in q_1, x_n \in q_j} \\ \vdots & \ddots & \vdots \\ w_{ij|x_n \in q_i, x_1 \in q_j} & \cdots & w_{ij|x_n \in q_1, x_n \in q_j} \end{bmatrix} \quad 4.21$$

Example: The sine wave time series consists of 200 time steps ($n=200$). Therefore, the MTF matrix had a size of 200×200 .

$$M = \begin{bmatrix} 0.938 & \cdots & 0.938 \\ \vdots & \ddots & \vdots \\ 0.938 & \cdots & 0.938 \end{bmatrix}$$

To enhance computational efficiency and manage image dimensions (Figure 4.12(a)), the MTF size was decreased by calculating the average of pixels within each non-overlapping $m \times m$ section using the blurring kernel $\left\{\frac{1}{m^2}\right\}_{m \times m}$. This process involves combining the aggregated transition probabilities for every subsequence of length m :

Example: The 200×200 MTF matrix is reduced to 50×50 using the blurring kernel method to produce an aggregated MTF matrix. The difference between the MTF and the aggregated MTF is shown in Figure 4.11.

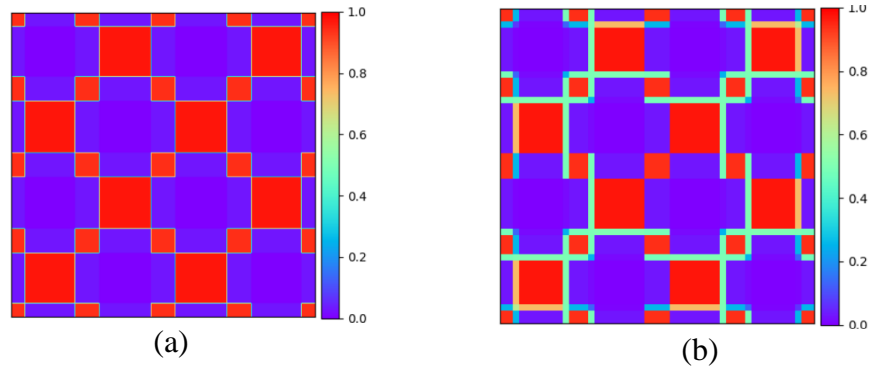


Figure 4.12: (a) MTF image (b) Aggregated MTF image

The MTF was applied to the ASHRAE dataset, as shown in Figure 4.12. Each MTF image represents one feature from the dataset under the normal operating conditions of the ASHRAE chiller. The four images represented in Figure 4.13 from left to right are TCO, TEI, TEO, and TCI (Refer Table 3.1).

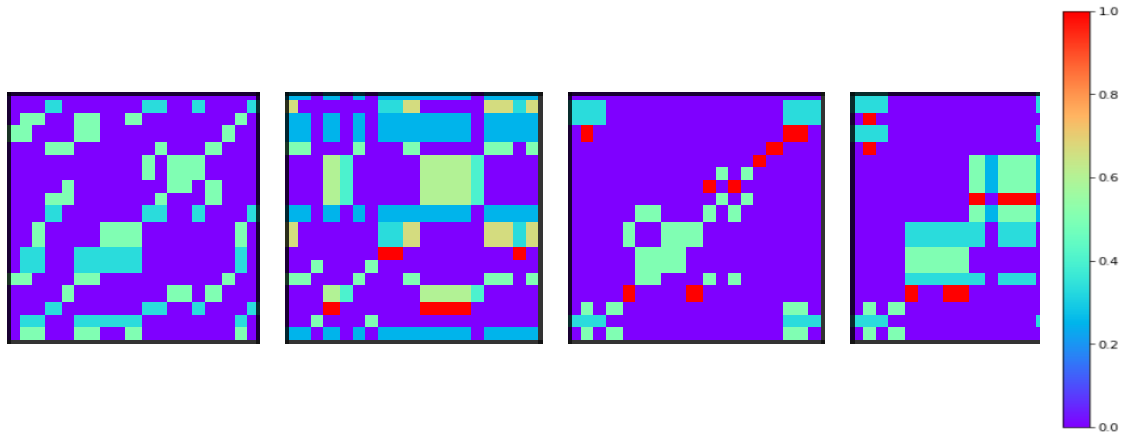


Figure 4.13 : MTF of 4 features from normal operation in ASHRAE chiller

Figure 4.13 illustrates the four features under normal operating conditions in the ASHRAE chiller. The MTF was implemented using three Q bins, and the M matrix had values ranging from 0 to 1. A color map was implemented in this matrix to obtain images, as shown in Figure 4.11.

4.2.2.2 Gramian Angular Summation Field

Similar to MTF, Gramian Angular field (GAF) encodes a time series as images. GAF is a representation of the time series in a polar coordinate system. Each element in the Gramian matrix is the cosine of the summation angle (Z. Wang & Oates, 2014).

Consider a sequence $X = x_n$ consisting of n observations with real values. X is scaled to ensure that all elements are confined within the range $[-1, 1]$.

$$\tilde{x}_i = \frac{x_i - \max(X) + (x_i - \min(X))}{\max(X) - \min(X)} \quad 4.22$$

The rescaled time series \tilde{X} is depicted in polar coordinates as shown in eqn 4.23 and 4.24.

The angle is the angular cosine of \tilde{X} and the radius is the time stamp.

$$\phi = \arccos(\tilde{x}_i), \quad -1 \leq \tilde{x}_i \leq 1, \tilde{x}_i \in \tilde{X} \quad 4.23$$

$$r = \frac{t_i}{N}, t_i \in N \quad 4.24$$

In eqn 4.24, t_i is the time stamp and N serves as a fixed value that normalizes the range of the polar coordinate system.

As time progressed, the corresponding values fluctuated among various angular points on the encompassing circles. For any given time series, the proposed mapping yielded a single outcome in a polar coordinate system with a unique inverse function. Polar coordinates can maintain absolute temporal relationships. After converting the rescaled time series into polar coordinates, the angular perspective was examined using the trigonometric sum between each point to detect the temporal correlations across different time intervals. GASF is defined as follows:

$$G = \begin{bmatrix} \cos(\phi_1 + \phi_2) & \cdots & \cos(\phi_1 + \phi_n) \\ \vdots & \ddots & \vdots \\ \cos(\phi_n + \phi_1) & \cdots & \cos(\phi_n + \phi_n) \end{bmatrix} \quad 4.25$$

$$= \tilde{X}' \cdot \tilde{X} - \sqrt{1 - \tilde{X}^2}' \cdot \sqrt{1 - \tilde{X}^2} \quad 4.26$$

\mathbf{I} represents a unit row vector $[1, 1, \dots, 1]$. After transformation to the polar coordinate system, each time step was considered as a 1-D space.

The inner product $\langle x, y \rangle = x \cdot y - \sqrt{1 - x^2} \cdot \sqrt{1 - y^2}$, G is a Gramian matrix:

$$\begin{bmatrix} \langle \tilde{x}_1, \tilde{x}_1 \rangle & \cdots & \langle \tilde{x}_1, \tilde{x}_n \rangle \\ \vdots & \ddots & \vdots \\ \langle \tilde{x}_n, \tilde{x}_1 \rangle & \cdots & \langle \tilde{x}_n, \tilde{x}_n \rangle \end{bmatrix} \quad 4.27$$

Example: A sine wave is considered an example of a time series, as illustrated in Figure 4.10. In total, 100 time points were used to construct the time series. The time series is scaled using Eqn. 4.22, as follows:

$$\tilde{x}_{100} = [0.5 \ 0.8 \ \cdots \ 0.19 \ 0.2]$$

Using eqn 4.23 and 4.24, ϕ and r are calculated for 100 time steps. Figure 4.13 represents both these values in the polar coordinate graph.

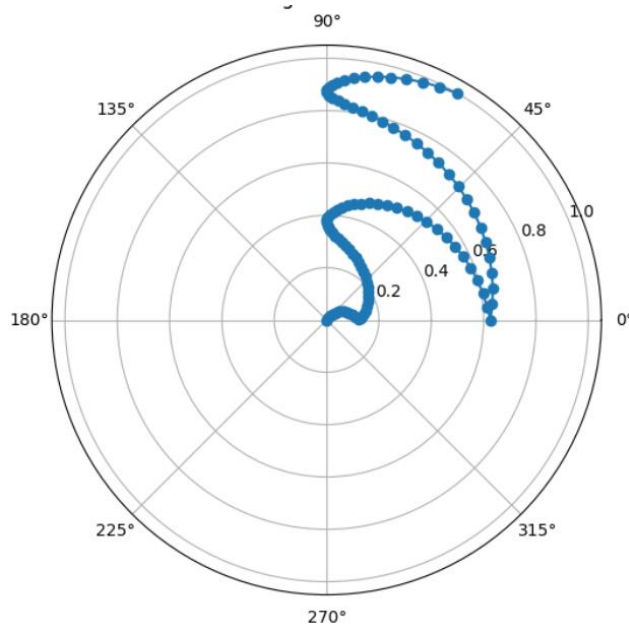


Figure 4.14: Polar coordinate graph for sine time series

The Gramian matrix for the sine time series is calculated using Eqn 4.26 as shown below. The resulting Gramian matrix is a 100×100 matrix, which is translated into an image, as shown in Figure 4.14.

$$\begin{bmatrix} -1 & \cdots & -1 \\ \vdots & \ddots & \vdots \\ -1 & \cdots & -1 \end{bmatrix}$$

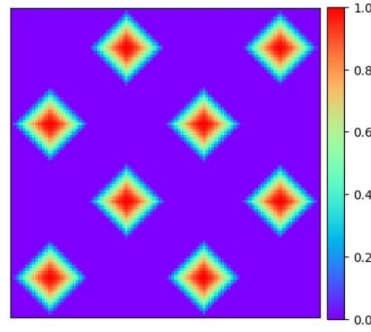


Figure 4.15 GASF image for sine wave

GASF offers multiple benefits. Primarily, it maintains temporal relationships as time progresses from the upper left corner to the lower right corner. Temporal correlations are embedded within the GASF, as $G_{(i,j)||i-j|=k}$ depicts the relative correlation through superimposed directions in relation to time interval k . The principal diagonal $G_{i,i}$ represents a unique case where $k = 0$, preserving the initial data. This diagonal enables the approximate reconstruction of the time series from high-level features extracted using a deep neural network.

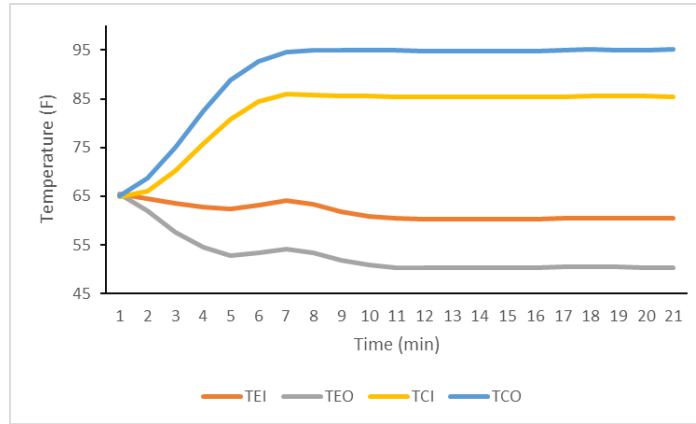


Figure 4.16 : Four features from ASHRAE dataset

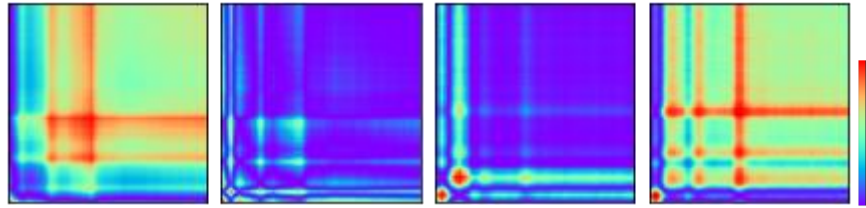


Figure 4.17 : GASF of 4 features from normal operation

The GASF methodology was implemented on the ASHRAE RP- 1043 dataset (Refer 3.3.1) in Python. Figure 4.16 illustrates the GAF images generated for the four features for normal operation. Each image was a feature of the ASHRAE dataset. The four features in Figure 4.17 from left to right are TCO, TEI, TEO, and TCI (see Table 3.1). Each time step of one feature in Figure 4.15 underwent a transformation from a polar coordinate to a Gramian matrix to the GASF image. Thus, the GASF image shows the dynamics of the feature for an entire cycle of operating conditions, which includes the transience caused by the change in the operating condition followed by a steady state, as shown in Figure 4.16 and 4.17.

4.2.3 Challenges in image data set generation

The samples were unique images representing the classes to be classified. In this study, 27 different operating condition cycles for different faults and normal operations were considered as unique conditions.

Table 4.2: Total number of samples available for the dataset

Experiment	No. of tests	No. of samples (*27)
Normal	4	108
Fault tests	20	540
Total	24	648

Table 4.2 represents the number of tests available in the ASHRAE RP-1043 dataset, and 27 operating conditions simulate the number of samples. The total number of available samples was 648, with 108 samples per class. The number of samples was insufficient to train, test, and validate the CNN model.

A major drawback of data-driven FDD models is that they require an immense amount of data. Because more experimental data were not available, the ASHRAE RP-1043 simulation model was proposed to generate additional data. A larger range of operating conditions and faults with more severity levels can be generated, thereby enriching the dataset.

4.2.3.1 Simulated Data Validation

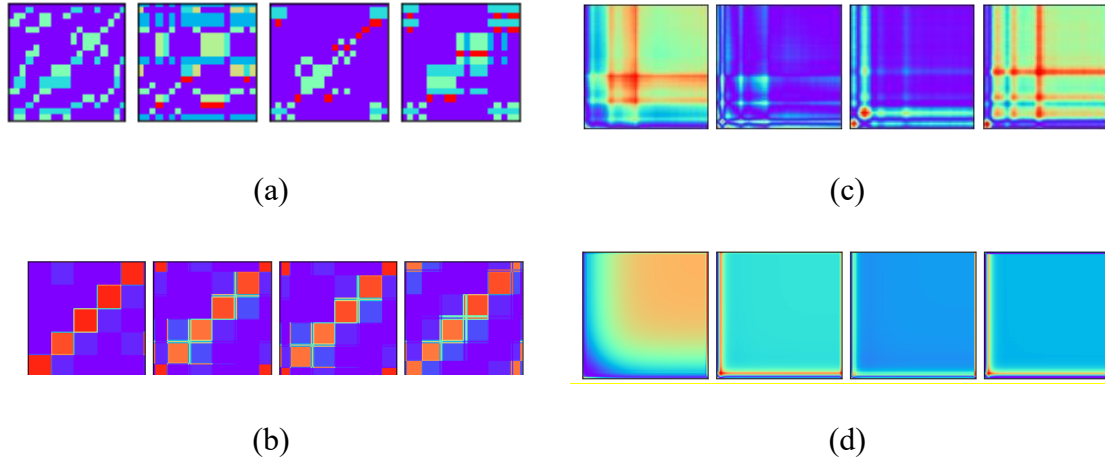


Figure 4.18: Comparison of simulated and experimental images (a) MTF image from experimental data (b) MTF image from simulation data (c) GASF image from experimental data (d) GASF image from simulation data

To use the simulated data to increase the data size, it was necessary to validate the simulated data with the experimental data. The same operating conditions were chosen as inputs for the simulation model. The model was run for 1000 seconds to capture the transient and steady states. As shown in the images in Figure 4.18, neither the GASF nor the MTF methods showed good validation of the experimental and simulation data.

The ASHRAE model is incapable of accurately simulating transient trends. It was noticed that the transient trend in the model was faster than the slower rate at which steady state occurred in the experiment. In the experiments, it took approximately 15 min to reach a steady state under operating conditions, whereas the steady state in the simulation model was achieved at approximately 40 seconds. This shorter transition was observed in both

the normal and fault scenarios. It is noted in the ASHRAE report that some thermal masses for the heat exchanger shell and compressor have not been accounted for. Hence, the GASF and MTF methodologies had to be abandoned because the data size could not be increased using the simulation data.

4.2.4 Deviation Strategy

In Section 4.2.1.2, it was concluded that the simulated data do not accurately capture the transient rate. The steady-state values of these features were compared with the experimental data. They were found to be in good agreement, with mean average error ranging from 0.05 to 3%. Therefore, a strategy is proposed that utilizes steady-state data from the simulation and creates images that are indicative of different faults.

A previous study noted that some measured parameters, such as temperature and pressure, and calculated parameters, such as the heat transfer rates of the evaporator, condenser, and COP, displayed a pattern of increase and decrease in their values when compared to the no-fault scenario (Breuker & Braun, 1998). By leveraging this observation, the following steps were implemented to calculate and generate deviation images.

1. Selection of parameters for the deviation matrix

The parameters considered for the deviation matrix are a collection of measured values, such as water temperature, refrigerant, pressure, and flow rate, which are critical indicators of a healthy or faulty condition. Because these are measured values that are usually available in the chiller, some measurements can be easily

retrofitted to the chiller system. The features selected for this application are explained in chapter 4.2.4.1.

2. Benchmark experiments

The ASHRAE RP- 1043 recommends benchmark tests that can be used to compare faulty data to normal data (Mathew C. Comstock, 1999). The steady-state values of these benchmark tests were used as the normal values.

3. Calculate deviation

Each cell in the deviation matrix was a parameter. The following formula was used to calculate the deviation of the fault parameters from the normal values:

$$Dev = \frac{Normal - Fault}{Normal} \quad 4.28$$

4.2.4.1 Feature selection

The ASHRAE dataset consists of 66 features containing the measured and calculated data, as listed in Table 3.1. The features are not only the chiller parameters, but also the secondary water circuits of the evaporator and condenser, which are specific to the experimental setup of ASHRAE RP-1043. As mentioned in Section 4.2.3, the limitations of the image-conversion method lead to the generation of additional data. The ASHRAE RP-1043 simulation model was used to supplement the experimental data set. Thus, the chosen features should be commonly measured and used for the simulation in the model. Random Forest (RF) and recursive feature elimination (RFE) were used for feature selection. RFE is a wrapper-type feature-selection algorithm. The wrapper style has a

different machine learning algorithm at the core wrapped by the RFE, which is used for feature selection. RFE operates by removing features that are deemed to be the least important until the desired number of features remains. Important features are determined by the importance score calculated by the core method, which are algorithms, such as decision trees or other statistical methods.

To determine the optimal number of important features in the ASHRAE RP-1043 dataset, RFE was applied using a random forest classifier (RF) as the core method. Cross-validation with Recursive Feature Elimination (RFE) was employed to evaluate various feature subsets and identify the optimal number of features based on the highest scoring combination. This method was applied to the ASHRAE RP-1043 experimental dataset, which contains eight classes with fault classes with four severity levels.

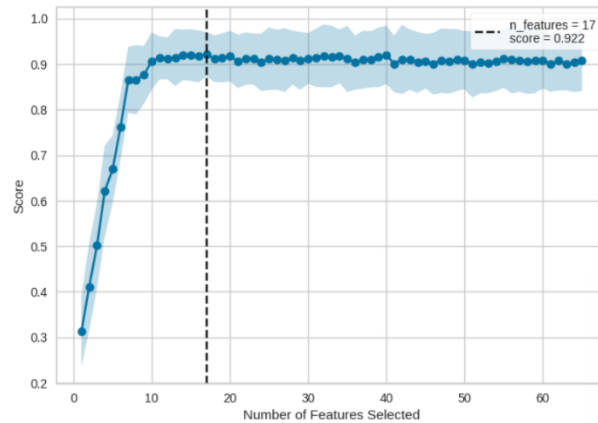


Figure 4.19: RFE for RandomForest classifier

Figure 4.19 illustrates the RFE visualizer plot with the number of features in the model with the cross-validated test score, variability, and optimum number of features. The test accuracy is shown in Figure 4.18. The first highest accuracy occurred with 17 features, the second highest score was at 20 features, and further features showed decreased scores.

Thus, this method recommends that 17-20 features best capture the dataset. 20 features were selected, as a rectangular shape is desirable when applying the 2D method.



Figure 4.20: Workflow for feature selection from the ASHRAE dataset

Once the number of features required is determined, the features that most effectively represent the data are identified using RF. The workflow of feature selection is shown in Figure 4.20. Random Forest, a machine learning algorithm, was employed for both classification and regression analyses. The model has a useful attribute “feature_importances_” which ranks the features. The model listed the 20 most important features listed in Table 4.3(a), and the test data were used to evaluate the models. The classification accuracy of RFE was 93.65%.

Table 4.3: List of features obtained from feature selection method (a) List of important features from RFE (b) list of usable features

Important feature (20)	System	Selected Features	Description
TWE_set	Chiller	TWE_set	Chilled water setpoint
TEO	Chiller	TEO	Temperature of Evaporator Water Out

TCO	Chiller	TCO	Temperature Condenser Water Out
TSI	Building	CondTons	Condenser Heat Rejection Rate
TBO	Building	EvapTons	Evaporator Cooling Rate
Cond Tons	Chiller	COP	Coefficient of Performance
Shared Cond Tons	Building	kW/Ton	Compressor Efficiency
CondEnergyBalance	Building	FWC	Flow Rate of Condenser Water
Evap Tons	Chiller	FWE	Flow Rate of Evaporator Water
Shared Evap Tons	Building	TEA	Evaporator Approach Temperature
EvapEnergyBalance	Building	TCA	Condenser Approach Temperature
COP	Chiller	PRE	Pressure of Refrigerant Evaporator
kW/Ton	Chiller	PRC	Pressure of Refrigerant Condenser
FWC	Chiller	P_lift	Pressure Lift Across Compressor
FWE	Chiller	Tsh_suc	Refrigerant Suction Superheat Temperature
TEA	Chiller	TRC_sub	Subcooling from Condenser
TCA	Chiller	T_eva	Refrigerant Temperature Evaporator
PRC	Chiller	T_cond	Refrigerant Temperature Condenser
Tsh_suc	Chiller	TEI	Temperature of Evaporator Water In
TRC_sub	Chiller	TCI	Temperature of Condenser Water In

(a)

(b)

Table 4.3 (a). lists the first 20 important features based on the RFE selector. This list of features includes chiller- and building-associated parameters. The building-related parameters are the measurements and calculated values of the secondary evaporator and

condenser loops. This system is specific to the experimental setup. Only the chiller parameters, which can also be obtained from the chiller model, are considered. Table 4.3 (b) shows the final list of the 20 features used in the deviation method. These features corroborate those reported in other studies (Nie et al., 2023; Xue et al., 2018).

4.2.4.2 Demonstration of Deviation matrix method

To demonstrate the deviation matrix method, a fault with a reduced condenser water-flow rate was considered. One operating condition was chosen, which consisted of 20 features (Table 4.3(b)). A 1D array of sizes [1,20] was obtained from the reduced condenser water-flow-rate dataset. Similarly, data were extracted from normal tests with the same operating conditions and 20 features. The deviation is calculated using Eqn 4.28 and is provided below:

Normal =

[10.00	10.422	32.824	230.059	195.69	3.398	1.033	16.848	13.63	362.9
876.227	514.430	3.274	3.444	3.589	3.122	6.133	34.578	9.256	30.989]

Fault =

[10.000	10.422	33.872	185.608	147.771	2.786	1.260	10.159	13.566	368.277
901.045	531.941	4.383	2.605	5.000	3.266	6.511	35.577	9.777	30.577]

Deviation =

[0.000	0.061	0.002	0.193	0.245	0.078	-0.219	0.397	0.005	-0.015
-0.029	-0.034	-0.339	0.244	-0.393	-0.046	-0.061	-0.028	-0.056	0.013]

These calculated deviation values were used in the 1D array form as inputs for the models described in chapter 4.1. The deviation matrix was reshaped to a 2D array of sizes [4,5] for

the 2D CNN model described in chapter 4.2.1. Each cell of the matrix represents a feature from Table 4.3 (b) as shown in Figure 4.21.

TWE_set	TEO	TCO	Cond Tons
EvapTons	COP	kW/Ton	FWC
FWE	TEA	TCA	PRE
PRC	P_lift	Tsh_suc	TRC_sub
T_eva	T_cond	TEI	TCI

Figure 4.21: Features in deviation matrix

The resulting 2D deviation matrix in numerical form is represented below:

Deviation matrix =

0.000	0.061	0.002	0.193,
0.245	0.078	-0.219	0.397,
0.005	-0.015	-0.029	-0.034,
-0.339	0.244	-0.393	-0.046,
-0.061	-0.028	-0.056	0.013]

Each cell of the matrix represents a feature from Table 4.3 (b).

4.2.4.3 Comparison of experimental and simulated data

The following images (Figure 4.15 (a)–(d)) were generated from the deviation matrix to illustrate the patterns among the different classes. This also helps in quick judgement when comparing simulation and experimental data.

The deviation matrix was normalized, and color coded using a color legend between 1 and -1. Hence, the image will be able to capture the increasing and decreasing trends of the parameter in different faults, thus providing a unique pattern for each fault.

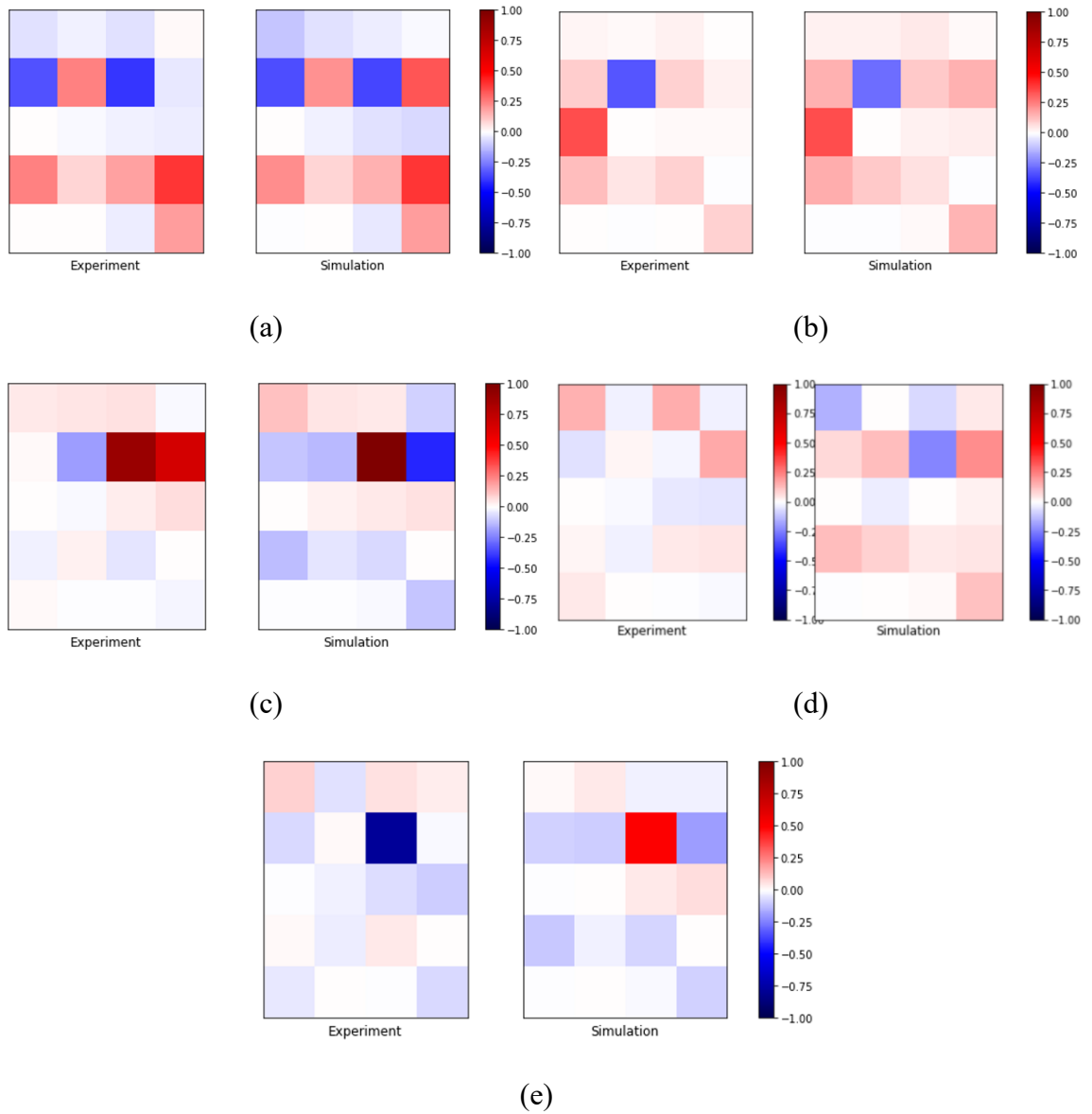


Figure 4.22: Images generated using deviation strategy for faults (a)Reduced Condenser Flow (b) Reduced Evaporator Flow (c)Refrigerant Leakage (d)Refrigerant Overcharge (e)Condenser Fouling

Figure 4.22 shows the images created from the experimental and simulation data for the five fault types. Simulations were performed under the same operating conditions as those used in the experiment. The majority of the parameters were in good agreement. Faults, such as refrigerant overcharge and condenser fouling, display a number of dissimilarities between the features of the experiment and simulation. This could affect further studies based on simulated data. Hence, more images can be created using the simulation model to enhance the dataset for CNN models.

4.3 Pipeline

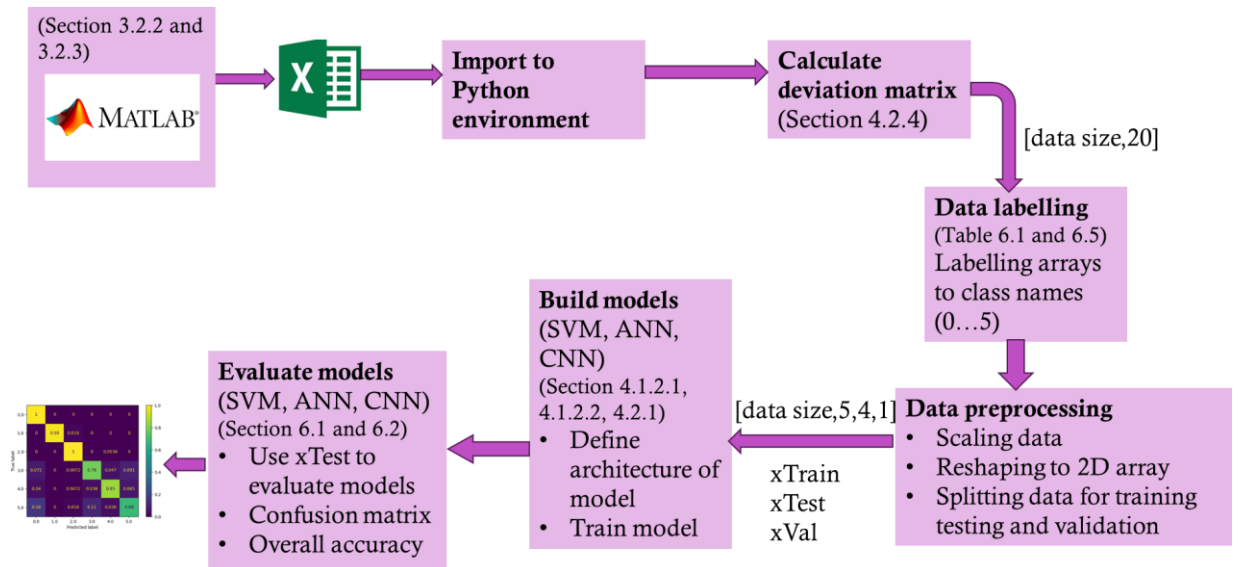


Figure 4.23: Workflow to implement deviation matrix method

Figure 4.23 illustrates the workflow implemented to build the FDD models. MATLAB was used to generate data by implementing the ASHRAE model and small chiller model. It was also used to extract steady-state values from the experimental test cycles. The datasets were stored in Microsoft Excel workbooks. The data were then imported into Python to calculate

the deviation matrix specified in chapter 4.2.4. The deviation matrix was then converted into NumPy (Harris et al., 2020), labeled, and saved. This labeled dataset was then scaled using the Python package and reshaped for the 2D array for the CNN and 1D array for the ANN and SVM. The data were then split into training and test datasets using Keras³ software package. The model architectures described in Chapter 4.1 and 4.2.1 was defined using TensorFlow and trained using a training dataset. The model was evaluated using the model accuracy function of the Keras software package. Finally, the FDD performance was evaluated using a confusion matrix.

4.4 Summary

This chapter discusses the methods used in hybrid networks, the architecture, and the parameters used to build the hybrid network. Machine learning and deep learning were used for the feature selection and classifier modules of the hybrid network. The use of a 2D CNN as an FDD and the architecture to be used for the FDD are described. Some 2D input creation methods such as MTF and GASF have been explored. The challenges faced in implementing these methods for CNN have been recognized. One of the challenges is the availability of experimental data to satisfy the requirements of 2D CNN. Hence, simulating more data would help address the data shortage and variability within the dataset. The simulated data were assessed using MTF and GASF. However, these methods cannot validate simulation data. It is inferred that the ASHRAE model cannot closely replicate the transience of the test cycle. Therefore, steady-state data were used to develop

³ Keras functions as an open-source software library. It offers a Python-based interface for constructing models of artificial neural networks..

the deviation matrix method, which utilizes only steady-state values to construct a 5×4 matrix comprising 20 features. These 20 features were chosen using feature selection methods such as RFE. A 2D matrix is visualized to validate experimental and simulation results.

5. Small chiller model

In this study, a small chiller model was developed. A small chiller was used for cooling the modular data center. A Data center is a physical facility that houses IT infrastructure such as servers, data storage drives, and hardware equipment. All of this equipment requires continuous cooling for optimum operation. They were placed in enclosed boxes known as cabinets to maximize the cooling effect supplied to the equipment. Hence, the cooling system of the data center consisted of a heat exchanger placed inside the data center cabinet, and a scroll-type vapor compression chiller was modelled. The model was developed and validated against experiments. Several faults in the system were identified and replicated in the system model.

In Data centers, the chiller is a key component used in modular cooling systems for data-server racks, also known as IT racks. Physics-based chiller models can be categorized by a modeling approach using heat exchangers, including the (1) lumped parameter approach, (2) moving boundary approach, and (3) finite control volume approach. Browne and Bansal used the lumped parameter approach to model a packaged chiller operating under different operating conditions (Browne & Bansal, 2002). The same setup was modeled using the NTU-e methodology for heat exchangers to improve the physical realism and accuracy of the model (Browne & Bansal, 2001). A 90-ton centrifugal water chiller was modeled was modelled using a finite control method to demonstrate the start-up and transient load changes in the chiller (S. Bendapudi, 2002). Researchers have compared the finite volume and moving boundary methods for heat exchangers. Their findings revealed that the moving boundary method offers similar accuracy while being computationally more

efficient. (Hermes & Melo, 2008). A natural convection bypass two-circuit cycle was modeled using multiple zones for the heat exchangers (Ding et al., 2004). A control-oriented approach for a water chiller refrigeration system was developed using a lumped parameter approach to study the effects of control inputs, such as the compressor operational frequency, and their effect on the performance of the chiller (Lei & Zaheeruddin, 2005).

Based on a literature review, a model for a small modular cooling system for IT racks has not been reported in previous studies. This paper proposes a physics-based mathematical model for the cooling system of IT racks that accurately simulates normal and faulty conditions. A series of common faults were identified and simulated using this model. Validation using real experimental data demonstrated the performance of this model. Furthermore, the chiller response from different types of faults is presented, providing data-driven insights into the behavior of small chillers. This model can be used to predict faulty system behaviors and develop predictive maintenance strategies for these systems. Additionally, simulated data pertaining to varying operating conditions and fault levels can be used to train and validate Artificial Neural Networks (ANN) or Deep Neural Networks (DNN) for online fault diagnosis (Santosh et al., 2007; X. Tian et al., 2018).

The remainder of this chapter is organized as follows. Section 5.2 introduces the modular cooling system, and Section 5.3 presents common faults. Sections 5.4 and 5.5 detail the mathematical model of the cooling system and the fault conditions, respectively. Section 5.6 elaborates on the experiments and analyzes the results. Finally, Section 5.7 concludes the study.

5.1 Modular Cooling System Overview

This section provides a brief overview of the modular cooling systems. A mathematical model is developed for this system, which consists of a modular data center that is used to change the loads on the chiller and packaged chiller. This section consists of two parts: describing the system setup and the overall approach for the mathematical model development of the system.

5.1.1 Cooling System set-up

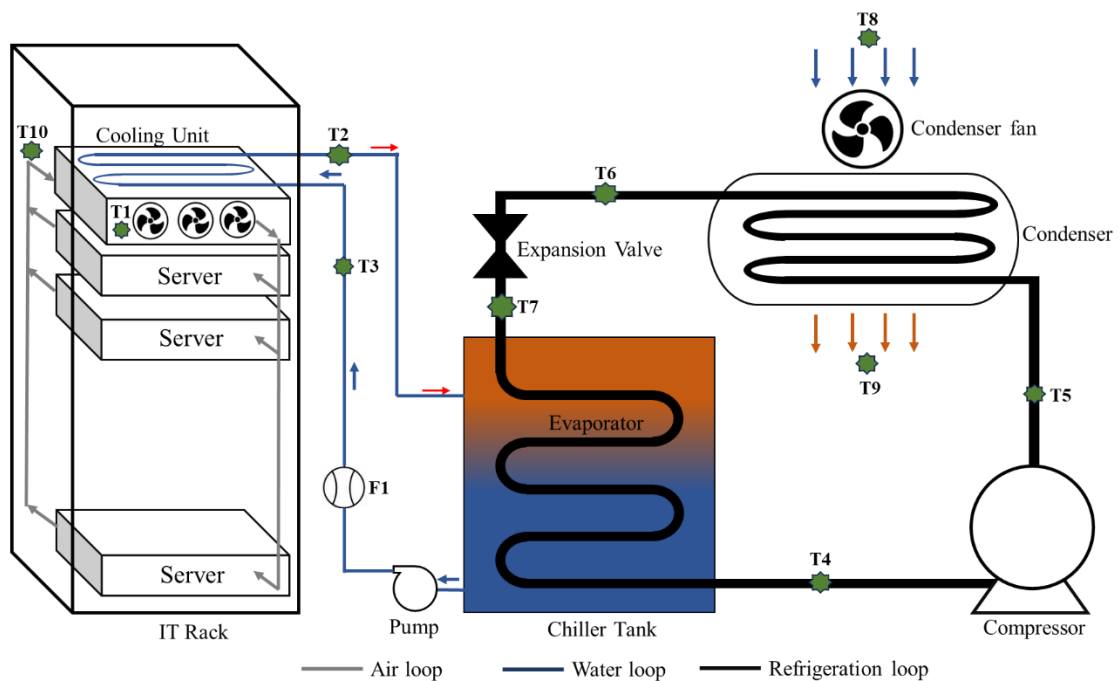


Figure 5.1: Schematic of experimental set-up

Figure 5.1 shows the schematic of the experimental setup used in this study. The IT rack had 32 servers and a cooling unit within the IT cabinet. The IT rack applies a thermal load to the chiller. The temperatures were measured at ten locations across different components

within the system. A flowmeter is installed in the water loop to measure the flow rate of water in the water loop. Four temperature sensors were placed inside the IT cabinet, two of which were placed on the side where the hot air from the servers entered the cooling unit, and the other was placed at the exit face of the cooling unit. The other two sensors are present within the water pipes entering and exiting the cooling unit, measuring the chilled water supplied to the unit and the hot water temperature exiting the unit. Four temperature sensors were installed in the chiller. The temperature sensors were wedged between the refrigerant pipe and the insulation covering the pipeline. The temperature was measured at the exit of each component. The positions of the sensors are shown in Figure 5.1. The remaining two temperature sensors were placed near the face from which air entered the condenser heat exchangers, and the other sensor was located near the condenser exit face. Handheld power meters were used to measure the power supplied to each server and the cooling unit.

Table. 5.1: Components of the experimental set-up

Loop	Component No.	Component Name
Air loop	1	Fan in cooling unit
	2	Heat exchanger in cooling unit
Water loop	3	Water pipes
	4	Pump
Refrigerant loop	5	Evaporator
	6	Compressor

	7	Condenser
	8	Condenser fan
	9	Expansion valve

Table 5.2 lists the specifications of the instruments used in these experiments.

Table 5.2: Instrumentation details

Instrument type	Tag no. & Location	Range	Accuracy
Temperature DS-18S20 Digital Thermometer	T1, cold air (entry at cooling unit)	-55°C to	±0.5°C
	T2, hot water (exit from cooling unit)	125°C	
	T3, cold water (entry to cooling unit)		
	T4, exit from evaporator		
	T5, exit from compressor		
	T6, exit from condenser		
	T7, exit from expansion valve		
	T8, ambient air entry to condenser		
	T9, air exit from condenser		
	T10, hot air (exit from cooling unit)		

Flow	F1, exit from pump	10-120	$\pm 1\%$
Rotary Vane type		L/min	

5.1.2 Modeling Approach

This study proposes a temporal response model that is specific to IT rack systems with small modular cooling unit IT rack, as described in section 5.1.1. Such systems have three main operating loops that interact with each other: refrigeration, water, and air. Energy transfer occurs from one loop to another via an interface heat exchanger, as shown in Figure 5.2. The hot air emitted by the servers enters a cooling unit (air-water heat exchanger) inside the rack, which cools the hot air. The energy from the hot air is transferred to the water loop via a cooling unit containing water. As the water was heated, it was directed to a chiller tank containing an evaporator. An evaporator was used to transfer energy from hot water into the refrigerant loop.

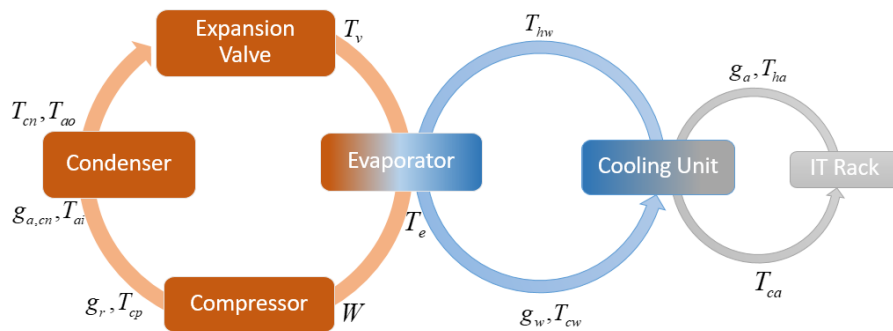


Figure 5.2: Schematic of the vapor compression chiller system

The refrigerant loop has four main components: evaporator, compressor, condenser, and expansion valve. The refrigerant enters the evaporator in the liquid phase, increases its enthalpy as it travels through the evaporator, exits as superheated vapor, and then enters the compressor. The compressor compresses the superheated vapor at high temperature and pressure. Pressurized vapor enters the condenser, which is a fin-tube-type heat exchanger. The condenser expels the energy absorbed by the evaporator and the work performed by the compressor on the refrigerant into the ambient environment. The refrigerant exited the condenser as a subcooled liquid. It proceeds to the expansion valve, where the refrigerant expands, thus further lowering the pressure and temperature before entering the evaporator. The thermodynamic states of the components are shown in Figure 5.3.

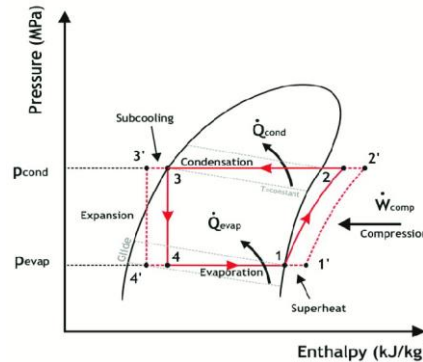


Figure 5.3: Pressure-Enthalpy diagram of refrigeration cycle (Duarte et al., 2017)

The chiller chosen for modeling had a scroll compressor with a fixed mass flow rate, a fin and tube condenser, an evaporator that is a helical tube immersed in a chiller tank, a thermostatic expansion valve, and a heat exchanger present in the IT rack. The working fluid in the chiller was the refrigerant R22 with a copper tube. The chiller was modelled with a set point of 10 °C, and the ambient air temperature of the condenser was 30 °C. An

outside temperature of 30 °C was obtained from the temperature measurement of ambient air in the experiment.

5.2. System Faults

Fault conditions can occur in many components of Heating Ventilation and Air Conditioning (HVAC), including chillers, heat pumps, boilers, and packaged rooftop units. Zhang et al. (2017) categorized a series of HVAC operational faults, among which three types were related to chillers: fouling fault, sensor offset, and performance degradation.

The system model was configured to capture the interaction of three loops: air, water, and refrigeration, as shown in Figure 5.2. In particular, the model and simulation presented in this study aimed to identify the following faults.

- i. Fault#1 - Fan malfunction in cooling unit
- ii. Fault#2 - Fouling in heat exchanger of cooling unit
- iii. Fault#3 - Restriction in water loop
- iv. Fault#4 - Fouling in heat exchanger of evaporator
- v. Fault#5 - Fan malfunction in condenser
- vi. Fault#6 - Fouling in heat exchanger of condenser

5.3. Mathematical Modeling

Each chiller was modeled using a transient lumped heat capacity method. An explicit method was employed to solve each numerical model using the values from the preceding time step. Each module calculates the exit temperature, which is subsequently used as the input for the next time step in the downstream module. The system determines the

temperature of the chilled water and the cold air temperature in the air loop. Each model calculates the enthalpy based on the energy balance and temperature, which are estimated using CoolProp (Bell et al., 2014), a software to estimate refrigerant properties under different thermodynamic conditions. The enthalpy and pressure of the state are provided in the software to obtain the fluid temperature.

The following assumptions in modeling the system:

- (i) The physical properties of the refrigerant were uniform in the transverse section of the heat exchanger.
- (ii) Heat conduction in the axial direction was ignored.
- (iii) The momentum equation is not considered in this physics-based model. This was because the chiller under consideration had a low capacity, and the flow resistance and flow inertia (L/A) in the refrigeration section were negligible (Grald & MacArthur, 1992; Kadam et al., 2020; MacArthur & Grald, 1989).

5.3.1 IT Rack Cooling Unit

The cooling unit was modeled using the logarithmic mean temperature difference (LMTD) method. Because the heat exchanger is part of the air loop, with both air and water flowing through it, the energy balances for these two media were computed independently.

- Air side energy balance:

$$\frac{dh_{ca}}{dt} = \frac{g_{a,cu}}{m_{a,cu}} (h_{ha} - h_{ca}^{t-1}) - \frac{U_{cu}}{m_{a,cu}} A_{cu} LMTD_{cu}^{t-1} \quad 5.1$$

- Water side energy balance:

$$\frac{dh_{hw}}{dt} = \frac{g_{w,cu}}{m_{w,cu}} (h_{cw}^{t-1} - h_{hw}^{t-1}) - \frac{U_{cu}}{m_{w,cu}} A_{cu} LMTD_{cu}^{t-1} \quad 5.2$$

5.3.2 Compressor

A scroll-type compressor was considered in this simulation. The work done by the compressor on the refrigerant is polytrophic. The compressor drives the mass flow rate of the refrigerant in the refrigerant loop. The following parameters were calculated for the compressor module.

Mass flow rate of the refrigerant:

$$g_r = \eta_v \rho_{suc} vol_s N \quad 5.3$$

Work performed on refrigerant:

$$W = \frac{n P_{suc}}{(n-1) \rho_{suc}} \left(\left(\frac{P_{dis}}{P_{suc}} \right)^{1-n^{-1}} - 1 \right) \quad 5.4$$

Exit enthalpy from compressor:

$$\frac{dh_{cp}}{dt} = g_r (h_e^{t-1} - h_{cp}^{t-1}) + g_r W \quad 5.5$$

5.3.3 Condenser

The condenser was a fin-tube-type heat exchanger. Air was forced to pass through the heat exchanger using fans near the heat exchanger. The condenser module solves the energy balance on the refrigerant-side.

- Refrigerant-side energy balance:

$$\frac{dh_{cn}}{dt} = \frac{g_r}{m_{r,cn}} (h_{cp}^{t-1} - h_{cn}^{t-1}) - \frac{U_{cn}}{m_{r,cn}} A_{cn} LMTD_{cn}^{t-1} \quad 5.6$$

$$T_{cn} = f(h_{cn}, P_{cn})$$

- Air-side energy balance:

$$\frac{dh_{a,cn}}{dt} = \frac{g_r}{m_{a,cn}} (h_{a,i}^{t-1} - h_{a,o}^{t-1}) + \frac{U_{cn}}{m_{a,cn}} A_{cn} LMTD_{cn}^{t-1} \quad 5.7$$

5.3.4 Expansion Valve

The refrigerant expands adiabatically in the thermal expansion valve. Hence, the valve outlet enthalpy was the same as the inlet enthalpy. The refrigerant exits the expansion valve at lower temperature and pressure.

$$h_v = h_{cn}^{t-1} \quad 5.8$$

$$T_v = f(h_v, P_v)$$

5.3.5 Evaporator

The evaporator was a shell-and-tube-type heat exchanger. The coiled tube contains a flowing refrigerant that is submerged in a tank of water (chiller tank), where water flows continuously. Similar to all the heat exchangers modeled in this system, the LMTD method was applied. The energy balances for the refrigerant and water sides were solved simultaneously. The exit temperature of the evaporator was obtained as a function of evaporator pressure and exit enthalpy.

- Water side energy balance:

$$\frac{dh_{cw}}{dt} = \frac{g_w}{m_{w,e}} (h_{hw}^{t-1} - h_{cw}^{t-1}) - \frac{U_e}{m_{w,e}} A_e LMTD_e^{t-1} \quad 5.9$$

- Refrigerant side energy balance:

$$\frac{dh_e}{dt} = \frac{g_r}{m_{r,e}} (h_v^{t-1} - h_e^{t-1}) + \frac{U_e}{m_{r,e}} A_e LMTD_e^{t-1} \quad 5.10$$

$$T_e = f(P_e, h_e)$$

The pressure drop correlation was used to calculate the pressure drop within the heat exchangers to estimate the steady-state pressure conditions at the outlet of the evaporator and condenser. The correlations used to calculate the pressure drop across the refrigerant tube are given in Appendix -1.

5.3.6 Overall Heat Transfer Coefficient

Correlations were used to estimate the overall heat-transfer coefficients of the heat exchangers in the refrigerant loop. The estimations were used for steady-state and transient conditions. The heat-transfer coefficient was calculated in a manner similar to that of the pressure-drop calculation. The heat exchanger was divided into several control volumes, and the heat transfer coefficient at each control volume was calculated. The heat-transfer coefficient along the length of the heat exchanger was obtained for each control volume. The correlations used to calculate the overall heat-transfer coefficients for the evaporator and condenser are provided in Appendix 1.

5.3.7 Wall-Heat Transfer Model

This model estimates the heat loss from tubing sections between components. A certain amount of heat transfer occurs from the ambient to the refrigerant tube because of the large difference in temperature between the refrigerant and the ambient environment. Sensors were placed on the tube wall to indirectly obtain the refrigerant temperature. As the thermal conductivity of copper (material of construction of tubing section) is very high, it is assumed that the refrigerant temperature is very close to the thin copper tube surface temperature. The sensors are located midway between the two components of the refrigerant loop. Thermal sensors were placed between the refrigerant tube and the insulation covering it. To capture the heat transfer and obtain a temperature closer to that measured, a thermal resistance network was considered, as illustrated in Figure 5.3.

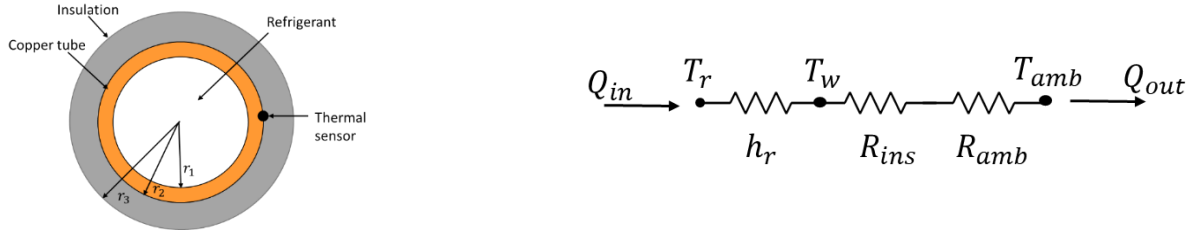


Figure 5.4: Thermal resistance network for tube with insulation

A lumped heat resistance-capacitance model was formulated owing to the high thermal conductivity of the copper tube, ensuring negligible spatial temperature gradients in the axial direction. The governing equations were solved to determine the tube-wall temperature.

$$\frac{dT_{wall}}{dt} = \frac{1}{m_{tube}} (Q_{in} - Q_{out}) \quad 5.11$$

$$Q_{in} = \alpha_r (2\pi r_1 L) (T_r^t - T_{wall}^{t-1}) \quad 5.12$$

$$Q_{out} = \frac{1}{R_{ins} + R_{amb}} (2\pi r_3 L) (T_{wall}^t - T_{amb}) \quad 5.13$$

$$R_{amb} = \frac{1}{\alpha_a} \quad 5.14$$

$$R_{amb} = \frac{r_3 \ln\left(\frac{r_3}{r_2}\right)}{k_{ins}} \quad 5.15$$

5.3.8 System Model

The chiller system component models are described in the previous section. The flow chart in Figure 5.5 provides an overview of the integration of component models and the computational method used to simulate the system. The geometrical and system operation

parameters, that is, the system-specific operating pressure and mass flow rate of the water and air loop, were used as inputs to the model. The temperatures across all the components were initialized for the model. In the next step, the mass flow rate for the refrigeration loop was calculated based on the system parameters. The mass flow rate was used to estimate the heat transfer coefficients of the heat exchangers in the refrigerant loop. The pressure drop across the heat exchangers was estimated at the same time step. These values remained constant throughout the run and were updated only when the mass flow rate reached zero. The values of the heat transfer coefficient and pressure drop estimated in the previous steps were used to determine the temperature at the exit of each component using energy balance. An ON/OFF controller logic was applied at the end of the time loop, as shown in Figure 5. 5. This constitutes the chiller model methodology.

Table. 5.3: Furnishes all model parameters

Table5.3: Model parameters

Sr. No	Parameter	Description
1.	P_{dis}	Pressure at discharge of compressor
2.	P_{suc}	Pressure at suction of compressor
3.	T_{ha}	Temperature of hot air at inlet of cooling unit
4.	g_w	Mass flow rate of water in water loop
5.	g_a	Mass flow rate of air through cooling unit on air loop
6.	$g_{a,cn}$	Mass flow rate of air through condenser

7.	g_r	Mass flow rate of refrigerant in refrigerant loop
8.	U_e	Overall heat transfer coefficient in evaporator
9.	U_{cn}	Overall heat transfer coefficient in condenser
10.	ΔP	Pressure difference between discharge and suction pressures
11.	T_{sp}	Set point temperature of the chiller
12.	t	Time

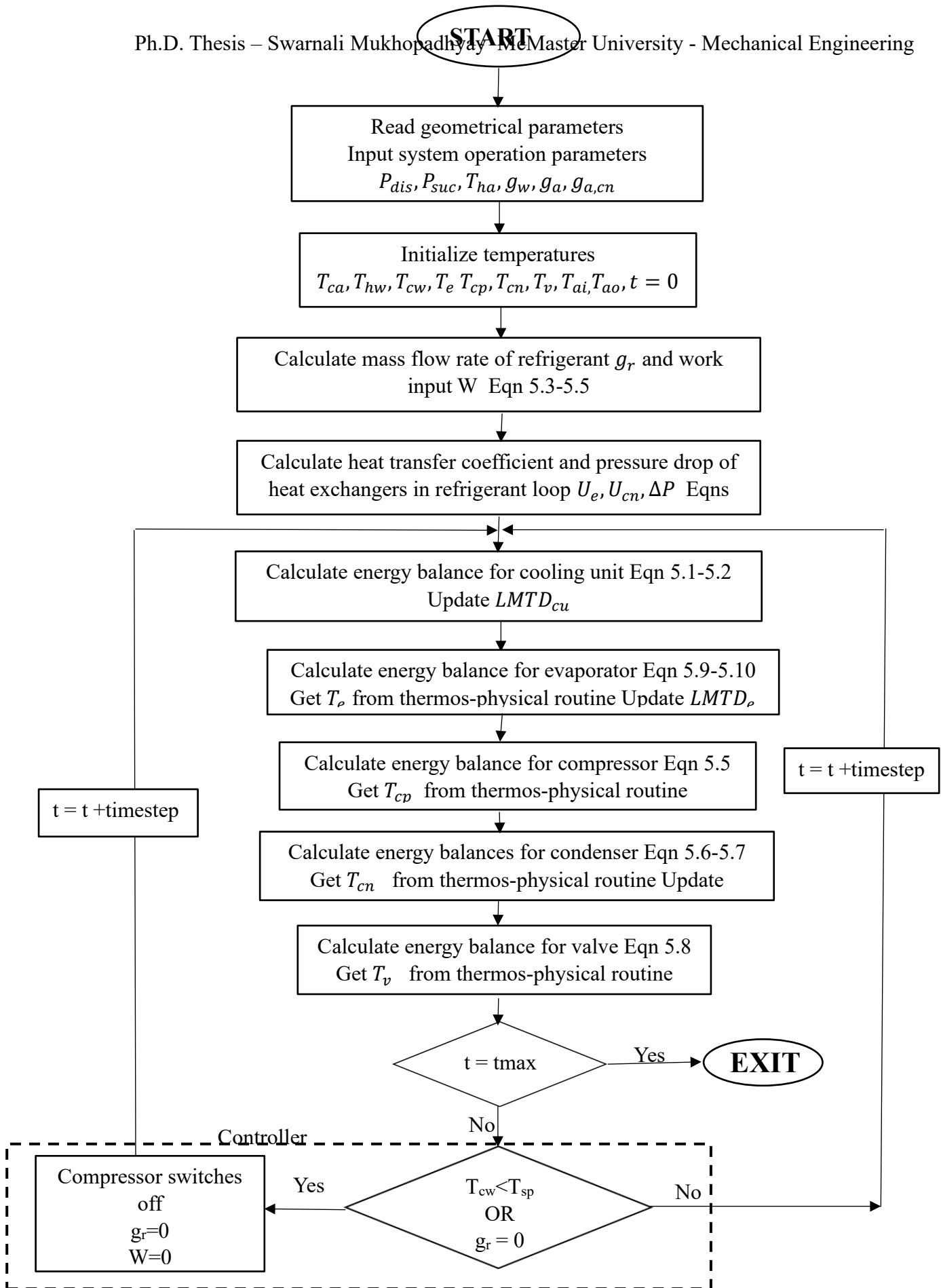


Figure 5. 5: Flowchart of model

5.4. Fault Models

Faults can be modeled in three ways: white-box (physics)-based, black-box (empirical)-based, and grey box (semi-empirical) models. In this study, a physics-based approach was selected to represent the faults listed in Section 5.2 for the modular cooling system of an IT rack.

Fault#1 (Component No. 1): The air loop consists of a cooling unit, which is a water-to-air heat exchanger. This fault is restricted to the flow of air that could occur owing to fan malfunction or wear, which is represented as a decrease in $g_{a,cu}$ by a factor of $(1-FL)$, where FL is the fault level, which may vary from 10% to 90%.

$$g_{a,cu,fault} = (1 - FL)g_{a,cu} \quad 5.17$$

Fault#2 (Component No. 2): Fouling is a common fault that occurs over time in heat exchangers. Fouling affects the degradation of the overall heat transfer coefficient of the heat exchanger. This phenomenon is represented by Eqn. (5.18). FL may vary from 10-90%.

$$U_{cu,fault} = (1 - FL) U_{cu} \quad 5.18$$

Fault#3 (Component Nos. 3 and 4): The water loop carries the chilled water to the cooling unit and returns hot water into the chiller tank. Valves and pumps are present in the loop.

The malfunction of either the valve or pump affects the flow rate of the water, as shown in Eqn. (5.19). FL may vary from 10-90%.

$$g_{w,fault} = (1 - FL)g_w \quad 5.19$$

Fault#4 (Component No. 5): The heat exchanger used in the chiller system was an immersed coil heat exchanger. The metal was continuously exposed to water on its outer side and liquid refrigerant on its inner side, which increased the chance of fouling by corrosion on the surfaces of the coil evaporator, particularly on the outer side. This causes degradation of the overall heat transfer coefficient, as shown in Eqn. (5.20). FL may vary from 10-90%.

$$U_{e,fault} = (1 - FL)U_e \quad 5.20$$

Faults #5 and #6 (Components No. 7 and 8): Similar to the case of the restriction in the air loop, this fault affects the refrigerant loop. Condensers are susceptible to environmental factors because they are mostly kept outside. Condenser fan wear and dirt deposition on the condenser are common faults that occur in these heat exchangers. FL may vary from 10-90%. This wear, which leads to lower fan flow and condenser fouling, is mathematically presented below. Eqn (5.21) represents fault#5, and Eqn (5.22) represents fault#6.

$$g_{a,cn,fault} = (1 - FL)g_{a,cn} \quad 5.21$$

$$U_{cn,fault} = (1 - FL)U_{cn} \quad 5.22$$

5.5. Analysis

This section consists of two parts: (a) experiments conducted to validate the model, and (b) fault evaluation using the chiller model.

5.5.1 Experimentation and model validation

A set of experiments were conducted on a packaged chiller to validate the developed mathematical model. These experiments were designed to capture different operating conditions of the chiller. Table 5.4 represents the constants used in modeling the chiller. These values are specific to the chiller system. They were obtained from the spec sheet and measurements of the system.

Table 5.4 : Constants of the chiller system

Parameters	Constants
Mass flow rate of refrigerant	0.016 kg/s
Mass of water in chiller tank	30 kg
Mass of refrigerant in evaporator	0.6 kg
Mass of refrigerant in condenser	0.7 kg
Pressure in evaporator	0.32 MPa
Pressure in compressor	0.91 MPa
Heat transfer area in evaporator	0.62 m ²

Heat transfer area in condenser	1.194 m ²
---------------------------------	----------------------

Two experiments were conducted at different thermal loads, including 2.3 kW and 3 kW. Each experiment was repeated three times. Varying the load was achieved by changing the number of active servers (switched on). Thus, nine experiments were conducted in total. The chiller was set at a temperature of 11 °C, and the IT rack was simultaneously switched on. The system ran for an hour to achieve steady-state operation.

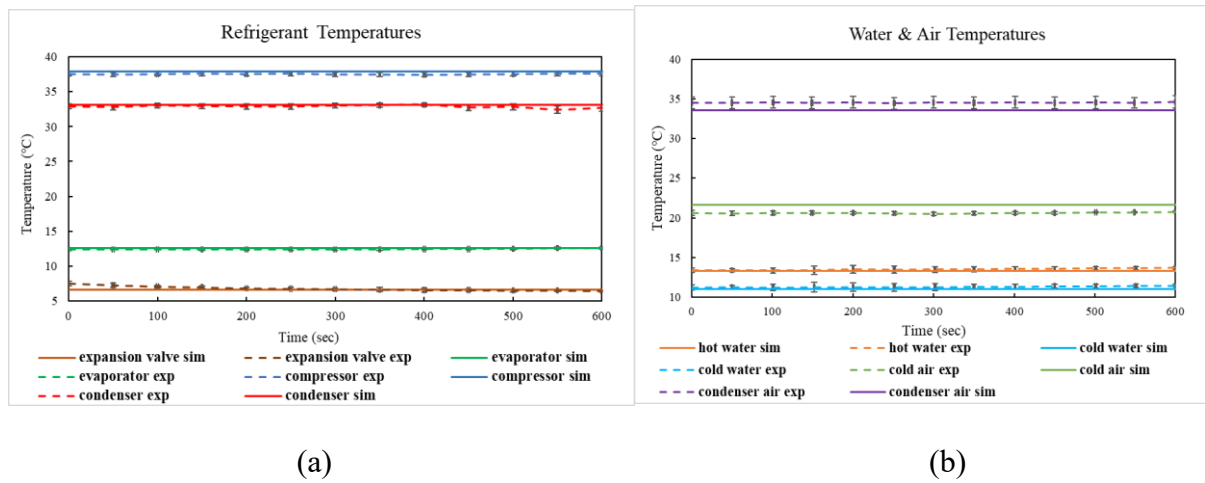


Figure 5.6: (a) Temperature profile of refrigerant under 3 kW thermal loading (b) Temperature profile of water and air loop under 3 kW thermal loading

The response of the experiment conducted at a thermal load of 3 kW is shown in Figure 5.6. It is evident from the response that the chiller operated continuously under steady-state conditions, without a compressor trip.

Figure 5.6 shows that there is good agreement between the simulated temperatures and the experimental data. The Mean Relative Error (MRE) was calculated using Eqn. 5.23. The

estimated MRE between the simulated temperature and experimental data was found to be in the range of 3-15 %.

$$MRE = \frac{1}{n} \sum \frac{|\Delta y_{sim} - \Delta y_{exp}|}{|\Delta y_{exp}|} \times 100\% \quad 5.23$$

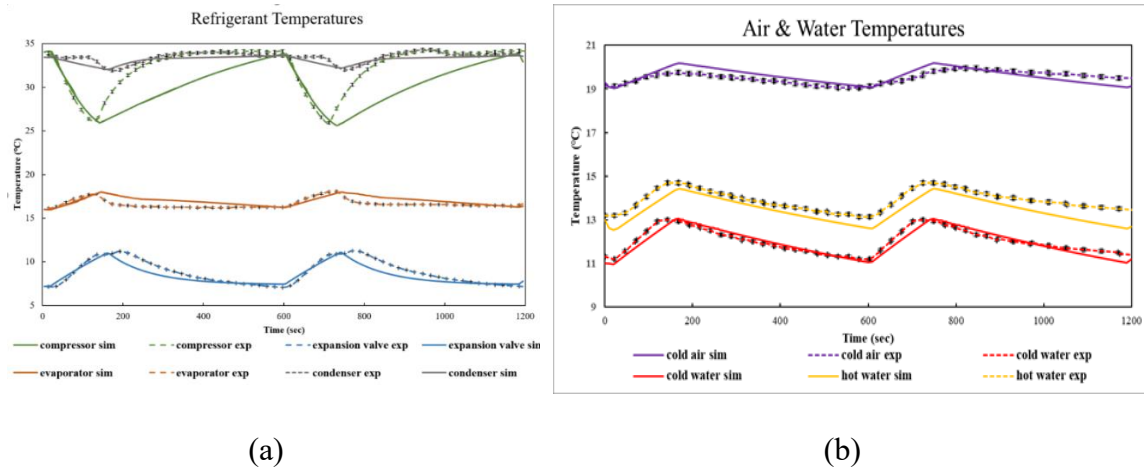


Figure 5.7: (a)Temperature profile of refrigerant under 2.3 kW thermal loading (b) Temperature profile of water and air loop under 2.3 kW thermal loading

The second experiment had a thermal loading of 2.3 kW of the chiller. The chiller had a capacity of 3 kW; hence, the system did not run continuously. As the thermal loading was less than the capacity of the chiller, the water in the chiller tank dropped below the set point. The controller detected this slight temperature drop in the tank and switched off the compressor and condenser fans. As shown in Figure 5.7 (a), at 20 s, the refrigeration cycle was switched off, and the refrigeration cycle pressure settles at 0.41 MPa. This drop in pressure at the outlet of the compressor and condenser (high-pressure lines) caused a temperature drop, which can be observed in the downward slopes of the compressor and

condenser temperatures. The pressure in the expansion valve and evaporator increases from a lower pressure to a higher resting pressure. Thus, a temperature rise can be observed in Figure 5.7(a) after 20 s. The pump still pumps water through the chiller tank, and the increasing evaporator temperature provides no cooling to the incoming water, which results in a rising water temperature throughout the loop, as shown in Figure 5.7(b) after 20 s.

As the water temperature crossed a threshold of 12 °C at 180 s, the controller switched on the compressor and condenser fans and the refrigerant flowed through the refrigerant cycle. Thus, high- and low-pressure sections were created, decreasing the evaporator temperature and increasing the compressor temperature to facilitate heat transfer. Figure 5.7(b) shows that the water in the chiller tank started to decrease towards the set-point temperature and reached it at 600 s.

Good agreement between the simulated and experimental data for the transient condition was observed, except for the compressor. The MRE calculated from the simulated data to the experimental values ranges from 3-18%. Although the model can simulate the ON-OFF timing and trends very closely, a time lag was observed between the simulation and the experiments. This effect was more pronounced during the compressor switch-on action. The time lag between the experiment and the simulation was further reduced by applying a time constant controller. The maximum deviation was observed for the refrigerant outlet temperature of the compressor (T_{cp}), as shown in Figure 5.7(b). The rise in temperature during the compressor switch-ON event was not well simulated by the model. This can be attributed to the thermal inertia (thermal diffusivity) of the insulating material. The temperature represented in Figure 5.7 is the measured temperature at the copper tube and

insulation interface. The exact configuration of the copper tube at this location was unknown.

5.5.2 Sensitivity Analysis

A model sensitivity analysis was performed with respect to the parameters that were categorized as inputs. These parameters were calculated using the correlations or values obtained from experiments. The heat transfer coefficient for evaporator, condenser, and cooling unit had a variation of $\pm 10\%$. These values were estimated using correlations; hence, an appropriate variation was chosen. The mass flow rate of the water, inlet ambient temperature, and cooling unit hot-air temperature were obtained from the experiments. A variation of $\pm 5\%$ was considered for these parameters, considering the measurement errors. The mass flow rates of refrigerant and air in the condenser are considered to have a variation of $\pm 5\%$, as these values were obtained from experiments and data sheets. The analysis showed that the model could generate responses to the aforementioned variations logically. Appendix 3 presents the details of the analysis.

5.5.3 Fault Evaluation

Faults were implemented in the model using their mathematical representation, as discussed in the previous section. Fault models were inserted into their respective component modules to simulate the fault conditions. Table 5.5 shows the different fault levels at which each fault was simulated in the model and the parameters used to simulate the faults.

Table 5.5. Simulated faults

Sr. No	Faults	Fault level	Parameters changed
1	Fan malfunction in cooling unit	10%, 50%	$g_{a,cu}$
2	Fouling in heat exchanger of cooling unit	10%	U_{cu}
3	Restriction in water loop	10%, 50%	g_w
4	Fouling in heat exchanger of evaporator	10%	U_e
5	Fan malfunction in condenser	10%, 50%	$g_{a,cn}$
6	Fouling in heat exchanger of condenser	10%	U_{cn}

A nominal fault level of 10% was considered for the fault simulations. However, for components, such as pumps, fans, and valves, 50% was also considered. Figure 5.8 illustrates the deviation of the fault parameters with respect to the normal condition. A positive deviation indicates an increase in the value of a parameter from the normal operating condition and a negative deviation indicates a decrease in the value of the faulty parameter with respect to the normal condition.

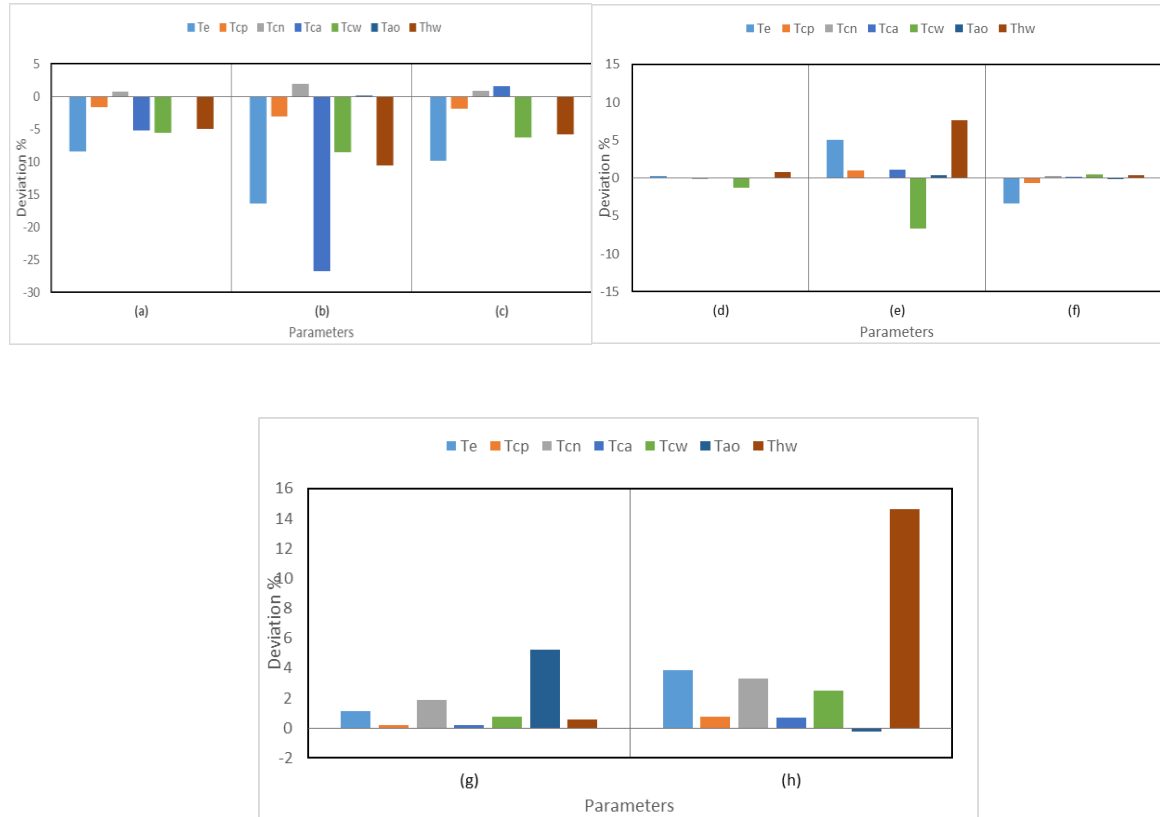


Figure 5.8: Fault simulation at varying fault levels (a) 10% fan malfunction in cooling unit (b) 50% fan malfunction in cooling unit (c) 10% fouling in cooling unit (d) 10% restriction in water loop (e) 50% restriction in water loop (f) 10% fouling in evaporator (g) 10% fan malfunction in condenser (h) 10% fouling in condenser

Fault#1– Figure 5.8 (a) presents the deviation of the parameters from normal operating conditions at a 10% fault level (Refer Table 5.5). Similarly, Figure 5.8 (b) shows the deviation in the parameters at the 50% fault level. It was observed that A maximum deviation of 8% occurred for a 10% fault. However, when the fault level was changed to 50%, a substantial deviation of 26% was observed.

Fault#2: A 10% fault level was considered for the simulation. The responses of the parameters are shown in Figure 5. 8 (c), which shows a decrease in the temperature of hot water (T_{hw}) of 5.8% and increase in the temperature of cold air (T_{ca}) of 1.5% with respect to the normal condition.

Fault#3– Restriction fault was simulated with 10% and 50% fault levels, as illustrated in Figure 5. 8 (d) and Figure 5.8 (e), respectively. The response for a 10% fault was found to be negligible (maximum of 0.4%). However, the degree of severity increased as the fault level increased. The maximum noticeable deviation estimated for T_{hw} was 7.6% at the 50% fault level.

Fault#4 – Figure 5.8(f) illustrate the fouling fault simulated at the 10% fault level. Fouling caused a decrease in the temperature of the evaporator (T_e) by 5%, which in turn caused the refrigerant temperature of the condenser (T_{cn}) to decrease by 1%. The temperature of cold air (T_{ca}) also shows a very small increase because of insufficient heat transfer occurring in the evaporator.

Fault#5– A 10% restriction to the condenser was simulated, and the effects on the temperatures are shown in Figure 5.8(g). This fault shows an increase in all temperatures, with the highest increase in the temperature of ambient air out of the condenser (T_{ao}) at 6%, and the temperature of the condenser (T_{cn}) at 2%. The increase in the exiting enthalpy of the refrigerant creates a cascade of increases in the exit enthalpy and temperature of all components.

Fault#6 – 5.8(h) show the system temperature deviation at 10% fault level for condenser fouling. A maximum deviation of 14% was observed for the temperature of the hot water (T_{hw}). There was also a noticeable increase in the temperature of the condenser (T_{cn}) and temperature of the evaporator (T_e) by 5% and 4%, respectively.

Each type of fault displayed a unique combination of increases and decreases in observed temperatures. Faults #1 and #2 displayed very similar patterns, except for the temperature of cold air (T_{ca}), which increased for Fault # 2 and decreased for Fault #1. Faults #3 and #4 also demonstrated increases in all parameters, except for the temperature of the evaporator (T_e) and temperature of the compressor (T_{cp}), which increased for fault #3 and decreased for fault #4. Faults #5 and #6 showed similar trends of increase, except for the temperature of ambient air out from the condenser (T_{ao}), which decreased for fault #6.

5.6 Simulation for FDD model

A test dataset was prepared using the simulation model developed for a small chiller, as shown in Figure 5.1. The three inputs that could be manipulated to change the operating conditions of the chiller were T_{set} , T_{ha} , and T_{ai} . These changes in the parameters result in variations in the loads of the chiller, thus providing varying operation conditions.

Table 5.6: Simulated operation conditions

Test No.	T _{set}	T _{abi}	T _{ha}
1	10	26	25
2	10	26	26
3	10	26	27
4	10	26	28
5	10	26	29
6	10	26	30
7	10	26	31
8	10	26	32
9	10	26	33
10	10	27	25
11	10	27	26
12	10	27	27
13	10	27	28
14	10	27	29
15	10	27	30
16	10	27	31
17	10	27	32
18	10	27	33

Test No.	T _{set}	T _{abi}	T _{ha}
25	10	28	31
26	10	28	32
27	10	28	33
28	10	29	25
29	10	29	26
30	10	29	27
31	10	29	28
32	10	29	29
33	10	29	30
34	10	29	31
35	10	29	32
36	10	29	33
37	10	30	25
38	10	30	26
39	10	30	27
40	10	30	28
41	10	30	29
42	10	30	30

Test No.	T _{set}	T _{abi}	T _{ha}
49	10	31	28
50	10	31	29
51	10	31	30
52	10	31	31
53	10	31	32
54	10	31	33
55	10	32	25
56	10	32	26
57	10	32	27
58	10	32	28
59	10	32	29
60	10	32	30
61	10	32	31
62	10	32	32
63	10	32	33
64	10	33	25
65	10	33	26
66	10	33	27

19	10	28	25
20	10	28	26
21	10	28	27
22	10	28	28
23	10	28	29
24	10	28	30

43	10	30	31
44	10	30	32
45	10	30	33
46	10	31	25
47	10	31	26
48	10	31	27

67	10	33	28
68	10	33	29
69	10	33	30
70	10	33	31
71	10	33	32
72	10	33	33

Nine temperature values for T_{abi} and T_{ha} were identified as inputs to the model. Each T_{abi} temperature value had nine different T_{ha} values, as listed in Table 5.6. Thus, 72 unique operating conditions were simulated with a fixed T_{ca} value and changing T_{ha} and T_{abi} values.

Reduced water flow in the evaporator and reduced air flow in the condenser are the two fault conditions simulated in the model. These faults are faults #3 and #5 mentioned in this chapter (5.4) represented in Table 5.7. These conditions were chosen because they were closest to the fault conditions in the ASHRAE RP-1043 dataset. The faults were simulated at four severity levels: 10, 20, 30 and 40%. Overall, 288 samples were generated for the fault conditions and 72 for the normal operating conditions.

Table 5.7: Small chiller fault models

Fault	Fault model	Severity level (FL)
Reduced evaporator water flow	$g_{w,fault} = (1 - FL)g_w$	0.1, 0.2, 0.3 and 0.4
Reduced condenser air flow	$g_{a,cn,fault} = (1 - FL)g_{a,cn}$	0.1, 0.2, 0.3 and 0.4

5.7 Summary

This chapter presents a response model capable of simulating faults and their responses to a modular cooling system for an IT rack. A component-based thermal modeling approach was used to represent a small modular cooling unit with interacting parameters. The system model was experimentally validated.

The simulated model represented the experimental setup within reasonable margins. Six different faults were identified for the system and implemented in the model. Faults such as restriction in the water loop, evaporator fouling, and fan malfunction in the condenser with a 10% fault level had very low deviation in its parameters, whereas faults such as fan malfunction in the cooling unit, fouling in the cooling unit, and fouling in the condenser showed higher variation in the response parameters for the 10% fault level. Nevertheless, the parameters that showed a small deviation for a 10% fault were found to be more responsive to a higher (50%) fault severity.

The model can produce distinguishing parameter values for various scenarios. In this study, we observed only the use of temperature measurements for each component. However,

when used in conjunction with flow rate and pressure, faults with a lower level of severity can be distinguished.

Two faults with reduced flow rates in the evaporator and condenser were simulated at four severity levels. These samples are used to test the FDD models in further chapters.

6. Implementations and Results

This chapter is divided into two main parts that analyze the two datasets: time-series data and 2D data. Time-series data were used to study hybrid architectures by comparing machine learning, deep learning, and hybrid approaches on different time-series datasets. The deviation matrix method was applied to both experimental and simulated data. Different training and testing datasets have been studied to understand the effect of simulation data on training FDD models as well as testing FDD models for various real-life scenarios.

6.1 Application of Hybrid network for FDD

The architecture proposed in Chapter 4.1 comprises two parts: feature selection and classification. The dimensionality reduction method compresses the dataset, which is then fed to a classifier that predicts the fault. With this architecture, the feature selection and the classifier can be chosen separately. In this study, PCA and LSTM-AE were selected as dimensionality reduction models, and SVM and ANN as the classifiers. One dimensionality reduction method was paired with another classifier. Thus, three model combinations are obtained as listed below:

1. PCA-SVM
2. LSTM-AE SVM
3. LSTM-AE ANN

This architecture enables the retrofitting of different dimensionality reduction methods to classifiers, thus enabling a more comprehensive evaluation. The selected models represent machine-learning and deep-learning methods, respectively. These specific methodologies were selected for comparison because they offer the opportunity to assess a complete machine learning approach (PCA-SVM), a hybrid approach utilizing neural networks for feature selection, a machine learning algorithm for classification (LSTM-AE SVM), and a fully AI-based approach (LSTM-AE ANN).

A regular LSTM network is added to the evaluation as a benchmark. This LSTM comprises an input layer with two hidden layers, with 65 and 35 variables in the first and second layers, respectively, as shown in Figure 6.1. The output layer consists of eight variables with a softmax layer to diagnose the eight classes.

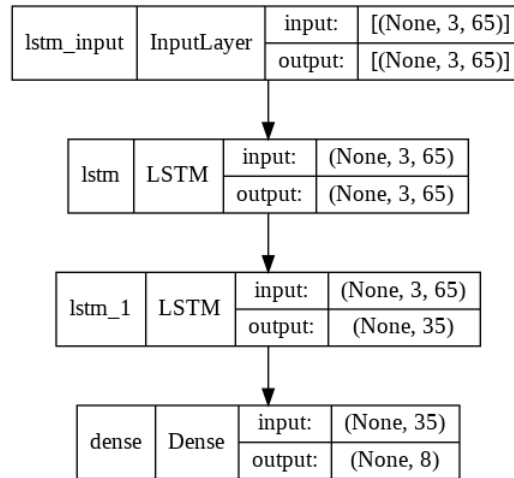


Figure 6.1: LSTM Architecture

Three types of datasets were used to train the networks. The complete dataset consists of 27 operating conditions and data for the ASHARE 1043-RP experiments, as explained in

Chapter 3.2.1. The steady-state dataset consisted of data from each test cycle, once the system reached a steady state. In the case study of the missing severity level, the training data contained three severity levels of faults, and the networks were tested against the missing severity level data. The dataset consisted of seven fault classes and a normal class, as listed in Table 6.1.

Table 6.1: List of classes

Class Label	Classes
0	Normal
1	Reduced Condenser Water Flow
2	Reduced Evaporator Water Flow
3	Refrigerant Leak
4	Refrigerant Overcharge
5	Excess Oil
6	Condenser Fouling
7	Non-Condensables in Refrigerant

6.1.1 Complete dataset

The complete dataset contained the data for the entire experimental cycle, which included the transient and steady-state phases of each cycle. The number of samples present in the dataset was 3464 with 65 features (Table 3.1), that is, 433 samples/class of one severity. The data were labeled numerically from 0 to 7. LSTM networks only accept input in a 3D

array format, which is data size \times time step \times features. Therefore, the dataset was first normalized to values between 0 and 1 and then reshaped to a 3D array. The shape of the input was $3460 \times 3 \times 65$. The dataset was then split into 70%, 20%, and 10% for training, testing, and validation, respectively. The architecture of the PCA is shown in Figure 4.1 in chapter 4.1.1.1, and that of the LSTM-AE is illustrated in Figure 4.5 in chapter 4.1.1.2.

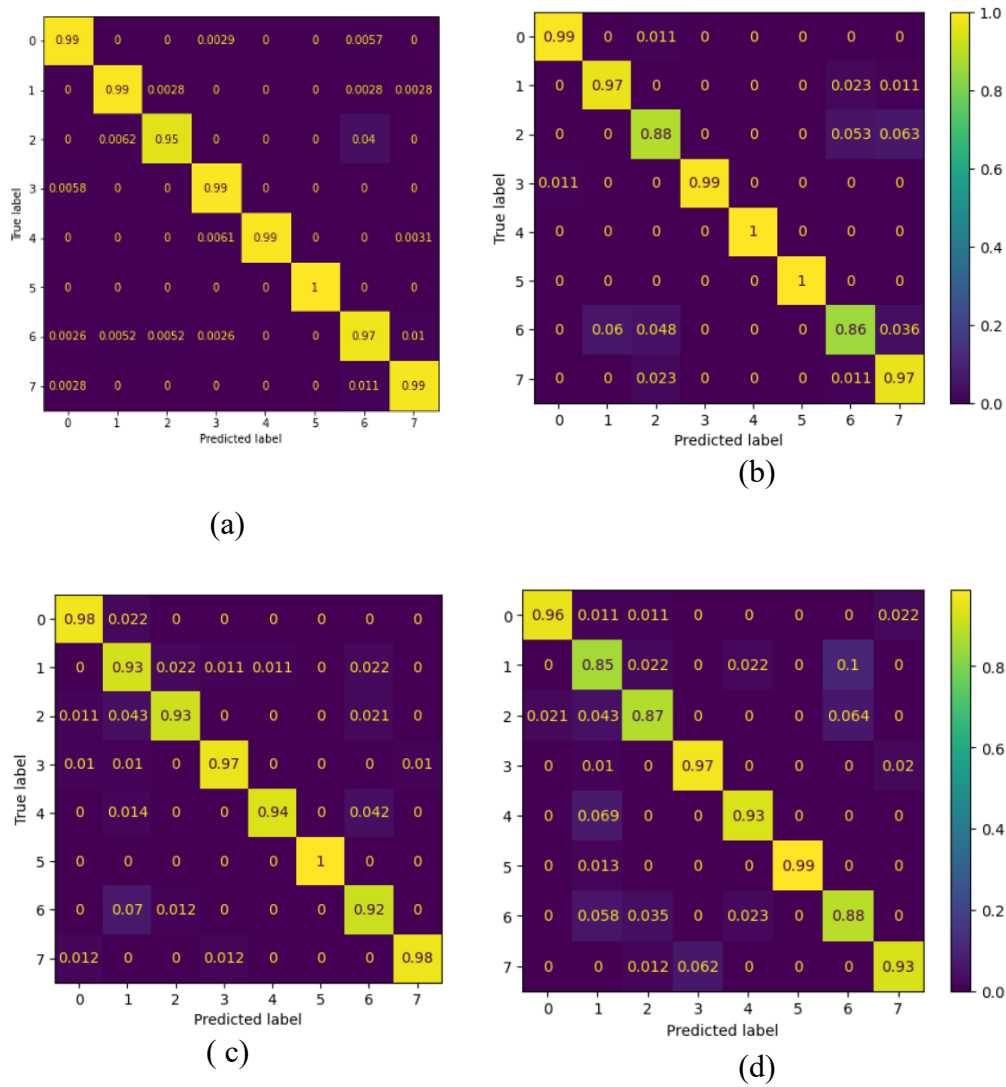


Figure 6.2 Confusion matrix of test data of the complete dataset (a) LSTM (b) PCA-SVM (c) LSTM AE- SVM (d) LSTM AE-ANN

The confusion matrix for the test data of the complete dataset is shown in Figure 6.2. All the models demonstrated a good fault detection rate of 96% and above. LSTM and PCA-SVM had the highest fault detection rate of 99%, as shown in Figure 6.2(a) and (b). The second highest detection rate was achieved by LSTM AE-SVM at 98%, as shown in Figure 6.2(d), followed by LSTM AE-ANN at 96%. Faults 1, 2, 4, and 6 appeared to be the most misclassified faults in the LSTM AE-SVM and LSTM AE-ANN. Faults 2 and 6 had the lowest prediction accuracies in all models, as low as 87% (Figure 6.2(d)) and 86% (Figure 6.2(b)), respectively. Faults 3 and 5 had the highest accuracy, above 97%, among other faults, throughout all the models.

Table 6.2: Classification accuracy of all models for complete data

Models	Complete data Accuracy
LSTM	98.52
PCA-SVM	95.53
LSTM-AE-SVM	95.52
LSTM-AE-ANN	92.2

The highest overall testing accuracy was shown in the LSTM. PCA-SVM and LSTM AE-SVM had the second highest accuracies of 95.53 and 95.52%, respectively, and LSTM AE-ANN had the lowest accuracy of 92.2%.

6.1.2 Steady state dataset

This study uses the steady-state data detailed in chapter 3.2.1. The data were subjected to the same preprocessing treatment described in the previous section. Hence, the shape of the input data was $(3438 \times 3 \times 65)$. The dataset was then divided into 70% for training, 20% for testing, and 10% for validation. LSTM, PCA, and LSTM AE remained the same (Figure 6.1, 4.1, and 4.4).

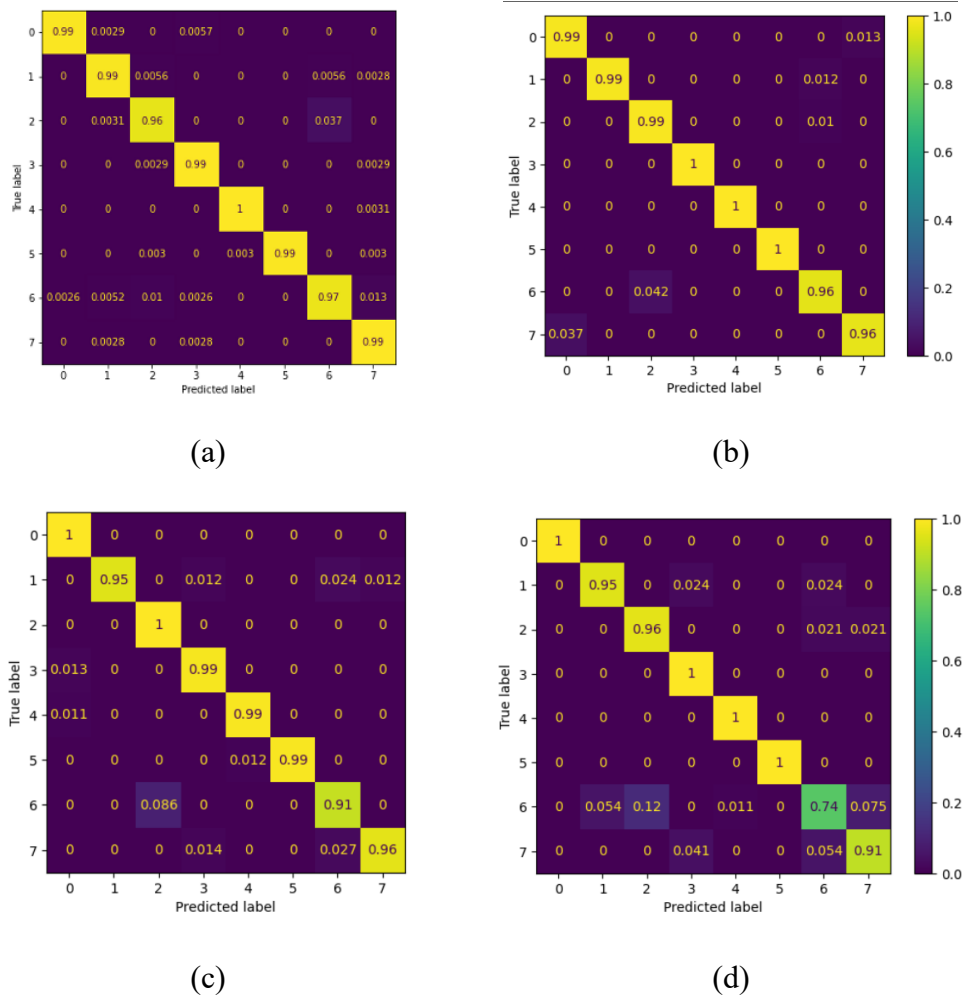


Figure 6.3: Confusion matrix of test data of the steady state dataset (a) LSTM (b) PCA-SVM (c) LSTM AE-SVM (d) LSTM AE-ANN

Fault detection rate is at 99% and higher for all the four models. Fault 6 has the least accuracy among all the models, the lowest in LSTM AE-ANN model at 74%, as displayed in Figure 6.3(d). Fault 7 is the second highest misclassified fault in the PCA-SVM, LSTM AE-SVM, and LSTM AE-ANN at 96%, 96%, and 91%, respectively (Figure 6.3 (b), (c), (d)). Though fault 1 displayed a slightly lower accuracy of 95% in LSTM AE-SVM (Figure 6.3 (c)). All faults, except for faults 3 and 6 in LSTM model has 99% accuracy or higher (Figure 6.3(a)). Faults 3, 4, and 5 had the highest accuracy of 99% and greater across all the models.

Table 6.3: Classification accuracy of all models for steady state data

Models	Steady state accuracy
LSTM (2 layers)	99.1
PCA-SVM	98.55
LSTM-AE-SVM	97.38
LSTM-AE-NN	94.33

The highest overall testing accuracy of 99.1% was observed for the LSTM. PCA-SVM had the second highest accuracy at 98.55%, followed by LSTM AE-SVM at 97.38%, and LSTM AE-ANN had the lowest accuracy of 94.33%.

6.1.3 Missing severity levels

The aim of this study was to train networks with three severity levels, departing from the four used in previous cases, and subsequently utilize the missing severity level data as the

testing dataset to evaluate the FDD methods. The training dataset consisted of a complete dataset at three fault severity levels at 10,20 and 40%. The model was tested at a severity level of 30 %.

Table 6.4. Classification accuracy of all models with missing severity level data

Models	Accuracy (%)
LSTM (2 layers)	68.12
PCA-SVM	90.28
LSTM-AE-SVM	71.39
LSTM-AE-ANN	45.8

As shown in Table 6.4, all the methods exhibited lower accuracy than the previous experiment. Notably, PCA-SVM performed the best with an accuracy of 90.28%, indicating a relatively robust performance even with the reduced dataset. The LSTM-AE SVM had the second-highest accuracy of 71.39%. LSTM showed a significant drop in accuracy, which was a result of a significant decrease in the number of samples in the training dataset.

6.2 Application of 2D input method

The following studies used three types of datasets: ASHRAE 1043-RP experimental data, ASHRAE 1043- RP simulation data, and small-chiller simulation data, as detailed in

chapter 3.2.1, 3.2.2, and 5.6, which contain normal and five fault conditions. The classes were numerically labelled 0-5 as shown in Table 6.5. As mentioned in chapter 4.3.1, the CNN architecture was implemented using the data. For comparison, an artificial neural network (ANN) (refer 4.1.2.2.1, Figure 4.7) and a Support Vector Machine (SVM), detailed in Section 4.2.2.1.1, were used for classification.

Table 6.5: Faults simulated in small chiller model

Class no.	Class name
0	Normal
1	Reduced Condenser Water flow rate
2	Reduced Evaporator Water flow rate
3	Refrigerant Overcharge
4	Refrigerant Leakage
5	Condenser Fouling

6.2.1 Dataset with only ASHRAE simulation data

The dataset used for this case was simulated data generated using the ASHRAE 1043-RP chiller model detailed in chapter 3.2.3. Each class consisted of 1377 samples with 20 features. The dataset of 8262 samples was preprocessed and split into 70%, 20%, and 10% for training, testing, and validation, respectively.

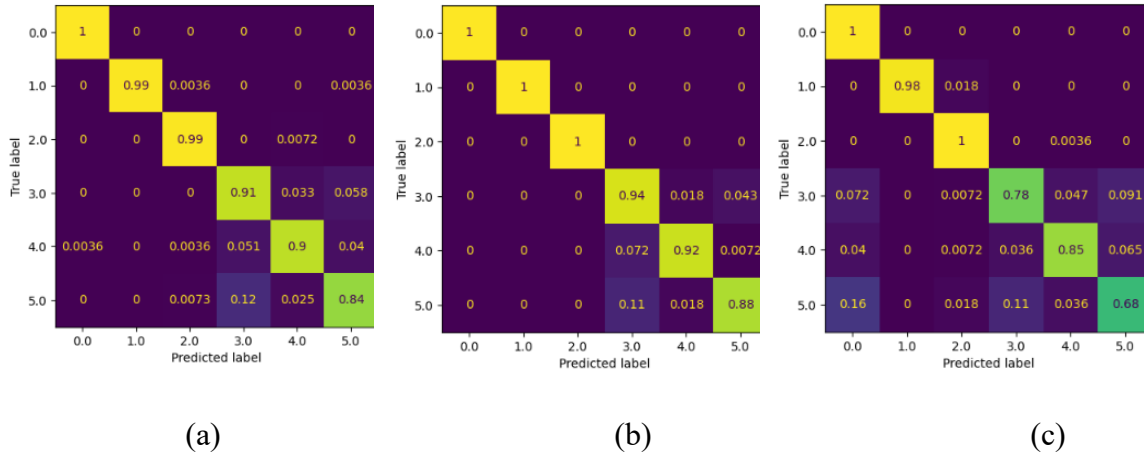


Figure 6.4: Confusion matrix for simulated dataset (a) Confusion matrix for CNN (b) Confusion matrix for ANN (c) Confusion matrix for SVM

Figure 6.4 illustrates the confusion matrix for the classification of the six classes. It is evident that 100% detection was achieved for all the three networks. Faults 1 and 2 are well diagnosed; however, Faults 3 and 4 have the second highest accuracy of above 90%, as displayed in Figure 6.4 (a) and (b). Fault 5 had the lowest accuracy across all the models, lowest at 68% for SVM (Figure 6.4 (c)), followed by CNN at 84% and 88% for ANN (Figure 6.4(b)). The CNN and ANN misdiagnosed fault 5 as fault 3. SVM also misdiagnoses fault 5 for class 0 in 16% of samples and fault 3 in 11%, as shown in Figure 6.4 (c). The overall highest accuracy at 95.58% was for neural networks, followed by 94.01% for CNN, and 88.81% for SVM.

This shows that the simulated dataset can generate data for different faults with distinguishing features that neural networks can detect and classify.

6.2.2 Dataset with combined simulation and experimental data

The dataset used for this case was a combination of simulated ASHRAE RP-1043 data without experimental operating conditions and experimental data from ASHRAE RP-1043, as mentioned in Section 3.2.1 and 3.2.3, respectively. This dataset contained 7614 simulated data samples and 648 experimental data samples. The dataset prepared for classification combines and randomly shuffles these two datasets and splits for training, testing, and validation by 70%, 20%, and 10%, respectively. The CNN and other networks maintain their architecture because the models are well fitted and do not require further fine-tuning of their parameters.

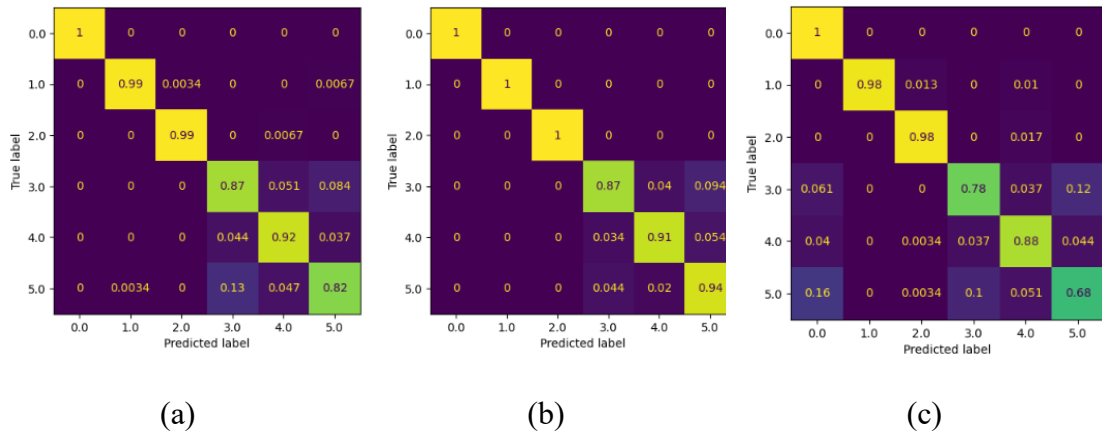


Figure 6.5: Confusion matrix for combined simulated and experimental data (a)

Confusion matrix for CNN (b) Confusion matrix for ANN (c) Confusion matrix for SVM

Figure 6.5 shows the confusion matrix for the three methods. The detection rate was 100% for all three methods. Faults 1 and 2 display almost 100% classification, and fault 4 is classified at 90% in CNN and ANN, as shown in Figure 6.5(a) and(b). Fault 3 had lower accuracy of 87% for CNN and ANN, and 78% for SVM. Fault 5 performed poorly at 82%

and 68% in CNN and SVM models whereas ANN had a good accuracy of 94%, as shown in Figure 6.5 (b). Fault 5 was the most misdiagnosed as fault 3. The highest overall accuracy was achieved by ANN at 95.23%, followed by CNN at 93.10% and SVM at 88.21 %.

6.2.3 Training data as simulated and testing data as experimental

The training dataset used was simulated ASHRAE 1043-RP data without experimental operating conditions, and the testing dataset was experimental data from ASHRAE RP-1043, as described in Section 3.2.1 and 3.2.3. The training dataset contained 7614 samples and the test dataset contained 648 samples. Thus, 92% of the dataset was used for training, and 8% for testing. The CNN and other networks maintain their architecture because the models are well fitted and do not require further fine-tuning of their parameters.

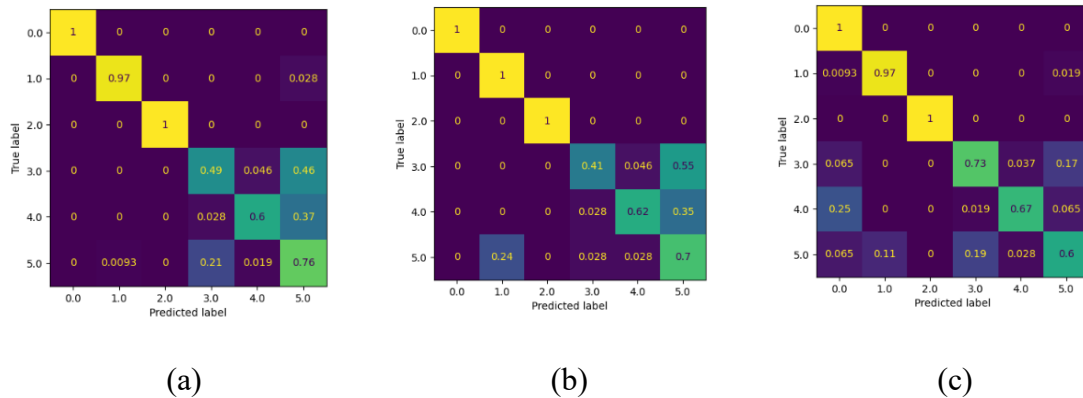


Figure 6.6: Confusion matrix for experimental data (a) Confusion matrix for CNN (b) Confusion matrix for ANN (c) Confusion matrix for SVM

Figure 6.6 illustrates the confusion matrix for the three fault classification methods. All three methods displayed 100% detection rates. Faults 1 and 2 display good classification accuracy, although they are slightly lower than those of the previous cases. Fault 3-5

perform poorly according to the confusion matrix. It was observed that in CNN and ANN, faults 3 and 4 were misclassified as fault 5, as shown in Figure 6.6 (a) and (b). However, SVM can classify fault 3-5 clearly with low accuracy (Figure 6.6 (c)). The highest overall accuracy was displayed by the SVM (82.87%), CNN (80.4%), and ANN (78.86%). Thus, it can be inferred that the small size of the testing data affects the classification of the CNN and ANN, as SVMs can perform well under smaller-sized datasets.

6.2.4 Influence of experimental data on testing

This case consisted of both simulated and experimental datasets. The training dataset consists of 8262 samples and the testing dataset consisted of 648 samples, which was 11.7% of the simulated data. The testing dataset had varying percentages of experimental data. For example, 60% of the 648 samples (i.e., 388) contained experimental data, and the remaining 40% (i.e., 259 samples) contained simulated data. The percentage of experimental data present in the testing dataset varied at 60%, 50%, 40%, and 20%.

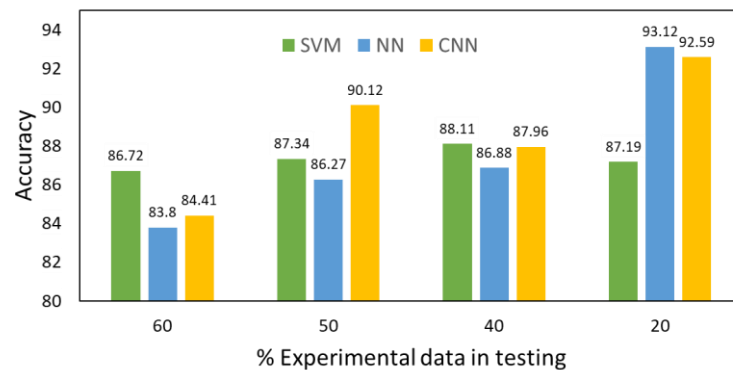


Figure 6.7: Accuracy w.r.t varying experimental data in testing dataset

Figure 6.7 shows the percentage change in accuracy with varying experimental data in the training dataset. The overall accuracy of all the models increased with a decrease in the

experimental data. The SVM had the most constant accuracy ranged from 86-88%. The other methods exhibited higher fluctuations in accuracy for each case. CNN displayed the highest accuracy of 90.12% at 50% experimental data, then decreased by 2.16% at 40% experimental data, and increased to 92.59% at 20% experimental data. The ANN has a constant increase through the varying experimental data and displays the highest accuracy among all cases at 93.12%.

6.2.5 Influence of experimental data on training

Four different training datasets were prepared for the case study. The training datasets consisted of varying percentages of experimental data at 60%, 50%, 40%, and 20%, and the rest of the training dataset was simulated. The test data consisted of only experimental data. The test data contains 1652 samples, and the total number of training data samples was 6610. 60% of the training data were experimental, that is, 3966.

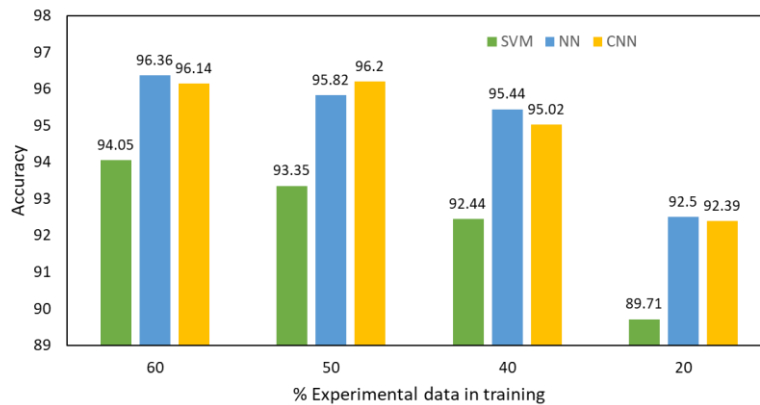


Figure 6.8: Accuracy w.r.t varying experimental data in training dataset

Figure 6.8 demonstrates the overall test accuracy of the three models with varying experimental data in the training dataset. It was observed that, with decreasing percentages of experimental data present in the training, the test accuracy decreased for all three models.

The ANN and CNN models exhibit the highest accuracies of 96.14% and 96.36%, respectively, for 60% of the experimental data. The 50% experimental data presence in the training data were 95.82 and 96.2% for the ANN and CNN models, respectively. As the experimental data decreased to 40% of the training data, the accuracy fell to 95.44%, 95.02%, and 92.44% for ANN, CNN, and SVM, respectively. It can be concluded that the ANN and CNN have the highest accuracies of 60 and 50%, respectively, with a low difference in accuracy between the two datasets.

6.2.6 Testing using missing severity level

This case used a dataset containing simulated and experimental ASHRAE 1043-RP data for the training. This dataset contained faults with severity levels of 10%, 20%, and 30%. A testing dataset was generated using the operating conditions listed in Table 2 at severity levels of 5%, 15%, and 25%. The training dataset consists of 8262 samples and the testing dataset consists of 2430 samples.

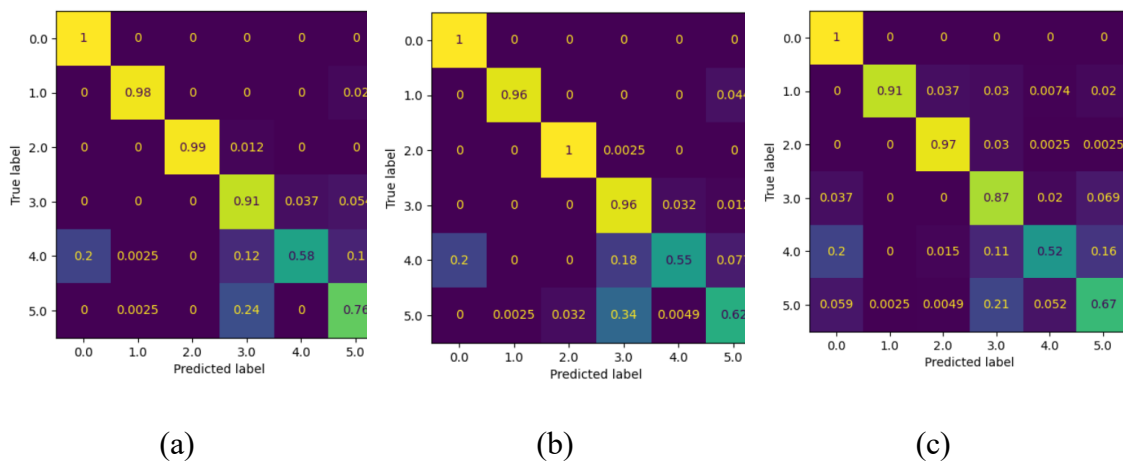


Figure 6.9: Confusion matrix for different severity level dataset (a) Confusion matrix for CNN (b) Confusion matrix for ANN (c) Confusion matrix for SVM

Figure 6.9 shows the confusion matrices of the three models. These matrices show the percentage of samples accurately predicted for the testing dataset containing different fault severity levels compared to those of the training dataset. All the three models exhibited an 80% detection rate. Faults 1, 2, and 3 also exhibited high accuracy from 0.87-1. All three models seem to struggle to classify faults 4 and 5. CNN had the highest overall accuracy at 86.87%, followed by ANN at 84.69%, and SVM at 82.38%.

6.2.7 Testing using near normal and other normal data

The training dataset consisted of 8262 samples, of which 7614 samples were from the simulated ASHRAE 1043-RP model and 648 samples were from the experimental ASHRAE 1043-RP. The test dataset comprised of near-normal experimental data of ASHRAE 1043-RP for 324 samples. Thus, the testing dataset comprises 5% of the total dataset.

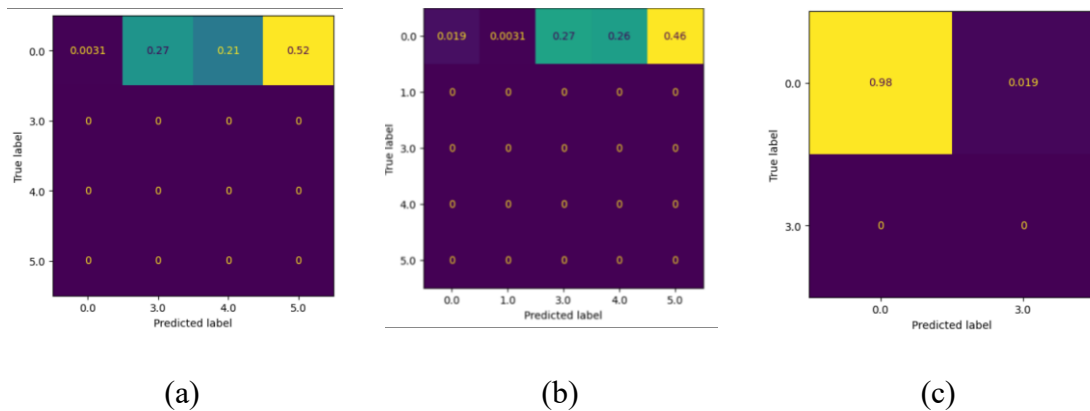


Figure 6.10: Confusion matrix of near normal test data (a) Confusion matrix for CNN (b) Confusion matrix for ANN (c) Confusion matrix for SVM

Figure 6.10 compares the confusion matrices for the near-normal test data. AI methods perform poorly by misclassifying normal (class 0) to Fault 5. SVM was able to classify near-normal conditions as normal with 98% accuracy.

6.2.8 Testing using small chiller data

The DL models (NN and CNN) used in this case were pre-trained models from Case 6.2.7, which were trained on ASHRAE simulated and experimental data and did not contain any small chiller data. A test dataset was generated using the small-chiller model under the operating conditions described in Chapter 5.6. Faults 1 and 2 and normal conditions were simulated at three severity levels, creating 864 samples for testing. The pre-trained DL models (ANN and CNN) from case 6.2.7, which were trained using the simulation and experimental ASHRAE RP-1043 datasets, were used for classification.

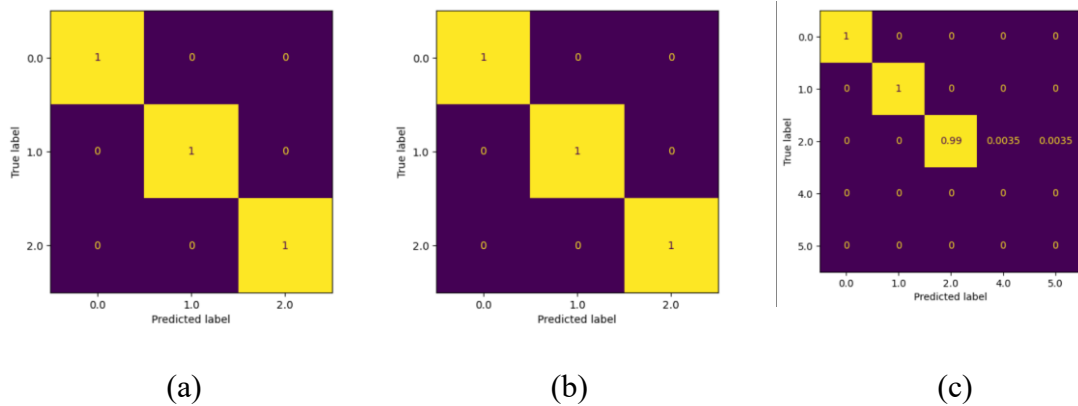


Figure 6.11: Confusion matrix of small chiller test data (a) Confusion matrix for CNN (b) Confusion matrix for ANN (c) Confusion matrix for SVM

Figure 6.11 shows the confusion matrix for the small-chiller test data for the three models. All three models showed 100% detection rate and 100% accuracy in classifying

all classes, except the SVM model with 99% accuracy for Fault 2. As shown in Figure 6.11(c), very few samples were misclassified for faults 4 and 5. Hence, the confusion matrix is 5×5 . The other models did not have misclassification cases; hence, a 3×3 confusion matrix is displayed.

6.3 Summary

Three datasets were prepared to implement the hybrid architecture, and three models were developed using combinations of machine and deep learning methods for dimensionality reduction and classifier modules. The machine learning and hybrid models performed the best on the complete dataset. Machine learning performed best when only a steady-state dataset was used to train and test the models. The machine learning model also performed best when tested against faults of an unknown severity level.

The deviation matrix method was applied to ASHRAE RP-1043 experimental and simulated data. Three FDD models were built to diagnose faults: a 2D CNN, an ANN, and SVM. First, simulated data was used to train and test the three models. All the faults were detected and diagnosed. The second case combined both experimental and simulated data and found good detection and diagnostic accuracy for all models. The third and fourth scenarios varied the experimental data in the testing and training datasets, respectively. It was found that, with a decreasing percentage of experimental data, testing the accuracy of all models tends to increase. The increasing percentage of experimental data in the training showed increasing accuracy in the three models. The models were tested under three scenarios in which FDD models were not trained. The models were tested against test data

containing faults of different severity levels compared with the training set. The 2D CNN model performed the best with the highest accuracy in this scenario. In the second case, near-normal conditions were used to test the models. Only SVM was able to detect this as normal operation. The last scenario used simulated small-chiller data to detect and diagnose two faults. All three models were performed with high accuracy.

7. Discussion

This chapter discusses the results of the case studies in chapter 6. This chapter discusses the findings into three categories: effect of steady state, data augmentation using simulated data, missing severity level, and generalizability (7.1-7.4). The implications of the findings are detailed in chapter 7.5, and the limitations of the study and method are discussed in chapter 7.6 and 7.7.

7.1 Effect of Steady State Data

In the real world, a continuous stream of data from sensors is obtained from a system that undergoes transient-state and steady-state operations. Two datasets are prepared to study this case. A dataset consisting of data from the entire test cycle is referred to as a complete dataset. The other dataset contains only steady-state data extracted from the complete dataset, which is referred to as the steady-state dataset.

Comparing the overall testing accuracy of the four methods, LSTM performed the best, followed by PCA-SVM, LSTM AE-SVM, and LSTM AE-NN for the complete dataset (Table 6.2). These methods follow the same rank when using steady-state data (Table 6.3). PCA-SVM and LSTM AE-SVM exhibited a low difference of 0.01% in accuracy for the complete dataset. As a result, the two-dimensional reduction methods can be considered equally effective. The results derived from the steady-state data indicate a general improvement in the accuracy of all models. A noticeable increase in the difference between the LSTM AE-SVM and PCA-SVM models was observed, with an increase of 1.17 in

accuracy. Although the overall accuracy increased, the LSTM AE model did not perform as effectively as the PCA model in retaining information following the dimensionality reduction.

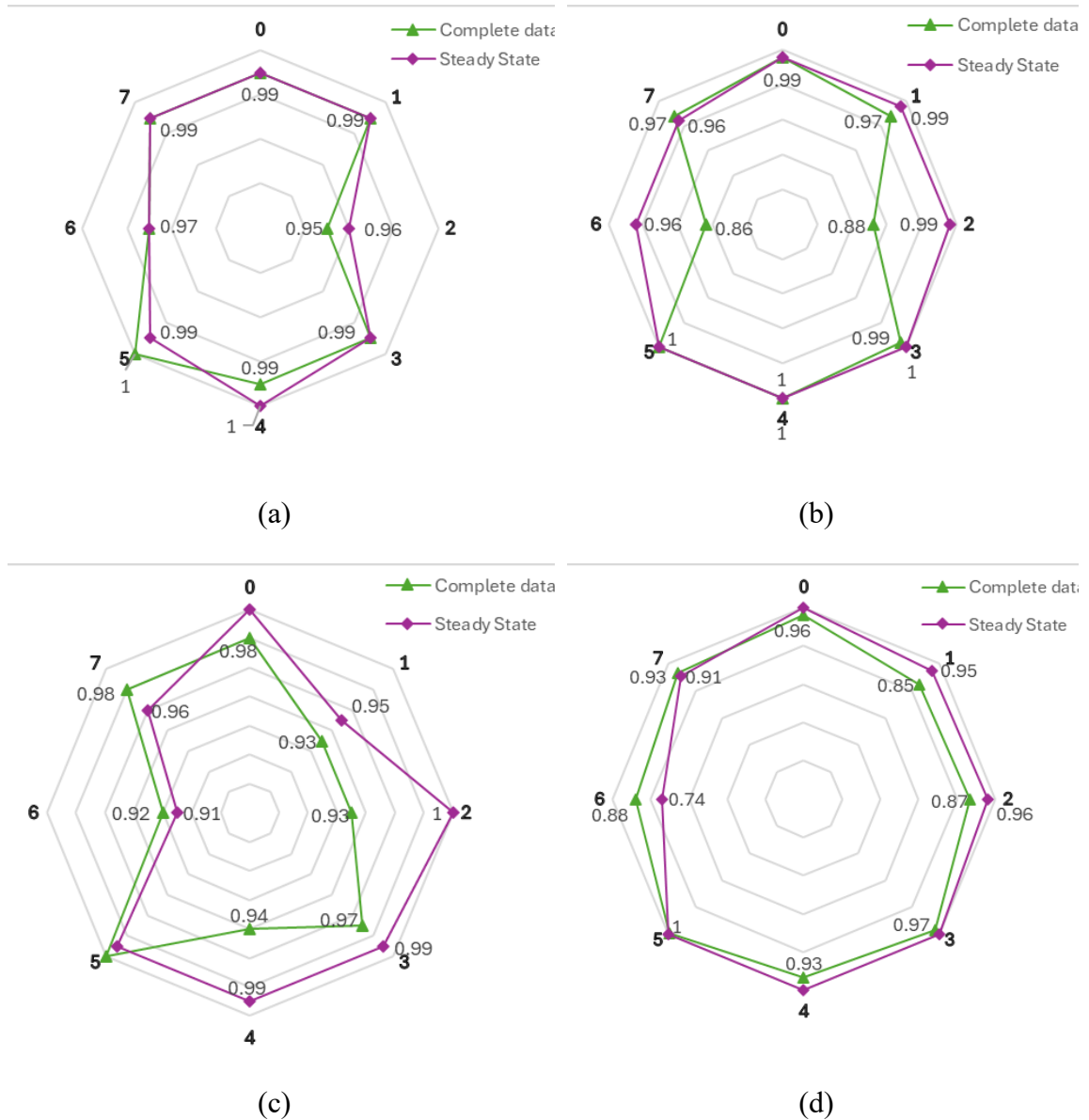


Figure 7.1 Test accuracy for two datasets (a) LSTM (b) PCA-SVM (c) LSTM AE- SVM (d) LSTM AE-ANN

Figure 7.1 illustrates the testing accuracy of the complete dataset and steady state for each method and each class. Examining the individual class accuracy will reveal differences in the trends between the two datasets. Faults 2 and 6 show significant increases under steady-state data in the PCA-SVM. Fault 6 had the lowest accuracy in the steady state and complete data in the LSTM AE-SVM. Faults 2 and 4 exhibit a significant increase in accuracy. In the LSTM AE-ANN, faults 1, 2, and 6 have low accuracy in the complete dataset and show a significant increase after implementing the steady state, except for fault 6, which decreased.

Faults 2, 4, and 6, which have reduced evaporator flow, refrigerant overcharge, and condenser fouling, respectively, have been shown to be difficult to diagnose using all methods. Steady-state data improved the accuracy. The transience in the complete dataset has variance, which results in decreased accuracy. A steady-state filter decreases this variance, thereby increasing the accuracy of most faults and methods.

Faults 2, 4 and 6 are more difficult to diagnose in the complete dataset because the fault signatures present in the transience of the data is not clearly distinguishable. Hence there is an increase in accuracy of these faults using steady state data. LSTM has ranked highest in both types of dataset. Higher number of features present in the LSTM dataset has helped the algorithm diagnose faults better. In dimensionality reduction methods machine learning algorithm PCA-SVM has performed best with LSTM AE-SVM coming a close second. While PCA shows better capabilities in dimensionality reduction in comparison to LSTM AE but SVM has proven to be a strong classifier. Machine learning algorithm is better in generalizing than AI methods and perform better in limited amount of data.

7.2 Simulation and Experimental data

The steady-state data simulated using ASHRAE RP-1043 consisting of normal and five fault conditions with three severity levels were used to build and test the CNN, ANN, and SVM models (as shown in chapter 6.2.2). This dataset, when preprocessed using the deviation matrix method, showed 100% detection and good classification accuracy for faults. This indicated that the simulation model could produce distinct fault conditions.

In Section 6.2.3, the models are trained using simulated data and tested against experimental data. CNN and ANN have been shown to achieve 100% detection, whereas SVM have 75% detection. Fault 5 has been seen to be misclassified with fault 3 at a higher percentage than fault 4 for CNN and ANN as illustrated in Figure 6.6 (a) and (b). Although the SVM does not have the highest detection rate, it has a high classification accuracy for the experimental data. As mentioned in chapter 7.2, the fault refrigerant overcharge (Fault 3) and condenser fouling (Fault 5) have a lower classification accuracy. Fault 1 and 2 have higher classification accuracy because there are features in the dataset such as flow rates in evaporator and condenser which are direct indicators of these faults. In this case, SVM has the highest accuracy; thus, it is able to generalize better than its deep learning counterparts and can adapt to provide better results.

It is important to understand the influence of experimental data on testing data. It was observed (Figure 6.7) that with decreasing experimental data in the testing data, the overall accuracy of the three models increased notably in the ANN and CNN models. This corresponds to the fact that the majority of the dataset comprises simulated data and the

increasing percentage of simulated data is representative of the majority dataset. CNN performed well with 50% of the experimental data in the test dataset.

After investigating the influence of the experimental data on testing, the effects of experimental data training were examined. This is a more practical scenario, as training requires a large amount of data, and supplementing it with experimental data will help to address the data shortage issue. The decreasing percentage of the experimental data shows a downward trend in the overall testing accuracy for all models. The testing data consisted of experimental data; thus, the accuracy was affected by the decreasing percentage of training data. CNN and ANN had the highest accuracy across all cases. All models had accuracy close to or greater than 90%. A training set containing 60-40% of the experimental data would perform well.

7.3 Missing Severity Level Data

The results of testing the models with untrained fault severity levels are presented in chapter 6.1.3 and 6.2.6. The severity levels of faults can vary from 2% until failure, which can be as high as 95%. This is a large range of values that requires the production of a large amount of training data. The models used for the hybrid network and deviation matrix method were used to test the severity levels of faults that were not present in the training data.

Chapter 6.1.3 details the training and testing data used. The LSTM AE-SVM, LSTM AE-ANN, and benchmark LSTM models performed poorly. The significant decrease in the dataset size resulting from the removal of the entire severity level suggests insufficient

training. The models seem to have memorized the training data due to low versatility in it. Hence the models perform poorly on the new missing severity level data. The PCA-SVM performed comparatively better at 90.28%. Owing to the generalization capability of machine learning, PCA-SVM was able to diagnose faults of different severity levels.

The deviation matrix method and models CNN, ANN, and SVM were tested against untrained severity levels of 5, 15 and 25% (chapter 6.2.6). All three models exhibited a fault detection rate of approximately 80%. CNN and ANN had higher accuracies for faults 1, 2, and 3. Fault 5 (condenser fouling) was misclassified as fault 3 (refrigerant overcharge) in all the models, but it was the highest in the ANN. This trend was observed throughout the study. Faults 4 and 5 had lower classification accuracies among all models, but CNN showed better accuracy. Hence, the overall accuracy was highest for CNN. The 2D CNN could recognize fault signatures as low as 5% of the severity level.

7.4 Testing New Data

The deviation matrix method uses normal operation data as a benchmark and calculates the deviation of the fault features from the normal features. This results in a 2D matrix of zeros for normal operation. It has been proven to be effective for fault detection; however, when considering real-life operating scenarios, there is variability in normal operating conditions for which data-driven models have not been trained. The deviation was calculated for these near-normal operating conditions, as described by ASHRAE RP-1043, which are operations that did not completely meet the manufacturer's specifications but were deemed to be normal operations. These deviations were nonzero. The three models trained with

normal and five faults were tested with deviation values of near-normal operation (chapter 6.2.7). Only SVM, with the highest accuracy of 98%, was able to detect it as a normal operation, and CNN and ANN misclassified it as faults 3, 4, and 5 (Figure 6.10). The low number of samples available for testing could be the reason for the poor accuracy of the CNN and ANN, as they are deep learning models. The performance of these deep learning models can be improved by using near-normal data in the training dataset. However, SVM accuracy is a promising ability to be incorporated into real-life models.

In all previous cases, the models were trained and tested using ASHRAE RP-1043 chillers, which were 90-ton centrifugal chillers. The models were tuned and tested by using a specific chiller. Different types and sizes of chillers affect the features (measurements) obtained from the chiller. To test the generalizability of the model, data from a small chiller were investigated. Test data were generated using a small chiller model (Chapter 5.6). It consists of normal and faults 1 and 2. The simulated dataset was tested against trained models. A 100% fault detection and accuracy were achieved for all models except SVM, with 99% accuracy for Fault 2. This indicates that, by using the deviation matrix method, fault signatures are more distinguishable and can be recognized in different systems for these faults.

7.5 Implications

- Steady state

The majority of the datasets used to develop the FDD method use steady-state data. The study in section 7.1 concludes that using steady-state data shows an improvement in accuracy compared to the complete dataset in hybrid models.

- Simulation data

Data simulated using physics-based models of HVAC systems and air conditioners were used to test FDD methodologies (Nie et al. 2023; Simmini et al. 2022). Some studies have also used simulated data to train and test models using real-world data (Karami & Wang, 2018; Miyata et al., 2020). Yan et al. used GAN-based models to supplement a dataset for diagnosing fault severity levels (K. Yan, 2021; K. Yan et al., 2022). In the study discussed in Section 7.2, the ability of the chiller model to generate fault data is verified. The influences of the experimental and simulated data on the training and testing datasets were analyzed. It was found that in the case of very limited experimental data, if the FDD models are trained on simulated data, then the recommended 50% of the testing data can contain experimental data to obtain reasonable accuracy while using the deviation matrix method for preprocessing and the 2D CNN for FDD. A training dataset can contain 60-40% of the experimental data to provide high accuracy using 2D CNN and ANN for experimental testing data. This provides a recommended limit on how much data can be supplemented using physics-based models; thus, it is still feasible to be applied in the real world.

- Missing severity level

The most commonly used dataset in FDD for chillers was developed using the ASHRAE RP-1043 experimental data. This dataset consisted of eight faults with four severity levels of 10, 20, 30%, and 40% (shown in Table 3.3). Hence, the most investigated faults contain these four severity levels. No study has attempted to diagnose faults at other severity levels. CNN has been observed to perform best at fault diagnosis when confronted with unseen fault severity levels. The CNN, along with preprocessing data using the deviation matrix method, has shown good accuracy. This helps to address one of the shortcomings of real-world applications.

- Generalizability

The chiller system had variable operating conditions. Testing the models under near-normal operating conditions helps understand the generalization capability of the FDD method. Only SVM could diagnose near-normal conditions. Therefore, when developing an FDD system, an SVM can be used as a fault detection method to detect normal and near-normal conditions. Studies have been conducted using transfer learning methods specifically developed for cross-operation and cross-system FDD (Du, Liang, et al., 2023; G. Li, Chen, et al., 2023; J. Liu et al., 2021).

Small chiller data obtained using the physics-based model were tested on a pretrained model using the ASHRAE experimental data. Lee et al. used ASHRAE RP-1043 historical experimental data on machine-learning classifiers to successfully detect and diagnose

faults in 100 refrigeration systems (2022). The study showed that it significantly reduced energy consumption due to faults.

7.6 Limitations

This study has some limitations that are discussed in this section. While attempting to convert 1D time-series data into 2D images, the number of generated samples was insufficient for training and testing the CNN. A physics-based model of the experimental setup was used to supplement the experimental data. The development of physics-based models for chiller systems is complex and requires expert knowledge. Software programs, such as EnergyPlus (*EnergyPlus*, n.d.), TRNSYS (*TRNSYS*, n.d.), and Modelica (*Modelica*, n.d.) can be used to decrease the effort and shorten the time needed to develop the system model. However, these software models must be fine-tuned to the system characteristics to generate useful data.

The physics-based models used in this study to generate data had restrictions on the minimum and maximum values that could be used for the inputs, which limited the range of the operating conditions that could be produced. Users should also ensure that the model converges for each unique condition to obtain accurate and useful data. These models also require computing time to achieve a steady state, which is required for training. The type of fault that can be simulated in the models can be limited, depending on the approach used to develop the model. Not all faults replicated using the ASHRAE RP-1043 model were able to implicate the small chiller model.

These models were developed by using only the ASHRAE RP-1043 dataset. Using data other than ASHRAE's would help to study the generalizability of the deviation matrix method further than being dependent on small chiller simulated data.

The deviation matrix method is the deviation of each faulty feature from normal operation. This makes it largely dependent on what is classified as normal operation. It also requires an initial collection of normal operating conditions of a particular system. Therefore, any faults that might occur during the commissioning of the system must be identified before collecting the normal benchmark data.

7.7 Summary

This chapter discusses the results presented in Chapter 7. The results are divided into four categories. In summary, the steady-state data performed better than the complete dataset when using time-series data for the hybrid network architecture. The simulation and experimental data were studied using 2D CNN, ANN, and SVM. The ability to use simulation data as a supplement to training and testing data was assessed. The test data with untrained severity levels were prepared and tested. The models were able to diagnose faults with varying accuracy. When discussing new data testing, the new data consists of small chiller data and near-normal operating conditions. These three models, along with the deviation matrix method, have shown promising results.

8. Conclusion

This chapter summarizes the research performed and discussed in this thesis, and also includes recommendations for future work to continue and expand on the research.

8.1 Concluding remarks

This study aims to understand how data-driven FDD models for chillers can adapt to variable operating and fault conditions.

As a result, a preprocessing method was developed that helps FDD models detect and diagnose faults under varying operating and fault conditions. Using this method, data-driven models can detect near-normal operations and diagnose faults at untrained fault severity levels. The deviation matrix method displays patterns unique to these faults. It was also observed that the intensity of the parameters in the fault pattern was dependent on the severity level of the fault.

The dataset was supplemented with a diverse array of operating conditions by employing simulated data from the ASHRAE RP-1043 model and small chiller model. Because of the limited data available for developing data-driven methods, the use of simulated data from physics-based models has been suggested. The reliability of using the simulated data for training and testing was also assessed. Up to 60-40% of training data can have simulated data, whereas testing data are experimental data that closely represent real-world data.

Data-driven models consisting of a machine learning model SVM and deep learning 2D CNN and ANN models were tested with simulated fault severity levels that were not

present in the training dataset. All models were able to detect and diagnose faults. The CNN proved to be the best method for fault classification. In real-world applications, it is not possible to train models with every possible variation in fault severity level. Thus, the models were tested to assess their ability to diagnose the faults.

Near-normal operation data, which is another form of variation in operating conditions in which the system runs normally but does not meet all manufacturer specifications. Such data were also tested, and the machine learning method SVM was the only model that was able to successfully detect it as a normal operation. Simulated data from the small chiller model were used to diagnose the two faults using pre-trained models on the ASHRAE RP-1043 dataset. All models detected and diagnosed the faults. This indicates that transfer learning is an effective method to develop cross-system FDD models.

A hybrid network consisting of a dimensionality reduction method and a classifier was proposed. The hybrid networks were trained and tested using steady-state and complete datasets. There was a noticeable improvement in the overall classification accuracy of the steady-state data over that of the complete dataset. It was also noted that PCA and SVM, as machine learning dimensionality reduction and classifier, performed better than LSTM AE and ANN for their deep learning counterparts.

Studies conducted on various training and testing datasets have provided insights into the effects of varying operating conditions on data-driven FDD methods. The deviation matrix method helped detect and diagnose faults in previously unseen and untrained data. The use of simulated data to supplement or enrich datasets with insufficient data addresses the

limited availability of data for FDD development. Creating a large number of unique operating conditions and simulating physics-based models can help increase the data variability in datasets. Applying transfer learning to detect and diagnose faults in different types of chillers can also help increase the reliability of the FDD method rather than being chiller-type-specific. Although including unsteady data is more realistic, using steady-state data provides better classification accuracy. Hence, most studies have used steady-state data to develop FDD models.

Implementing FDD to address varying conditions across systems requires uniformity in the data collection and implementation. The features used in the deviation matrix method were a collection of system measurements and calculated values. These measurements are commonly found in the monitoring systems of chillers. Therefore, FDD models, along with the deviation matrix method, can be applied to other chillers. Uniformity in data collection will ensure further development of generic FDD systems. Creating an IoT environment with cloud computing, thus enabling the continuous updating of FDD, is one of the ways to implement and develop a more comprehensive model.

8.2 Recommendations for future work

Further experimentation is required to collect experimental data on small chillers and their faults to understand the extent of transfer learning effectiveness. Making more fault experimental data publicly available to researchers will help in the development of more generalized FDD methods.

An online FDD system with an SVM as a fault detector can help detect near-normal operating conditions. This can be used as the first layer of detection, and the advancing layers are deep-learning models for fault classification. The similarity and relation between the fault severity levels can be utilized to further estimate the fault severity level as the third layer of the FDD after fault classification. Applying the FDD method to an operating chiller provides more clarity regarding the practical applicability of this method.

The problem statement stated in this thesis was how data-driven methods can adapt to varying operating and faulty conditions. This solution comprises of two approaches. A deviation matrix method is developed to detect near-normal operations and faults of different severity levels. This also addresses the research gap in limited real-world data. The second approach was to generate more data using physics-based models and test the feasibility of using simulation data for FDD development. This study attempts to address the research gap created by the limited amount of data available to researchers. The application of the simulated small chiller data implemented on the data driven using the deviation matrix method indicates that the reliability of the FDD method can be achieved by transfer learning. The simulated data was used to supplement the dataset. However, they cannot replace the real-world data. It is important to address real-world data issues to develop relevant and applicable FDD methods. A good data-driven FDD system for chillers should accommodate varying operating conditions such as component degradation, controllers, or environmental factors, and different fault severity levels.

Appendix - 1

A1. Pressure drop in refrigerant loop heat exchanger

The pressure drop correlation was used to calculate the pressure drop within the heat exchangers to estimate the steady-state pressure conditions at the outlet of the evaporator and condenser. The heat exchanger was divided into control volumes and the pressure drop across each control volume was estimated using the following correlation:

A phase change occurred in both heat exchangers of the refrigerant loop. The Lockhart–Martinelli correlation was used to estimate pressure drop. The two-phase pressure drop under the liquid-only flow condition is expressed as

$$\phi^2 = \frac{(\Delta P)_{tp}}{(\Delta P)_{lo}} \quad (\text{A1-1})$$

The multiplier relation is expressed as a function of the Martinelli parameter (X_{tt}) as follows:

$$\phi^2 = 1 + \frac{C}{X_{tt}} + \frac{1}{X_{tt}^2} \quad (\text{A1-2})$$

$$X_{tt} = \left(\frac{1 - x_{cv}}{x_{cv}} \right)^{0.9} \left(\frac{\rho_{g,r}}{\rho_{l,r}} \right)^{0.5} \left(\frac{\mu_{l,r}}{\mu_{g,r}} \right)^{0.1} \quad (\text{A1-3})$$

Souza et al. (1992) examined the application of the Lockhart and Martinelli multipliers for refrigerant systems and proposed a better fitted correlation for pressure drop estimation using the Martinelli parameter (X_{tt}). This correlation is expressed as follows:

$$\phi^2 = (1.376 + c_1 X_{tt}^{-c_2})(1 - x)^{1.75} \quad (\text{A1-4})$$

Where,

$$0 < Fr_l \leq 0.7$$

$$c_1 = 4.172 + 5.480Fr_l - 1.564Fr_l^2$$

$$c_2 = 1.773 - 0.169Fr_l$$

The vapor quality was calculated by dividing the heat exchanger into several control volumes. The vapor quality for each control volume was calculated as follows:

$$x = \frac{h_{cv} - h_{l,r}}{h_g - h_{l,r}} \quad (\text{A1-5})$$

In contrast, h_{cv} is estimated from the power (received or lost) in each control volume (Q_{cv}) depending on the type of heat exchanger.

$$h_{cv} = \frac{Q_{cv}}{g_r} \quad (\text{A1-6})$$

It was assumed that the power received or lost from the heat exchangers was uniformly distributed over the tube length of the heat exchangers. Similarly, the multiplier is estimated for each control volume.

The single-phase pressure drop for the liquid-only flow was estimated as follows:

$$(\Delta P)_{lo} = \frac{2fG^2L}{\rho_{l,r}d} \quad (\text{A1-7})$$

where friction factor (f) was calculated using the Blasius correlation for a smooth pipe ($2100 < Re < 10^5$).

$$f = \frac{0.079}{Re^{0.079}} \quad (A1-8)$$

Thus, the frictional pressure drop for each phase of the refrigerant was estimated, and the overall pressure drop across the heat exchangers was calculated for the steady-state condition.

Appendix - 2. Overall Heat Transfer Coefficient

A2.1 Evaporator

Refrigerant side:

The refrigerant enters the evaporator in the liquid phase and exits in the vapor phase. Correlations were used to calculate the heat-transfer coefficient for each phase. The refrigerant phases in the evaporator are categorized into four types, depending on their vapor quality. The phases are liquid, two-phase, mist, and super-heated phases. The heat-transfer coefficients for high flow and boiling were calculated using the following correlation:

- Liquid phase region

$$\alpha_{l,r} = 0.023 Re_{l,r}^{0.8} Pr_{l,r}^{0.4} \left(\frac{k_l}{d_i} \right) \quad (\text{A2-1})$$

- Two-phase region

$$\alpha_{tp} = E\alpha_{l,r} + S\alpha_{nb} \quad (\text{A2-2})$$

$$E = 1 + 24000Bo^{1.16} + 1.37 \left(\frac{1}{X_{tt}} \right)^{0.86} \quad (\text{A2-3})$$

$$S = (1 + 1.15e^{-6}E^2Re_l^{1.17})^{-1} \quad (\text{A2-4})$$

$$\alpha_{nb} = 55pr^{0.12}(-0.4343 \ln pr)^{-0.55}M^{-0.5}q^{0.67} \quad (\text{A2-5})$$

- Mist phase region

$$\alpha = \frac{(1 - x)\alpha_{tp} + (x - 0.85)\alpha_{g,r}}{0.15} \quad (\text{A2-6})$$

- Super-heated region

$$\alpha_{g,r} = 0.023 Re_{g,r}^{0.8} Pr_{g,r}^{0.4} \left(\frac{k_g}{d_i} \right) \quad (\text{A2-7})$$

The heat transfer coefficients under low flow conditions ($Re < 2300$) (Er. R. K Rajput, 2012) were calculated using the correlations given by:

$$\alpha_{l,r} = 3.66 \left(\frac{k_l}{d_i} \right) \quad (\text{A2-8})$$

$$\alpha_{g,r} = 3.66 \left(\frac{k_g}{d_i} \right) \quad (\text{A2-9})$$

The overall heat transfer coefficient for the refrigerant tube of the evaporator was obtained by averaging the individual tube section heat transfer coefficients (liquid, two-phase, and vapor phases) over the tube length with different thermodynamic qualities.

Water side:

A water tank (chiller tank) can exhibit forced convection, mixed convection, or only natural convection. Only natural convection may occur for a large-diameter water tank or in the case of a loss of the water-circulating pump power. Mixed convection can occur for high-power input or low-flow-velocity conditions, where forced convection is not sufficient for the removal of heat. A fault in the circulating system can result in low flow conditions in the chiller. The heat-transfer mode is determined by the Richardson number (Ri), and is

expressed as $Ri = Gr/Re^2$. Typically, natural convection is negligible for $Ri < 0.1$, forced convection is negligible for $Ri > 10$, and both modes of heat transfer are present at $0.1 < Ri < 10$.

The heat transfer coefficient for forced convection was calculated using the correlation developed (Cengel, 1998).

$$\alpha_{forced} = 0.0266 Re_d^{0.805} Pr^{0.33} \left(\frac{k_w}{d} \right) \quad (A2-10)$$

The heat-transfer coefficient for natural convection was calculated using the correlation developed by Churchill et al. {Churchill, 1975 #68} (1975).

$$Nu_{natural} = \left\{ 0.6 + \frac{0.387 Ra_d^{\frac{1}{6}}}{\left[1 + \left(\frac{0.559}{Pr} \right)^{\frac{9}{16}} \right]^{\frac{8}{27}}} \right\}^2 \quad (A2-11)$$

Mixed convection is calculated using the following relation:

$$Nu = [Nu_{forced}^{1/n} + Nu_{natural}^{1/n}]^{1/n} \quad (A2-12)$$

The relationship evolved from the experimental data, which suggests an area-averaged heat transfer for a mixed convection heat transfer process, as suggested by Incropera et al.

The Ri for the tank is calculated to be less than 0.1 under steady state conditions, which implies that forced convection is dominant in the chiller tank; however, for flow transients, it may have mixed or pure natural convection.

Finally, the overall heat transfer coefficient of the evaporator is expressed as follows:

$$U_e = \frac{1}{\frac{1}{\alpha_w A_o} + \frac{r_i \ln\left(\frac{r_o}{r_i}\right)}{k_{wall}} + \frac{1}{\alpha_r A_i}} \quad (\text{A2-13})$$

A2.2 Condenser

Refrigerant side:

This is a fin-tube heat exchanger. Similar to the evaporator, a phase change occurs inside the condenser from the super-heated gas to the sub-cooled liquid occurs inside the condenser. The heat transfer coefficient was calculated for each region. Cavillini-Zecchin developed a correlation for two-phase condensing refrigerants.

Super-heated region:

$$\alpha_{g,r} = 0.023 Re_{g,r}^{0.8} Pr_{g,r}^{0.4} \left(\frac{k_g}{d_i}\right) \quad (\text{A2-14})$$

Two-phase region:

$$\alpha_{tp} = 0.05 Re_{eq}^{0.8} Pr_{l,r}^{0.33} \left(\frac{k_l}{d_i}\right) \quad (\text{A2-15})$$

$$Re_{eq} = Re_l(1 - x) + x \left(\frac{\mu_g}{\mu_l}\right) \left(\frac{\rho_g}{\rho_l}\right)^{0.5} Re_g \quad (\text{A2-16})$$

Liquid phase region:

$$\alpha_{l,r} = 0.023 Re_{l,r}^{0.8} Pr_{l,r}^{0.4} \left(\frac{k_l}{d_i} \right) \quad (\text{A2-17})$$

The heat transfer coefficients under low-flow conditions ($Re < 2300$) were calculated using the following correlations:

$$\alpha_l = 3.66 \left(\frac{k_l}{d_i} \right) \quad (\text{A2-18})$$

$$\alpha_g = 3.66 \left(\frac{k_g}{d_i} \right) \quad (\text{A2-19})$$

The overall heat transfer coefficient for the refrigerant tube of the condenser was obtained by averaging the individual tube section heat transfer coefficients (liquid, two-phase, and vapor phases) over the tube length with different thermodynamic qualities.

Air side:

Kays and London developed a correlation for fin- and tube-type heat exchangers for the heat transfer coefficient of the air-side. The following correlations were used for the air-side heat transfer coefficient estimation under forced fan flow:

$$\alpha_a = 0.011 Re_a^{0.65} Pr_a^{0.33} \left(\frac{k_a}{d_i} \right) \quad (\text{A2-20})$$

The Nusselt number under free convection was estimated under the compressor switched-off condition. Following this correlation, Kern D. Q. was used for the estimation.

$$\alpha_a = \left[Gr Pr \left(\frac{S_f}{d_m} \right) \right]^{\frac{1}{3}} \left(\frac{k_m}{d_m} \right) \quad (A2-21)$$

The overall heat transfer coefficient for the condenser is furnished as below,

$$U_{cn} = \frac{1}{\frac{A_o}{\alpha_a(A_{fin}\eta_{fin} + A_b)} + \frac{A_o}{A_i} \frac{r_i \ln \left(\frac{r_o}{r_i} \right)}{k_{wall}} + \frac{A_o}{\alpha_r A_i}} \quad (A2-22)$$

Appendix - 3 Model Sensitivity Analysis

A model sensitivity analysis was performed to obtain a better understanding of the parameters and their effects on the model output. The parameters considered are the heat transfer coefficients in the cooling unit, evaporator, and condenser; the mass flow rate of water, refrigerant, and air in the condenser; the inlet ambient temperature in the condenser; and the hot air temperature in the cooling unit. The selected parameters were inputs to the model, which were calculated using the correlations or values obtained from the experiments. The heat transfer coefficients for the evaporator, condenser, and cooling unit had a variation by $\pm 10\%$. These values were estimated using correlations; hence, appropriate variation was chosen. The measured values obtained from the experiments on the system were the mass flow rate of water and the temperature of the inlet ambient and hot air in the cooling unit. A variation of $\pm 5\%$ was considered for these parameters, taking into consideration measurement errors. The mass flow rates of refrigerant and air in the condenser are considered to have a variation of $\pm 5\%$, as these values were obtained from experiments and data sheets.

The sensitivity index (SI) is defined as follows

$$S.I = \frac{\frac{dy}{y}}{\frac{dx}{x}}$$

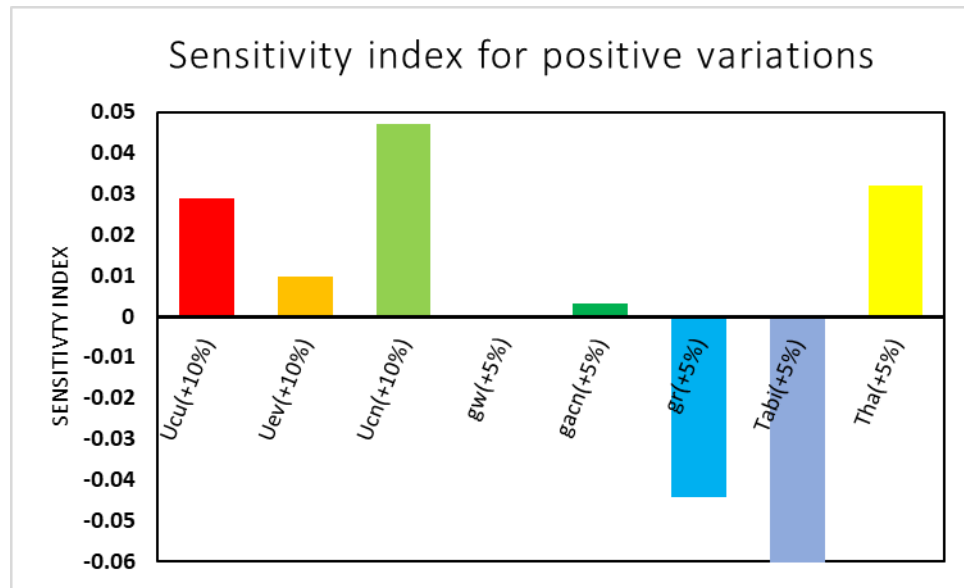
dy : change in output parameter

y: output parameter (nominal)

dx: change in input parameter

x: input parameter (nominal)

The output was considered to be COP of the chiller. The COP encompasses all the parameters of the chiller, and hence is a fitting output to be monitored.



FigureA3-1: Sensitivity index for positive variations

The figure above illustrates the effect of the positive variation in parameter on the COP. The highest positive impact was caused by the heat-transfer coefficient of the evaporator. This indicates that any change in this parameter significantly increases the COP. The ambient inlet temperature of the condenser is also highly sensitive and negatively affects the COP. As shown in Figure A3-1, any change in the mass flow rate of water has little effect on the COP.

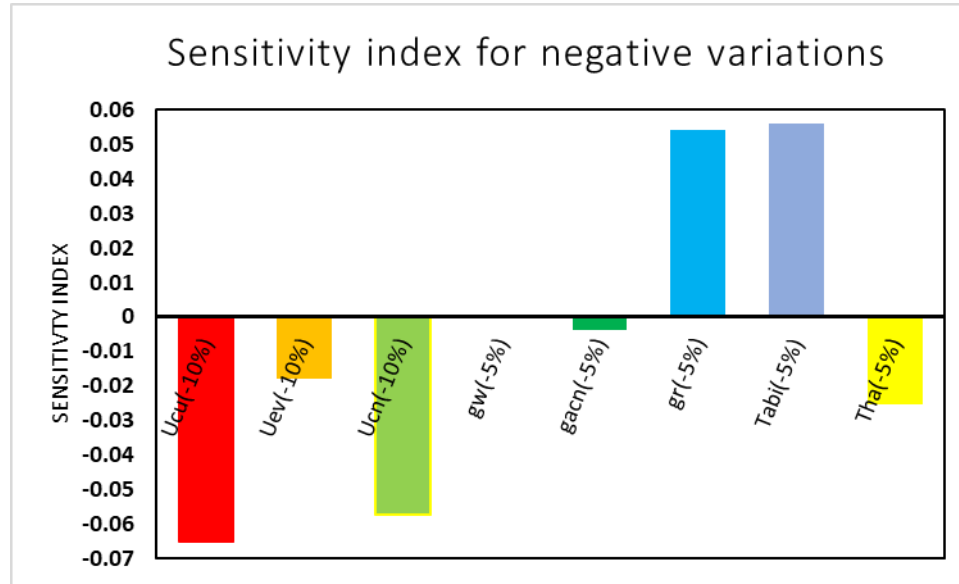


Fig.A3-2: Sensitivity index for negative variations

Figure A3-2 illustrates the sensitivity index for negative variations. The heat transfer coefficient of the cooling unit had the most negative impact on the COP. In FigureA3-2, the mass flow rate of water had almost no effect on the COP. The negative variation in the mass flow rate of the refrigerant and ambient inlet temperature of the condenser resulted in a positive change in the COP.

Hence, the parameters that are most sensitive with respect to the COP are the heat transfer coefficient of the cooling unit and condenser, mass flow rate of the refrigerant, and ambient inlet temperature for the condenser.

Bibliography

- A. Beghi, L. Cecchinato, F. Peterle, M. Rampazzo, & F. Simmini. (2016). *Model-based fault detection and diagnosis for centrifugal chillers*. 158–163.
<https://doi.org/10.1109/SYSTOL.2016.7739744>
- Bartholomew, D. J., Steele, F., Steele, F., & Moustaki, I. (2011). *Analysis of Multivariate Social Science Data* (2nd ed.). Chapman and Hall/CRC.
<https://doi.org/10.1201/b15114>
- Bell, I. H., Wronski, J., Quoilin, S., & Lemort, V. (2014). Pure and Pseudo-pure Fluid Thermophysical Property Evaluation and the Open-Source Thermophysical Property Library CoolProp. *Industrial & Engineering Chemistry Research*, 53(6), 2498–2508. <https://doi.org/10.1021/ie4033999>
- Bi, J., Wang, H., Yan, E., Wang, C., Yan, K., Jiang, L., & Yang, B. (2024). AI in HVAC fault detection and diagnosis: A systematic review. *Energy Reviews*, 3(2), 100071.
<https://doi.org/10.1016/j.enrev.2024.100071>
- Bonvini, M., Sohn, M. D., Granderson, J., Wetter, M., & Piette, M. A. (2014). Robust on-line fault detection diagnosis for HVAC components based on nonlinear state estimation techniques. *Applied Energy*, 124, 156–166.
<https://doi.org/10.1016/j.apenergy.2014.03.009>
- Braun, J. E. (2003). Automated Fault Detection and Diagnostics for Vapor Compression Cooling Equipment. *Journal of Solar Energy Engineering*, 125(3), 266–274.
<https://doi.org/10.1115/1.1591001>

- Breuker, M., & Braun, J. (1998). Common Faults and Their Impacts for Rooftop Air Conditioners. *HVAC&R Research*, 4(3), 303–318.
<https://doi.org/10.1080/10789669.1998.10391406>
- Browne, M. W., & Bansal, P. K. (2001). An elemental NTU- ϵ model for vapour-compression liquid chillers. *International Journal of Refrigeration*, 24(7), 612–627. [https://doi.org/10.1016/S0140-7007\(00\)00091-8](https://doi.org/10.1016/S0140-7007(00)00091-8)
- Browne, M. W., & Bansal, P. K. (2002). Transient simulation of vapour-compression packaged liquid chillers. *International Journal of Refrigeration*, 25(5), 597–610.
[https://doi.org/10.1016/S0140-7007\(01\)00060-3](https://doi.org/10.1016/S0140-7007(01)00060-3)
- Cengel, Y. A. (1998). *Heat Transfer* (International Edition). MC. Graw-Hill Book Company,.
- Chandrashekar, G., & Sahin, F. (2014). A survey on feature selection methods. *Computers & Electrical Engineering*, 40(1), 16–28.
<https://doi.org/10.1016/j.compeleceng.2013.11.024>
- Chen, K., Chen, S., Zhu, X., Jin, X., & Du, Z. (2023). Interpretable mechanism mining enhanced deep learning for fault diagnosis of heating, ventilation and air conditioning systems. *Building and Environment*, 237, 110328.
<https://doi.org/10.1016/j.buildenv.2023.110328>
- Chen, K., Wang, Z., Gu, X., & Wang, Z. (2021). Multicondition operation fault detection for chillers based on global density-weighted support vector data description. *Applied Soft Computing*, 112, 107795. <https://doi.org/10.1016/j.asoc.2021.107795>

- Chen, K., Yadav, A., If, A., Meng, Y., & Zhu, K. (2019). Improved Crack Detection and Recognition Based on Convolutional Neural Network. *Modelling and Simulation in Engineering, 2019*, 1–8. <https://doi.org/10.1155/2019/8796743>
- Chen, Y., Yang, Q., Chen, Z., Yan, C., Zeng, S., & Dai, M. (2023). Physics-informed neural networks for building thermal modeling and demand response control. *Building and Environment, 234*, 110149. <https://doi.org/10.1016/j.buildenv.2023.110149>
- Cheng, F., Cai, W., Liao, H., Wu, B., & Dubey, S. (2021). Fault Detection and Isolation for Chiller System based on Deep Autoencoder. *2021 IEEE 16th Conference on Industrial Electronics and Applications (ICIEA)*, 1702–1706. <https://doi.org/10.1109/ICIEA51954.2021.9516436>
- Cheung, H., & Braun, J. E. (2016). Empirical modeling of the impacts of faults on water-cooled chiller power consumption for use in building simulation programs. *Applied Thermal Engineering, 99*. <https://doi.org/10.1016/j.applthermaleng.2016.01.119>
- Choi, Y., & Yoon, S. (2021). Autoencoder-driven fault detection and diagnosis in building automation systems: Residual-based and latent space-based approaches. *Building and Environment, 203*, 108066. <https://doi.org/10.1016/j.buildenv.2021.108066>
- Churchill, S. W., & Chu, H. H. (1975). Correlating equations for laminar and turbulent free convection from a vertical plate. *International Journal of Heat and Mass Transfer, 18*(11), 1323–1329.

- Comstock, M. C., Braun, J. E., & Groll, E. A. (2001). The Sensitivity of Chiller Performance to Common Faults. *HVAC&R Research*, 7(3), 263–279.
<https://doi.org/10.1080/10789669.2001.10391274>
- Comstock, Matthew C. & Braun, James E. (1999). *Development of analysis tools for the evaluation of fault detection and diagnostics for chillers*. ASHRAE. *Controls, Settings, And Functions; 200 Series Microtech Control Panel—McQuay PFS 155C Operation And Maintenance Manual [Page 15]*. (n.d.). ManualsLib.
Retrieved May 27, 2024, from
<https://www.manualslib.com/manual/1620651/Mcquay-Pfs-155c.html>
- Cortes, C., & Vapnik, V. (1995). Support-vector networks. *Machine Learning*, 20(3), 273–297. <https://doi.org/10.1007/BF00994018>
- Coulomb, D. ; D. (2015). *The Role of Refrigeration in the Global Economy* (In 29th Informatory Note on Refrigeration Technologies). International Institute of Refrigeration.
- Cui, J., & Wang, S. (2005). A model-based online fault detection and diagnosis strategy for centrifugal chiller systems. *International Journal of Thermal Sciences*, 44(10).
<https://doi.org/10.1016/j.ijthermalsci.2005.03.004>
- Ding, G., Zhang, C., & Lu, Z. (2004). Dynamic simulation of natural convection bypass two-circuit cycle refrigerator–freezer and its application: Part I: Component models. *Applied Thermal Engineering*, 24(10), 1513–1524.
<https://doi.org/10.1016/j.applthermaleng.2003.12.009>

- Du, Z., Chen, S., Li, P., Chen, K., Liang, X., Zhu, X., & Jin, X. (2023). Knowledge-extracted deep learning diagnosis and its cloud-based management for multiple faults of chiller. *Building and Environment*, 235, 110228.
<https://doi.org/10.1016/j.buildenv.2023.110228>
- Du, Z., Liang, X., Chen, S., Li, P., Zhu, X., Chen, K., & Jin, X. (2023). Domain adaptation deep learning and its T-S diagnosis networks for the cross-control and cross-condition scenarios in data center HVAC systems. *Energy*, 280, 128084.
<https://doi.org/10.1016/j.energy.2023.128084>
- Duarte, M., Pires, L., Silva, P., & Gaspar, P. (2017). Experimental comparison between R409A and R437A performance in a heat pump unit. *Open Engineering*, 7.
<https://doi.org/10.1515/eng-2017-0011>
- EnergyPlus*. (n.d.). Retrieved June 3, 2024, from <https://energyplus.net/>
- Er. R. K Rajput. (2012). *Heat and Mass Transfer*.
- Fan, Y., Cui, X., Han, H., & Lu, H. (2020). Feasibility and improvement of fault detection and diagnosis based on factory-installed sensors for chillers. *Applied Thermal Engineering*, 164, 114506. <https://doi.org/10.1016/j.applthermaleng.2019.114506>
- Gálvez, A., Diez-Olivan, A., Seneviratne, D., & Galar, D. (2021). Fault Detection and RUL Estimation for Railway HVAC Systems Using a Hybrid Model-Based Approach. *Sustainability*, 13(12), Article 12. <https://doi.org/10.3390/su13126828>
- Gao, H., Zhao, B., & Gao, X. (2022). A Feature Extraction Method Based on Two-branch Sparsity and Manifold Regularized Temporal Convolutional Network for Chiller

Fault Diagnosis. *2022 China Automation Congress (CAC)*, 3060–3064.

<https://doi.org/10.1109/CAC57257.2022.10055458>

Gao, J., Han, H., Ren, Z., & Fan, Y. (2021). Fault diagnosis for building chillers based on data self-production and deep convolutional neural network. *Journal of Building Engineering*, 34, 102043. <https://doi.org/10.1016/j.jobbe.2020.102043>

Gao, Y., Han, H., Lu, H., Jiang, S., Zhang, Y., & Luo, M. (2022). Knowledge mining for chiller faults based on explanation of data-driven diagnosis. *Applied Thermal Engineering*, 205, 118032. <https://doi.org/10.1016/j.applthermaleng.2021.118032>

Gao, Y., Han, H., Ren, Z. X., Gao, J. Q., Jiang, S. X., & Yang, Y. T. (2021). Comprehensive study on sensitive parameters for chiller fault diagnosis. *Energy and Buildings*, 251, 111318. <https://doi.org/10.1016/j.enbuild.2021.111318>

Goodfellow, I., Bengio, Y., & Courville, A. (2016). *Deep Learning*. MIT Press.

Grald, E. W., & MacArthur, J. W. (1992). A moving-boundary formulation for modeling time-dependent two-phase flows. *International Journal of Heat and Fluid Flow*, 13(3), 266–272. [https://doi.org/10.1016/0142-727X\(92\)90040-G](https://doi.org/10.1016/0142-727X(92)90040-G)

Guo, Q., Shao, J., & Ruiz, V. (2005). Investigation of support vector machine for the detection of architectural distortion in mammographic images. *Journal of Physics: Conference Series*, 15, 88–94. <https://doi.org/10.1088/1742-6596/15/1/015>

Gupta, S., Venugopal, A., & Jidhu Mohan, M. (2022). Fault Detection and Diagnosis using AutoEncoders and Interpretable AI - Case Study on an Industrial Chiller. *2022 IEEE International Symposium on Advanced Control of Industrial Processes (AdCONIP)*, 198–203. <https://doi.org/10.1109/AdCONIP55568.2022.9894262>

Hacker, A., Gorthala, R., & Thompson, A. (n.d.). *An Approach to Bringing Automated Fault Detection and Diagnosis (AFDD) Tools for HVAC&R Into the Mainstream*.

Retrieved August 12, 2024, from

[https://asmedigitalcollection.asme.org/IMECE/proceedings-](https://asmedigitalcollection.asme.org/IMECE/proceedings-abstract/IMECE2019/59438/V006T06A050/1073243?redirectedFrom=PDF)

[abstract/IMECE2019/59438/V006T06A050/1073243?redirectedFrom=PDF](https://asmedigitalcollection.asme.org/IMECE/proceedings-abstract/IMECE2019/59438/V006T06A050/1073243?redirectedFrom=PDF)

Han, H., Cui, X., Fan, Y., & Qing, H. (2019). Least squares support vector machine (LS-SVM)-based chiller fault diagnosis using fault indicative features. *Applied Thermal Engineering*, 154, 540–547.

<https://doi.org/10.1016/j.applthermaleng.2019.03.111>

Han, S., Shao, H., Huo, Z., Yang, X., & Cheng, J. (2022). End-to-end chiller fault diagnosis using fused attention mechanism and dynamic cross-entropy under imbalanced datasets. *Building and Environment*, 212, 108821.

<https://doi.org/10.1016/j.buildenv.2022.108821>

Harris, C. R., Millman, K. J., van der Walt, S. J., Gommers, R., Virtanen, P., Cournapeau, D., Wieser, E., Taylor, J., Berg, S., Smith, N. J., Kern, R., Picus, M., Hoyer, S., van Kerkwijk, M. H., Brett, M., Haldane, A., del Río, J. F., Wiebe, M., Peterson, P., ... Oliphant, T. E. (2020). Array programming with NumPy. *Nature*, 585(7825), 357–362. <https://doi.org/10.1038/s41586-020-2649-2>

He, S., Wang, Z., Wang, Z., Gu, X., & Yan, Z. (2016). Fault detection and diagnosis of chiller using Bayesian network classifier with probabilistic boundary. *Applied Thermal Engineering*, 107, 37–47.

<https://doi.org/10.1016/j.applthermaleng.2016.06.153>

- He, Y., Zhou, C., & Hu, Y. (2023). Application of LSTM Method Combined with Feature Optimization in Chiller Failure Detection. *Journal of Physics: Conference Series*, 2442(1), 012026. <https://doi.org/10.1088/1742-6596/2442/1/012026>
- Hermes, C. J. L., & Melo, C. (2008). A first-principles simulation model for the start-up and cycling transients of household refrigerators. *International Journal of Refrigeration*, 31(8), 1341–1357. <https://doi.org/10.1016/j.ijrefrig.2008.04.003>
- Hinton, G. E., & Salakhutdinov, R. R. (2006). Reducing the Dimensionality of Data with Neural Networks. *Science*, 313(5786), 504–507. <https://doi.org/10.1126/science.1127647>
- Hu, R. L., Granderson, J., & Agogino, A. (2016, January 19). *Detection of Chiller Energy Efficiency Faults Using Expectation Maximization*. ASME 2015 International Design Engineering Technical Conferences and Computers and Information in Engineering Conference. <https://doi.org/10.1115/DETC2015-47000>
- Hua Han, Bin-Bin Gu, Tiangying Wang. (2011). Important sensors for chiller fault detection and diagnosis (FDD) from the perspective of feature selection and machine learning. *International Journal of Refrigeration-Revue Internationale Du Froid*, 34(2), 586–599. <https://doi.org/10.1016/J.IJREFRIG.2010.08.011>
- Hüsken, M., & Stagge, P. (2003). Recurrent neural networks for time series classification. *Neurocomputing*, 50, 223–235. [https://doi.org/10.1016/S0925-2312\(01\)00706-8](https://doi.org/10.1016/S0925-2312(01)00706-8)
- Ireneo C. Plando, Jr. (2023). Innovations in Refrigeration Compressor Technology: A Review of Recent Developments. *International Journal of Advanced Research in*

Science, Communication and Technology, 888–893.

<https://doi.org/10.48175/IJARSCT-12389>

Jin, B., Li, D., Srinivasan, S., Ng, S.-K., Poolla, K., & Sangiovanni-Vincentelli, A.

(2019). Detecting and Diagnosing Incipient Building Faults Using Uncertainty Information from Deep Neural Networks. *2019 IEEE International Conference on Prognostics and Health Management (ICPHM)*.

<https://doi.org/10.1109/icphm.2019.8819438>

Jin Wen & Shun Li. (2012). *RP-1312—Tools for Evaluating Fault Detection and Diagnostic Methods for Air-Handling Units*.

https://store accuristech.com/standards/rp-1312-tools-for-evaluating-fault-detection-and-diagnostic-methods-for-air-handling-units?product_id=1833299

Jolliffe, I. T. (1986). *Principal Component Analysis*. Springer.

<https://doi.org/10.1007/978-1-4757-1904-8>

Kadam, S. T., Hassan, I., Rahman, M. A., Papadopoulos, A. I., & Seferlis, P. (2020).

Review on Modeling of Vapor Compression Chillers: District Cooling Perspective. *International Journal of Air-Conditioning and Refrigeration*, 28(02), 2030003. <https://doi.org/10.1142/S2010132520300037>

Karami, M., & Wang, L. (2018). Fault detection and diagnosis for nonlinear systems: A new adaptive Gaussian mixture modeling approach. *Energy and Buildings*, 166, 477–488. <https://doi.org/10.1016/j.enbuild.2018.02.032>

- Katipamula, S., & Brambley, M. R. (2005). Review Article: Methods for Fault Detection, Diagnostics, and Prognostics for Building Systems—A Review, Part I. *HVAC&R Research*, 11(1), 3–25. <https://doi.org/10.1080/10789669.2005.10391123>
- L. H. Chiang, E. L. R. (2001). *Fault Detection and Diagnosis in Industrial Systems*. Springer-Verlag London.
- Lee, D., Chen, M.-H., & Lai, G.-W. (2022). Achieving energy savings through artificial-intelligence-assisted fault detection and diagnosis: Case study on refrigeration systems. *Case Studies in Thermal Engineering*, 40, 102499. <https://doi.org/10.1016/j.csite.2022.102499>
- Lee, D., Lai, C.-W., Liao, K.-K., & Chang, J.-W. (2021). Artificial intelligence assisted false alarm detection and diagnosis system development for reducing maintenance cost of chillers at the data centre. *Journal of Building Engineering*, 36, 102110. <https://doi.org/10.1016/j.jobbe.2020.102110>
- Lee, K. M., Yoo, J., Kim, S.-W., Lee, J.-H., & Hong, J. (2019). Autonomic machine learning platform. *International Journal of Information Management*, 49, 491–501. <https://doi.org/10.1016/j.ijinfomgt.2019.07.003>
- Lei, Z., & Zaheeruddin, M. (2005). Dynamic simulation and analysis of a water chiller refrigeration system. *Applied Thermal Engineering*, 25(14), 2258–2271. <https://doi.org/10.1016/j.applthermaleng.2005.01.002>
- Léo Bottou (with Internet Archive). (1998). *On-line learning in neural networks*. Cambridge [England] ; New York : Cambridge University Press. <http://archive.org/details/onlinelearningin0000unse>

- Li, B., Cheng, F., Zhang, X., Cui, C., & Cai, W. (2021). A novel semi-supervised data-driven method for chiller fault diagnosis with unlabeled data. *Applied Energy*, 285, 116459. <https://doi.org/10.1016/j.apenergy.2021.116459>
- Li, G., Chen, L., Liu, J., & Fang, X. (2023). Comparative study on deep transfer learning strategies for cross-system and cross-operation-condition building energy systems fault diagnosis. *Energy*, 263, 125943. <https://doi.org/10.1016/j.energy.2022.125943>
- Li, G., Hu, Y., Chen, H., Shen, L., Li, H., Hu, M., Liu, J., & Sun, K. (2016). An improved fault detection method for incipient centrifugal chiller faults using the PCA-R-SVDD algorithm. *Energy and Buildings*, 116, 104–113. <https://doi.org/10.1016/j.enbuild.2015.12.045>
- Li, G., Wang, L., Shen, L., Chen, L., Cheng, H., Xu, C., & Li, F. (2023). Interpretation of convolutional neural network-based building HVAC fault diagnosis model using improved layer-wise relevance propagation. *Energy and Buildings*, 286, 112949. <https://doi.org/10.1016/j.enbuild.2023.112949>
- Li, G., Yao, Q., Fan, C., Zhou, C., Wu, G., Zhou, Z., & Fang, X. (2021). An explainable one-dimensional convolutional neural networks based fault diagnosis method for building heating, ventilation and air conditioning systems. *Building and Environment*, 203, 108057. <https://doi.org/10.1016/j.buildenv.2021.108057>
- Li, P., Anduv, B., Zhu, X., Jin, X., & Du, Z. (2023). Diagnosis for the refrigerant undercharge fault of chiller using deep belief network enhanced extreme learning

machine. *Sustainable Energy Technologies and Assessments*, 55, 102977.

<https://doi.org/10.1016/j.seta.2022.102977>

Li, P., Liu, Z., Anduv, B., Zhu, X., Jin, X., & Du, Z. (2022). Diagnosis for multiple faults of chiller using ELM-KNN model enhanced by multi-label learning and specific feature combinations. *Building and Environment*, 214, 108904.

<https://doi.org/10.1016/j.buildenv.2022.108904>

Liang, Q., Han, H., Cui, X., Qing, H., & Fan, Y. (2018). Comparative study of probabilistic neural network and back propagation network for fault diagnosis of refrigeration systems. *Science and Technology for the Built Environment*, 24(4), 448–457. <https://doi.org/10.1080/23744731.2017.1375012>

Liu, J., Hu, Y., Chen, H., Wang, J., Li, G., & Hu, W. (2016). A refrigerant charge fault detection method for variable refrigerant flow (VRF) air-conditioning systems. *Applied Thermal Engineering*, 107, 284–293.

<https://doi.org/10.1016/j.applthermaleng.2016.03.147>

Liu, J., Zhang, Q., Li, X., Li, G., Liu, Z., Xie, Y., Li, K., & Liu, B. (2021). Transfer learning-based strategies for fault diagnosis in building energy systems. *Energy and Buildings*, 250, 111256. <https://doi.org/10.1016/j.enbuild.2021.111256>

Liu, X., Li, Y., Liu, X., & Shen, J. (2018). Fault diagnosis of chillers using very deep convolutional network. *2018 Chinese Automation Congress (CAC)*, 1274–1279. <https://doi.org/10.1109/CAC.2018.8623749>

Lu, H., Cui, X., Han, H., Fan, Y., & Zhang, Y. (2022). A feature importance ranking based fault diagnosis method for variable-speed screw chiller. *Science and Technology*

for the Built Environment, 28(2), 137–151.

<https://doi.org/10.1080/23744731.2021.1993454>

Maaten, L. van der, & Hinton, G. (2008). Visualizing Data using t-SNE. *Journal of Machine Learning Research*, 9(86), 2579–2605.

MacArthur, J. W., & Grald, E. W. (1989). Unsteady compressible two-phase flow model for predicting cyclic heat pump performance and a comparison with experimental data. *International Journal of Refrigeration*, 12(1), 29–41.

[https://doi.org/10.1016/0140-7007\(89\)90009-1](https://doi.org/10.1016/0140-7007(89)90009-1)

Mahbub, M., Hossain, M. M., & Gazi, Md. S. A. (2020). IoT-Cognizant cloud-assisted energy efficient embedded system for indoor intelligent lighting, air quality monitoring, and ventilation. *Internet of Things*, 11, 100266.

<https://doi.org/10.1016/j.iot.2020.100266>

Mathew C. Comstock, J. E. B. (1999). *Experimental Data from Fault Detection and Diagnosis Studies on a Centrifugal Chiller* (4036–1; ASHRAE Research Project 1043-RP).

McInnes, L., Healy, J., & Melville, J. (2018, February 9). *UMAP: Uniform Manifold Approximation and Projection for Dimension Reduction*. arXiv.Org.

<https://arxiv.org/abs/1802.03426v3>

Miyata, S., Akashi, Y., Lim, J., Kuwahara, Y., & Tanaka, K. (2020). *Model-based Fault Detection and Diagnosis for HVAC Systems Using Convolutional Neural Network*. 16, 853–860. <https://doi.org/10.26868/25222708.2019.210311>

- Mochammad, S., Kang, Y.-J., Noh, Y., Park, S., & Ahn, B. (2021). Stable Hybrid Feature Selection Method for Compressor Fault Diagnosis. *IEEE Access*, 9, 97415–97429. IEEE Access. <https://doi.org/10.1109/ACCESS.2021.3092884>
- Modelica*. (n.d.). Retrieved June 3, 2024, from <https://modelica.org/>
- N. Tudoroiu, M. Zaheeruddin, E. Tudoroiu, & V. Jeflea. (2008). *Fault Detection and Diagnosis (FDD) in Heating Ventilation Air Conditioning Systems (HVAC) Using an Interactive Multiple Model Augmented Unscented Kalman Filter (IMMAUKF)*. 334–339. <https://doi.org/10.1109/HSI.2008.4581459>
- Navarro-Esbrí, J., Torrella, E., & Cabello, R. (2006). A vapour compression chiller fault detection technique based on adaptative algorithms. Application to on-line refrigerant leakage detection. *International Journal of Refrigeration*, 29(5), 716–723. <https://doi.org/10.1016/j.ijrefrig.2005.12.008>
- Nie, L., Wu, R., Ren, Y., & Tan, M. (2023). Research on Fault Diagnosis of HVAC Systems Based on the ReliefF-RFECV-SVM Combined Model. *Actuators*, 12(6), Article 6. <https://doi.org/10.3390/act12060242>
- Reddy, T. A. (2007). Development and evaluation of a simple model-based automated fault detection and diagnosis (FDD) method suitable for process faults of large chillers. *ASHRAE Transactions*, 113(2), 27–40.
- Ren, Z., Han, H., Cui, X., Qing, H., & Ye, H. (2021). Application of PSO-LSSVM and hybrid programming to fault diagnosis of refrigeration systems. *Science and Technology for the Built Environment*, 27(5), 592–607. <https://doi.org/10.1080/23744731.2020.1859933>

S. Bendapudi, E. B. (2002). *A Dynamic Model Of A Vapor Compression Liquid Chiller*.

International Refrigeration and Air Conditioning Conference.

Santosh, T. V., Vinod, G., Saraf, R. K., Ghosh, A. K., & Kushwaha, H. S. (2007).

Application of artificial neural networks to nuclear power plant transient diagnosis. *Reliability Engineering & System Safety*, 92(10), 1468–1472.

<https://doi.org/10.1016/j.ress.2006.10.009>

Satyam Bendapudi, J. E. B. (2002). *Development and Validation of a Mechanistic,*

Dynamic Model for a Vapour Compression Centrifugal Liquid Chiller (Report #4036-4). ASHRAE.

Shohet, R., Kandil, M. S., Wang, Y., & McArthur, J. J. (2020). Fault detection for non-condensing boilers using simulated building automation system sensor data.

Advanced Engineering Informatics, 46, 101176.

<https://doi.org/10.1016/j.aei.2020.101176>

Simmini, F., Rampazzo, M., Beghi, A., & Peterle, F. (2018). Local Principal Component

Analysis for Fault Detection in Air-Condensed Water Chillers. *2018 IEEE 23rd International Conference on Emerging Technologies and Factory Automation*

(ETFA), 1, 1322–1327. <https://doi.org/10.1109/ETFA.2018.8502632>

Simmini, F., Rampazzo, M., Peterle, F., Susto, G. A., & Beghi, A. (2022). A Self-Tuning

KPCA-Based Approach to Fault Detection in Chiller Systems. *IEEE Transactions on Control Systems Technology*, 30(4), 1359–1374. *IEEE Transactions on Control*

Systems Technology. <https://doi.org/10.1109/TCST.2021.3107200>

- Singh, V., Mathur, J., & Bhatia, A. (2022). A comprehensive review: Fault detection, diagnostics, prognostics, and fault modeling in HVAC systems. *International Journal of Refrigeration*, 144, 283–295.
<https://doi.org/10.1016/j.ijrefrig.2022.08.017>
- Soltani, Z., Sørensen, K. K., Leth, J., & Bendtsen, J. D. (2022). Fault detection and diagnosis in refrigeration systems using machine learning algorithms. *International Journal of Refrigeration*, 144, 34–45.
<https://doi.org/10.1016/j.ijrefrig.2022.08.008>
- Song, Y., Ma, Q., Zhang, T., Li, F., & Yu, Y. (2023). Research on Fault Diagnosis Strategy of Air-Conditioning Systems Based on DPCA and Machine Learning. *Processes*, 11(4), Article 4. <https://doi.org/10.3390/pr11041192>
- Souza, A. L., Chato, J. C., Jabardo, J. M. S., Wattelet, J. P., Panek, J. S., Christoffersen, B. R., & Rhines, N. (1992). *Pressure drop during two-phase flow of refrigerants in horizontal smooth tubes*. Air Conditioning and Refrigeration Center. College of Engineering
- Stoupe, D. E. and Y. S. L. (1989). Air Conditioning and Refrigeration Equipment Failures. *National Engineer*, 93(9), 14–17.
- Sun, B., Luh, P. B., & O'Neill, Z. (2011). SPC and Kalman filter-based fault detection and diagnosis for an air-cooled chiller. *Frontiers of Electrical and Electronic Engineering in China*, 6(3), 412–423. <https://doi.org/10.1007/s11460-011-0164-9>
- Sun, K., Li, G., Chen, H., Liu, J., Li, J., & Hu, W. (2016). A novel efficient SVM-based fault diagnosis method for multi-split air conditioning system's refrigerant charge

fault amount. *Applied Thermal Engineering*, 108, 989–998.

<https://doi.org/10.1016/j.applthermaleng.2016.07.109>

Sun, X., Yan, K., & Zhou, X. (2020). Fault Detection and Diagnosis of Chillers with S&D Convolutional Neural Network. *2020 International Conferences on Internet of Things (iThings) and IEEE Green Computing and Communications (GreenCom) and IEEE Cyber, Physical and Social Computing (CPSCoM) and IEEE Smart Data (SmartData) and IEEE Congress on Cybermatics (Cybermatics)*, 829–836. <https://doi.org/10.1109/iThings-GreenCom-CPSCoM-SmartData-Cybermatics50389.2020.00141>

Szteklér, K., Kalawa, W., Stefański, S., Krzywański, J., Grabowska, K., Sosnowski, M., Nowak, W., & Makowski, M. (2019). Using adsorption chillers for utilising waste heat from power plants. *Thermal Science*, 23(Suppl. 4). <https://doi.org/10.2298/tsci19s4143s>

Tian, C., Wang, Y., Ma, X., Chen, Z., & Xue, H. (2021). Chiller Fault Diagnosis Based on Automatic Machine Learning. *Frontiers in Energy Research*, 9. <https://doi.org/10.3389/fenrg.2021.753732>

Tian, X., Becerra, V., Bausch, N., Santhosh, T. V., & Vinod, G. (2018). A study on the robustness of neural network models for predicting the break size in LOCA. *Progress in Nuclear Energy*, 109, 12–28. <https://doi.org/10.1016/j.pnucene.2018.07.004>

- Tien, C.-J., Yang, C.-Y., Tsai, M.-T., & Gow, H.-J. (2022). Development of Fault Diagnosing System for Ice-Storage Air-Conditioning Systems. *Energies*, 15(11), Article 11. <https://doi.org/10.3390/en15113981>
- Todd M. Rossi & James E. Braun. (1997). A Statistical, Rule-Based Fault Detection and Diagnostic Method for Vapor Compression Air Conditioners. *HVAC&R Research*, 3(1), 19–37. <https://doi.org/10.1080/10789669.1997.10391359>
- Tra, V., Amayri, M., & Bouguila, N. (2022a). Outlier detection via multiclass deep autoencoding Gaussian mixture model for building chiller diagnosis. *Energy and Buildings*, 259, 111893. <https://doi.org/10.1016/j.enbuild.2022.111893>
- Tra, V., Amayri, M., & Bouguila, N. (2022b). Unsupervised outlier detection using neural network-based mixtures of probabilistic principal component analyzers for building chiller fault diagnosis. *Building and Environment*, 225, 109620. <https://doi.org/10.1016/j.buildenv.2022.109620>
- TRNSYS. (n.d.). Retrieved June 3, 2024, from <https://sel.me.wisc.edu/trnsys/>
- van de Sand, R., Corasaniti, S., & Reiff-Stephan, J. (2021). Data-driven fault diagnosis for heterogeneous chillers using domain adaptation techniques. *Control Engineering Practice*, 112, 104815. <https://doi.org/10.1016/j.conengprac.2021.104815>
- Visual Environment Software for Embedded Systems* | Altair Embed. (n.d.). Default. Retrieved May 27, 2024, from <https://altair.com/embed>

- Wagner, J., & Shoureshi, R. (1992). Failure Detection Diagnostics for Thermofluid Systems. *Journal of Dynamic Systems, Measurement, and Control*, 114(4), 699–706. <https://doi.org/10.1115/1.2897743>
- Wang, L., Braun, J., & Dahal, S. (2023). An evolving learning-based fault detection and diagnosis method: Case study for a passive chilled beam system. *Energy*, 265, 126337. <https://doi.org/10.1016/j.energy.2022.126337>
- Wang, P., Xin, J., Gao, X., & Zhang, Y. (2015). Chiller gradual fault detection based on Independent Component Analysis. *The 27th Chinese Control and Decision Conference (2015 CCDC)*, 2422–2426. <https://doi.org/10.1109/CCDC.2015.7162327>
- Wang, X., & Dong, B. (2023). Physics-informed hierarchical data-driven predictive control for building HVAC systems to achieve energy and health nexus. *Energy and Buildings*, 291, 113088. <https://doi.org/10.1016/j.enbuild.2023.113088>
- Wang, Y., Yang, C., & Shen, W. (2019). A Deep Learning Approach for Heating and Cooling Equipment Monitoring. *2019 IEEE 15th International Conference on Automation Science and Engineering (CASE)*, 228–234. <https://doi.org/10.1109/COASE.2019.8843058>
- Wang, Z., Dong, Y., Liu, W., & Ma, Z. (2020). A Novel Fault Diagnosis Approach for Chillers Based on 1-D Convolutional Neural Network and Gated Recurrent Unit. *Sensors (Basel, Switzerland)*, 20(9), 2458. <https://doi.org/10.3390/s20092458>
- Wang, Z., & Oates, T. (2014). Encoding Time Series as Images for Visual Inspection and Classification Using Tiled Convolutional Neural Networks. *Undefined*.

<https://www.semanticscholar.org/paper/Encoding-Time-Series-as-Images-for-Visual-and-Using-Wang-Oates/e90666552aaaa056bc6465019632bf06917c842c>

Wang, Z., Wang, Z., Gu, X., He, S., & Yan, Z. (2018). Feature selection based on Bayesian network for chiller fault diagnosis from the perspective of field applications. *Applied Thermal Engineering*, 129, 674–683.

<https://doi.org/10.1016/j.applthermaleng.2017.10.079>

Wang, Z., Wang, Z., He, S., Gu, X., & Yan, Z. F. (2017). Fault detection and diagnosis of chillers using Bayesian network merged distance rejection and multi-source non-sensor information. *Applied Energy*, 188, 200–214.

<https://doi.org/10.1016/j.apenergy.2016.11.130>

Xia, Y., Ding, Q., & Jiang, A. (2021). Incipient Chiller Fault Diagnosis Using an Optimized Least Squares Support Vector Machine With Gravitational Search Algorithm. *Frontiers in Energy Research*, 9.

<https://doi.org/10.3389/fenrg.2021.755649>

Xia, Y., Ding, Q., Jiang, A., Jing, N., Zhou, W., & Wang, J. (2022). Incipient fault diagnosis for centrifugal chillers using kernel entropy component analysis and voting based extreme learning machine. *Korean Journal of Chemical Engineering*, 39(3), 504–514. <https://doi.org/10.1007/s11814-021-0864-7>

Xia, Y., Ding, Q., Jing, N., Tang, Y., Jiang, A., & Jiangzhou, S. (2021). An enhanced fault detection method for centrifugal chillers using kernel density estimation based kernel entropy component analysis. *International Journal of Refrigeration*, 129, 290–300. <https://doi.org/10.1016/j.ijrefrig.2021.04.019>

- Xia, Y., Ding, Q., Li, Z., & Jiang, A. (2021). Fault detection for centrifugal chillers using a Kernel Entropy Component Analysis (KECA) method. *Building Simulation*, 14(1), 53–61. <https://doi.org/10.1007/s12273-019-0598-1>
- Xue, Y., Zhang, L., Wang, B., Zhang, Z., & Li, F. (2018). Nonlinear feature selection using Gaussian kernel SVM-RFE for fault diagnosis. *Applied Intelligence*, 48(10), 3306–3331. <https://doi.org/10.1007/s10489-018-1140-3>
- Yan, J., Yu, Z., & Zhou, X. (2014). Study on operation energy efficiency model of chiller based on SVR. *The 26th Chinese Control and Decision Conference (2014 CCDC)*, 4282–4286. <https://doi.org/10.1109/CCDC.2014.6852932>
- Yan, K. (2021). Chiller fault detection and diagnosis with anomaly detective generative adversarial network. *Building and Environment*, 201, 107982. <https://doi.org/10.1016/j.buildenv.2021.107982>
- Yan, K., Chong, A., & Mo, Y. (2020). Generative adversarial network for fault detection diagnosis of chillers. *Building and Environment*, 172, 106698. <https://doi.org/10.1016/j.buildenv.2020.106698>
- Yan, K., & Hua, J. (2019). Deep Learning Technology for Chiller Faults Diagnosis. 2019 *IEEE Intl Conf on Dependable, Autonomic and Secure Computing, Intl Conf on Pervasive Intelligence and Computing, Intl Conf on Cloud and Big Data Computing, Intl Conf on Cyber Science and Technology Congress (DASC/PiCom/CBDCCom/CyberSciTech)*, 72–79. <https://doi.org/10.1109/DASC/PiCom/CBDCCom/CyberSciTech.2019.00027>

- Yan, K., Ji, Z., & Shen, W. (2017). Online fault detection methods for chillers combining extended kalman filter and recursive one-class SVM. *Neurocomputing*, 228, 205–212. <https://doi.org/10.1016/j.neucom.2016.09.076>
- Yan, K., Ma, L., Dai, Y., Shen, W., Ji, Z., & Xie, D. (2018). Cost-sensitive and sequential feature selection for chiller fault detection and diagnosis. *International Journal of Refrigeration*, 86, 401–409. <https://doi.org/10.1016/j.ijrefrig.2017.11.003>
- Yan, K., Shen, W., Mulumba, T., & Afshari, A. (2014). ARX model based fault detection and diagnosis for chillers using support vector machines. *Energy and Buildings*, 81, 287–295. <https://doi.org/10.1016/j.enbuild.2014.05.049>
- Yan, K., Su, J., Huang, J., & Mo, Y. (2022). Chiller Fault Diagnosis Based on VAE-Enabled Generative Adversarial Networks. *IEEE Transactions on Automation Science and Engineering*, 19(1), 387–395. *IEEE Transactions on Automation Science and Engineering*. <https://doi.org/10.1109/TASE.2020.3035620>
- Yan, K., & Zhou, X. (2022). Chiller faults detection and diagnosis with sensor network and adaptive 1D CNN. *Digital Communications and Networks*, 8(4), 531–539. <https://doi.org/10.1016/j.dcan.2022.03.023>
- Yan, Y., Luh, P. B., & Pattipati, K. R. (2015). Chiller plant fault diagnosis considering fault propagation. *2015 International Conference on Complex Systems Engineering (ICCSE)*, 1–6. <https://doi.org/10.1109/ComplexSys.2015.7385977>
- Yang Zhao, Zhao, Y., Tingting Li, Li, T., Tingting Li, Tingting Li, Xuejun Zhang, Zhang, X., Zhang, X., Chaobo Zhang, & Zhang, C. (2019). Artificial intelligence-based fault detection and diagnosis methods for building energy systems: Advantages,

- challenges and the future. *Renewable & Sustainable Energy Reviews*, 109, 85–101. <https://doi.org/10.1016/j.rser.2019.04.021>
- Yao, W., Li, D., & Gao, L. (2022). Fault detection and diagnosis using tree-based ensemble learning methods and multivariate control charts for centrifugal chillers. *Journal of Building Engineering*, 51, 104243. <https://doi.org/10.1016/j.jobbe.2022.104243>
- Zhang, F., Saeed, N., & Sadeghian, P. (2023). Deep learning in fault detection and diagnosis of building HVAC systems: A systematic review with meta analysis. *Energy and AI*, 12, 100235. <https://doi.org/10.1016/j.egyai.2023.100235>
- Zhang, N., Gao, X., Li, Y., & Wang, P. (2016). Fault detection of chiller based on improved KPCA. *2016 Chinese Control and Decision Conference (CCDC)*, 2951–2955. <https://doi.org/10.1109/CCDC.2016.7531487>
- Zhang, R., & Hong, T. (2017). Modeling of HVAC operational faults in building performance simulation. *Applied Energy*, 202, 178–188. <https://doi.org/10.1016/j.apenergy.2017.05.153>
- Zhang, S., Zhu, X., Anduv, B., Jin, X., & Du, Z. (2021). Fault detection and diagnosis for the screw chillers using multi-region XGBoost model. *Science and Technology for the Built Environment*, 27(5), 608–623. <https://doi.org/10.1080/23744731.2021.1877966>
- Zhang, Y., Fan, C., & Li, G. (2022). Discussions of Cold Plate Liquid Cooling Technology and Its Applications in Data Center Thermal Management. *Frontiers in Energy Research*, 10. <https://doi.org/10.3389/fenrg.2022.954718>

Zhanhong Jiang, Michael J. Risbeck, Santle Camilas Kulandai Samy, Chenlu Zhang,

Saman Cyrus, & Young M. Lee. (2023). *A timeseries supervised learning framework for fault prediction in chiller systems*. 285, 112876–112876.

<https://doi.org/10.1016/j.enbuild.2023.112876>

Zhao, Y., Wang, S., & Xiao, F. (2013a). A statistical fault detection and diagnosis method for centrifugal chillers based on exponentially-weighted moving average control charts and support vector regression. *Applied Thermal Engineering*, 51(1), 560–572. <https://doi.org/10.1016/j.applthermaleng.2012.09.030>

Zhao, Y., Wang, S., & Xiao, F. (2013b). Pattern recognition-based chillers fault detection method using Support Vector Data Description (SVDD). *Applied Energy*, 112, 1041–1048. <https://doi.org/10.1016/j.apenergy.2012.12.043>

Zhao, Y., Xiao, F., & Wang, S. (2013). An intelligent chiller fault detection and diagnosis methodology using Bayesian belief network. *Energy and Buildings*, 57, 278–288. <https://doi.org/10.1016/j.enbuild.2012.11.007>

Zhou, Q., Wang, S., & Xiao, F. (2009). A Novel Strategy for the Fault Detection and Diagnosis of Centrifugal Chiller Systems. *HVAC&R Research*, 15(1), 57–75. <https://doi.org/10.1080/10789669.2009.10390825>

Zhu, H., Yang, W., Li, S., & Pang, A. (2022). An Effective Fault Detection Method for HVAC Systems Using the LSTM-SVDD Algorithm. *Buildings*, 12(2), Article 2. <https://doi.org/10.3390/buildings12020246>

Zhu, X., Chen, K., Anduy, B., Jin, X., & Du, Z. (2021). Transfer learning based methodology for migration and application of fault detection and diagnosis

between building chillers for improving energy efficiency. *Building and Environment*, 200, 107957. <https://doi.org/10.1016/j.buildenv.2021.107957>

Zhu, X., Zhang, S., Jin, X., & Du, Z. (2020). Deep learning based reference model for operational risk evaluation of screw chillers for energy efficiency. *Energy*, 213, 118833. <https://doi.org/10.1016/j.energy.2020.118833>